THESIS FOR THE DEGREE OF DOCTOR OF PHILOSOPHY

Operando X-ray Imaging of Battery Electrodes

ANTOINE KLEIN

Department of Physics
Chalmers University of Technology
Göteborg, Sweden 2026

Operando X-Ray imaging of Battery Electrodes
ANTOINE KLEIN
ISBN 978-91-8103-375-5

Acknowledgements, dedications, and similar personal statements in this thesis, reflect the author's own views.

Doktorsavhandlingar vid Chalmers tekniska högskola
Ny serie nr 5832
ISSN 0346-718X
https://doi.org/10.63959/chalmers.dt/5832

Department of Physics
Chalmers University of Technology
SE-412 96 Göteborg
Sweden
Telephone +46 (0)31-772 1000

Cover: Orthogonal projection of metallic lithium deposition.

Printed by Chalmers Digital Printing
Göteborg, Sweden 2026

***Operando* X-ray Imaging of Battery Electrodes**

ANTOINE KLEIN
Department of Physics
Chalmers University of Technology

Abstract

Rechargeable batteries have become indispensable in modern society, enabling the widespread use of portable electronics and supporting emerging demands in transportation and grid energy storage. Increasing requirements for capacity, fast charging, and sustainability necessitate both a deeper understanding of existing technologies and the development of novel chemistries. At the heart of battery operation, complex electrochemical and structural transformations occur at the electrodes across multiple length and time scales, posing significant challenges for mechanistic insight and performance optimisation. This thesis addresses these challenges by employing *operando* X-ray imaging and scattering techniques to investigate key processes in lithium-ion, sodium-ion and lithium sulfur batteries (LiS). For Li-ion batteries, the focus was on lithium plating on graphite electrodes, a key degradation mechanism. Lithium plating was tracked using X-ray tomographic microscopy (XTM), and its interplay with the lithiation process of graphite was further investigated with scanning small- and wide-angle X-ray scattering (SWAXS). The results show that the use of electrolyte additives can delay the onset of lithium plating, that plating also occurs in the bulk of the electrode, and not only at the graphite/separator interface and that Li-plating is more localised with increasing current density. It was also found that lithium plating has an influence on intercalation by slowing down reaction kinetics. For Na-ion batteries, scanning S/WAXS was employed to follow the sodiation process in hard carbon electrodes. The results show that pore-filling is the dominant mechanism at low potentials (below 0.1 V), whereas intercalation between graphene layers occurs continuously during sodiation. For LiS batteries, XTM was used to track dissolution and precipitation of sulfur as a function of current rates. The results indicate that the sulfur conversion kinetics do not limit the cell's final capacity. Instead, the capacity loss can be attributed to incomplete utilisation of sulfur due to diffusion of soluble polysulfides beyond the electrode, resulting in active material loss. The presented experimental and analysis routes will hopefully encourage a more widespread use of X-ray imaging techniques in the battery community.

Keywords: lithium-ion batteries, sodium-ion batteries, lithium-sulfur batteries, X-ray imaging, XTM, SWAXS.

"It is not a real scientific experiment until you use sticky tape."

Adrian Rodriguez Palomo

List of papers

I. **Identifying the Role of Electrolyte Additives for Lithium Plating on Graphite Electrode by *Operando* X-ray Tomography**
Antoine Klein, Matthew Sadd, Nataliia Mozhzhukhina, Martina Olsson, Ludovic Broche, Shizhao Xiong, and Aleksandar Matic
Batteries & Supercaps 2024, e202400070

II. **Investigating the Interplay of Lithium Plating and Intercalation in Graphite Electrodes with *Operando* Scanning X-ray Scattering**
Antoine Klein, Aleksi Zitting, Marita Afiandika, Elin Dufvenius Esping, Martina Olsson, Vahid Haghighat, and Aleksandar Matic
Manuscript

III. **Resolving the Sodiation Process in Hard Carbon Anodes with Nanostructure Specific X-Ray Imaging**
Martina Olsson, Antoine Klein, Nataliia Mozhzhukhina, Shizhao Xiong, Christian Appel, Mads Carlsen, Leonard Nielsen, Linnea Rensmo, Marianne Liebi, and Aleksandar Matic
Advanced Science 2025, e08635

IV. **Investigation of 3D Structure Evolution in Lithium-Sulphur Batteries with Computed X-ray Tomography**
Antoine Klein, Salvatore de Angelis, Matthew Sadd, Stefano Checchia, Martina Olsson and, Aleksandar Matic
Manuscript

Contribution Report

I. MS planned and prepared the experiment. The synchrotron measurements were carried out by AK, MS, NM, MO, SX, AM and LB. All the data analysis was done by AK. The manuscript was written by AK and revised together by the coauthors.

II. The experimental design and beam time planning were done by AK, and the beam time was performed by AK, MA, EDE, MO, VH, and AM. Data analysis for WAXS was performed by AK, and for SAXS by AZ. AK and AZ wrote the manuscript and revised it together with the coauthors.

III. AK, MO, NM were jointly responsible for the design of the experiment. AK led the part on cell design, electrochemical investigations and evaluation. The data analysis was done by MO. The manuscript was drafted by MO and revised together by the coauthors.

IV. The experimental design and planning of the beam time were done by AK and MS. The synchrotron experiment was performed by MS, AK, SdA, SC, MO and AM. Data reconstruction was performed by the AK and SdA. Data analysis was done by AK, and advanced segmentation was performed by SdA. The manuscript was written by AK and was revised together with the coauthors.

Table of contents

Chapter 1

Introduction

The continuous economic growth of modern society is driving an ever-increasing demand for energy. Fossil fuels such as petrol, gas, and coal are consumed as though they were unlimited and without environmental consequences. However, the depletion of these resources, coupled with their significant contribution to environmental pollution, makes this approach unsustainable. A transition towards clean and sustainable energy conversion technologies is therefore needed. One of the main challenges in deploying non-carbon-based energy systems lies in their intermittent nature (e.g., solar and wind power), which can be mitigated by integrating efficient energy storage solutions. Lithium-ion batteries (LIBs), a well-established technology, are particularly suited for this purpose due to their high energy density [1, 2]. On a broader scale, the application of LIBs ranges from storing intermittent renewable energy to powering portable devices and enabling electric mobility. As part of efforts to reduce greenhouse gas emissions by 55 %, the European Union has adopted the plan "Fit for 55" [3] by 2030. Meeting this ambitious target will require significant advances in battery technology to develop electric vehicles, particularly in cost, energy density, lifetime, rate capability, material availability, and sustainability.

Since their first commercialisation by Sony in 1991 [4], LIBs have benefited from a tremendous effort of both material research and cell engineering. This effort has brought LIBs specific energy from 80 Wh/kg up to 300 Wh/kg (at the cell level) while the price per cell has decreased by 97 % [5]. LIBs still rely on similar active materials as when introduced to the market 30 years ago. On the anode side, graphite is the most common material thanks to its high theoretical capacity of 372 mAh/g, reversibility, low cost and abundance [6]. Even though graphite has been used for a long time, there is still room for improvement in terms of rate capability, especially fast charging, and coulombic efficiency. High current densities put graphite into a state where a degradation reaction is favourable to occur, called lithium plating, which is a major threat to the cell's safety [7, 8]. Thus, understanding lithium

plating in graphite electrodes and the conditions under which it develops is crucial to improve battery performance and safety.

With the diversification of applications for rechargeable batteries, there is also an increasing demand for improved performance and sustainability. This has spurred research on new battery chemistries, such as sodium-ion or lithium-sulfur (LiS) batteries. Replacing Li with Na as the active ion improves the sustainability, as sodium is the 4th most abundant element in Earth's crust [9]. However, in sodium-ion batteries, graphite cannot be used as an electrode since sodium has weak binding to the graphene layers [10], creating the need for new anode materials. To increase the capacity, a promising pathway is to go from insertion mechanisms in LIBs to conversion chemistries. LiS batteries are based on the conversion of elemental sulfur to Li_2S via a pathway that involves soluble polysulfides [11]. However, a poor cyclability related to active material loss holds the technology back from being competitive compared to LIBs [12].

The key to reaching high performance in batteries is to understand the physical and electrochemical processes taking place at the electrodes. These processes occur over a large spread of time and length scales, making a complete comprehension of, for instance, degradation, storage mechanisms and ion transport, challenging. In modern batteries, such as LIBs, the intercalation processes occur in the crystal structure of the materials, down at the angstrom level, but have undesirable macroscopic effects that need to be addressed. For instance, lithium plating is a common degradation mechanism where metallic Li is deposited on the graphite electrode instead of being intercalated in the graphite particles. One of the challenges in sodium-ion batteries is to understand the sodiation mechanism of hard carbons, a type of carbonaceous material with a higher degree of disorder than graphite, and link its microstructure with the energy storage reaction. Li/S batteries suffer from low coulombic efficiency because of the poor sulfur utilisation. Monitoring the dissolution and precipitation of sulfur particles is key to understand the complex conversion reaction mechanism. A powerful way to tackle these challenges is to investigate the fundamental processes directly in a working battery cell, making use of *operando* experiments. Synchrotron X-ray-based techniques are particularly suitable for *operando* battery research. The high energy and flux of photons enable fast measurements over many different length scales by the use of a combination of scattering and imaging techniques [13].

The scope of this thesis is to build an understanding of processes taking place inside a battery through *operando* characterisation with X-ray imaging. It aims to track physical processes in electrode materials to build a mechanistic understanding of the electrochemical processes. In **Paper I**, we investigated the effect of electrolyte additives on Li plating. By using a scanning X-ray beam, we were able to confirm the additional presence of lithium plating in the bulk of the electrode (**Paper II**). In **Paper III**, we tracked the sodiation of a hard carbon electrode through *operando*

small- and wide-angle X-ray scattering (SWAXS) imaging and observed micropore-filling inhomogeneities in the electrode. We found that the pore filling mechanism occurs at low potential (< 0.1 V) and the intercalation mechanism occurs throughout the discharge. Finally, in **Paper IV**, the dissolution and precipitation of elemental sulfur in LiS cell were followed by X-ray tomographic microscopy during cycling at different discharge rates.

Chapter 2

Batteries

This chapter aims to introduce the principles of batteries and a few examples of battery technologies that are studied in this thesis. The word "battery" is originally a military term, describing a group of cannons working together, and now also refers to a series of electrochemical cells connected to power an electrical device. However, in this thesis, the word battery will most often refer to a single electrochemical cell.

2.1 Basic principles of batteries

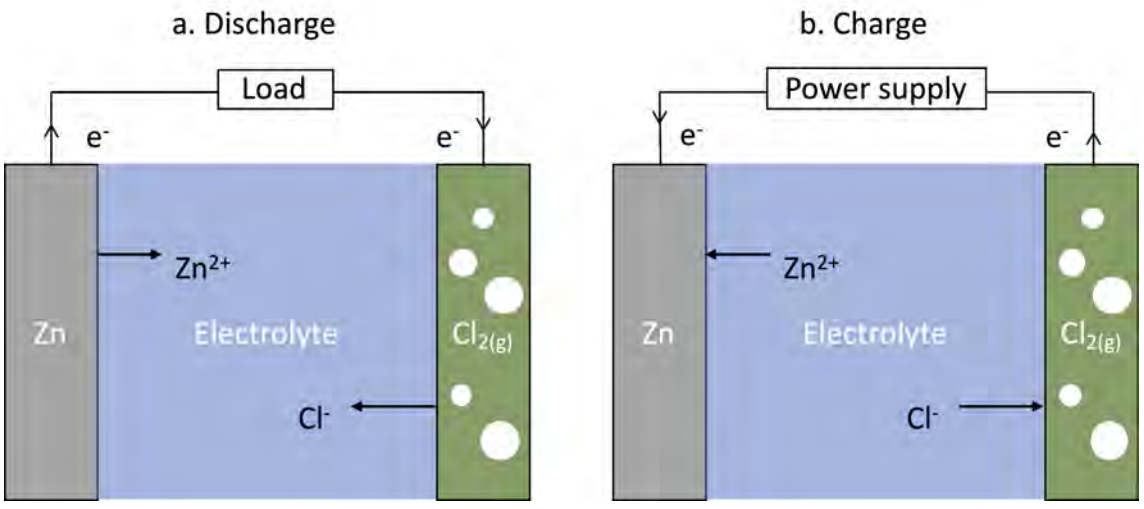

Figure 2.1: Electrochemical process of a Zn/Cl_2 cell under a. discharge and b. charge.

A battery converts chemical energy contained in active materials to electric energy by an electrochemical reaction [14]. This principle is illustrated in **Figure 2.1**, showing a battery composed of zinc (anode) and chlorine gas (cathode). At discharge, spontaneous redox reactions take place when a load is connected: the anode is oxidised, and the cathode is reduced. The flow of electrons created by the redox reactions is compensated by a flow of anions (Cl^-) and cations (Zn^{2+}) in the liquid

electrolyte. The redox half equations are the following:
Reduction (cathode):

$$Cl_{2(g)} + 2e^- \rightarrow 2Cl^- \tag{2.1}$$

Oxidation (anode):

$$Zn \rightarrow Zn^{2+} + 2e^- \tag{2.2}$$

Overall reaction (Discharge):

$$Zn + Cl_{2(g)} \rightarrow Zn^{2+} + 2Cl^- \tag{2.3}$$

If the process is reversible, the charge reaction may take place by connecting a power supply that applies a constant flow of electrons (**Figure 2.1b**). Zn^{2+} are being reduced to Zn and Cl^- oxidised back to chlorine, and equations 2.1 and 2.2 see their directions reversed. In battery research, the term "anode" often refers to the negative electrode and the term "cathode" often refers to the positive electrode, even though the use of anode/cathode depends on the state of the battery (charging or discharging); the naming convention will not be changed in this thesis.

Between the electrodes, an ion-conductive medium, an electrolyte, ensures the transport of the charged species via mass transport, such as migration or diffusion. The electrolyte is typically a liquid (e.g., water or organic solvents) with a dissolved salt to ensure ionic conductivity, and some batteries can also use a solid electrolyte [15]. The diffusion of ions in a solution follows Fick's law, which describes the movements of ions from high to low concentration according to:

$$J = -D\frac{dC}{dx} \tag{2.4}$$

where J is the flux of ions, D the diffusion coefficient, and $\frac{dC}{dx}$ is the one-dimensional concentration gradient. In addition, migration refers to the movement of ions caused by an electric field. In a battery, the electric field is produced by the difference in potential between the two electrodes:

$$\Delta E^\circ = E^\circ_+ - E^\circ_- \tag{2.5}$$

Each electrode has an intrinsic potential (also called standard potential E°) which is driving electrons to spontaneously move from the electrode with the higher redox potential (E°_+, positive electrode) to the electrode with the lower redox potential (E°_-, negative electrode). The standard potential associated with the electrochemical reaction is linked to the change in Gibbs free energy ΔG°, the number of electrons exchanged n, and Faraday's constant F [14]:

$$\Delta E^\circ = -\frac{\Delta G^\circ}{nF} \tag{2.6}$$

Another important parameter of a battery is its capacity (in Ah or coulombs), which is the number of electrons it can deliver or store. It can be measured by integrating the current with respect to time:

$$C = \int I(t)dt \tag{2.7}$$

The active materials at the battery's electrodes can thus store a certain amount of electrons, and the capacity is often scaled by the mass of the active material to obtain the specific capacity (C_s):

$$C_s = \frac{nF}{M} \tag{2.8}$$

Here, M is the molecular weight of the reactants, F is Faraday's constant, and n is the number of electrons exchanged. The specific capacity is commonly expressed in mAh/g and defines how much charge a material can store or deliver per unit of mass. The energy output is often normalised by weight as well. It is called the energy density or specific energy and is expressed in Wh/kg:

$$W = E_{cell} \cdot C_s \tag{2.9}$$

The specific energy can be determined at different levels. The active materials have a specific energy, but at the electrode level, one needs to take into account the other components, such as the additives that improve the conductivity or help keep the electrode's mechanical strength. At the cell level, one needs to consider the extra metallic foils that collect the current, the separator and the electrolyte. Finally, the battery pack weight must be considered, as well as other additional equipment, such as a cooling system or electronic circuits that regulate the battery.

2.2 Lithium-ion batteries

Lithium-ion batteries (LIBs) have become the state-of-the-art technology when it comes to secondary batteries. They cover a wide range of applications, such as phones, laptops, and electric vehicles. Even though the first LIB was commercialised in 1991 by Sony [4], their working principle has not fundamentally changed since then. In a LIB, lithium ions are transported by a liquid electrolyte and inserted into the electrodes. The positive electrode is most commonly a lithiated transition metal oxide ($LiMO_x$) or polyanionic materials such as lithium iron phosphate ($LiFePO_4$), and the negative electrode is based on graphite.

Originally, positive electrode materials were layered sulfides, e.g., TiS_2, that could intercalate lithium ions at 2.5 V, as shown by Whittingham *et.al.* in the 70s [16]. Subsequently, Goodenough *et.al.* pushed the cell voltage to 4 V by introducing

lithium cobalt oxide ($LiCo_2$, LCO) [17], while Yazami *et.al.* proved the possibility of reversibly intercalating Li^+ in graphitic materials [18]. Finally, Yoshino *et.al.* improved the electrolyte and safety [4]. In 2019, Whittingham, Goodenough and Yoshino received the Nobel Prize in chemistry "for the development of lithium-ion batteries". The first LIB introduced to the market by SONY had only an energy density of 80 Wh/kg, but this has, since then, been pushed to over 300 Wh/kg with new types of active materials, electrolytes and engineering of the cell itself [19].

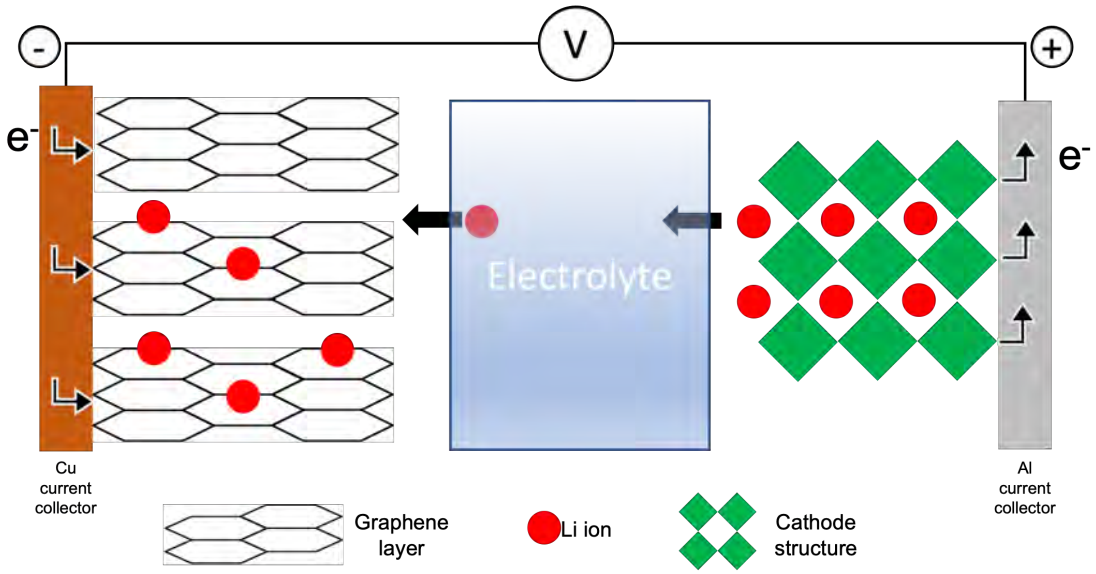

Figure 2.2: Schematic of a lithium-ion battery during charge.

Figure 2.2 shows a typical layout of a LIB. The usual negative electrode material is graphite, which is a stack of graphene layers. Lithium ions intercalate in graphite at a potential between 0.2 and 0 V vs. Li^+/Li. Graphite offers both high specific capacity (372 mAh/g), low electrode potential, and low cost (only made of carbon atoms), making it an excellent negative electrode material. Section 2.3 provides more details of lithium intercalation in graphite.

Other materials are also being investigated as alternatives to graphite for use in lithium-ion batteries. Among them, silicon is an attractive material mainly because it offers a high specific capacity of 4200 mAh/g of the Li-rich phase Li_xSi ($x = 4.4$) [20], which is more than ten times higher than that of graphite. The electrochemical reaction between lithium and silicon is an alloying reaction, which is associated with a large volume change between silicon and lithiated silicon (> 300 %) [21]. This change in volume during cycling is a major hurdle for the development of silicon-based batteries, because it induces a repeated stress in the electrode and the active material and leads to pulverisation of active material particles [22]. The mechanical degradation leads to loss in electrical contact, which inherently reduces the cyclability of lithium silicon cells. Solutions to mitigate the volume expansion due to lithiation are based on modifying the microstructure of silicon. For instance,

using porous silicon nanoparticles with a hollow core was demonstrated to cause negligible outward expansion of the particles [23]. The microporosities act as a buffer to the volume change, providing extra space for lithiated silicon to expand, while the hollow core causes inward expansion of the nanoparticle. Another example is to encapsulate silicon with a conductive material, creating a core-shell structure [24].

Another anode material considered is lithium titanate ($Li_4Ti_5O_{12}$, LTO), which undergoes negligible volume change upon lithiation [25]. Lithium intercalates in LTO at a relatively high voltage, at around 1.55 V vs. Li^+/Li, and LTO has a lower capacity (175 mAh/g) compared to other anode materials. This makes LTO inherently safer than other materials because the intercalation reaction potential is far away from the plating potential, making dendrite formation unlikely. Additionally, the high voltage plateau prevents the electrolyte from reducing at the LTO surface, which contributes to good cycle life and rate capabilities.

On the cathode side, there is a variety of active material options to choose from, depending on the desired application for the battery, e.g., if high energy or high power densities are desired. Transition metal oxides are the most common commercial cathode materials. For instance, in $LiCo_2$, lithium ions intercalate in the available octahedral sites during the discharge, whereas only half of the lithium can be removed during the charge form the structure before the release of oxygen, effectively limiting the capacity to 140 mAh/g [26]. The limited capacity, high cost and environmental hazard related to cobalt mining [27] pushed for other cathode materials that rely less on cobalt (e.g., $LiMn_2O_2$, $LiFePO_4$, or $LiNi_xMn_yCo_zO_2$, $x+y+z=1$). For instance, $LiFePO_4$ is now widely used in car batteries because of its high cycle life, low cost and sustainability [28].

The electrolyte typically consists of the lithium salt $LiPF_6$ dissolved in a mixture of organic solvents [29] (e.g., ethylene carbonate (EC), propylene carbonate (PC) or ethyl methyl carbonate (EMC)) in different ratios to improve the electrochemical and thermal stability window. The voltage window at which LIBs are operating is essential to achieve a high energy density, but at the same time, the electrolyte is not stable in this window. In the voltage range at which LIBs are working (typically, from 2.5 up to 4.5 V vs. Li^+/Li [30]), the electrolyte will decompose at the electrode surface, which is actually a vital process for stable cycling. The concept of a thin layer of decomposition products formed at the electrode/electrolyte interface was introduced by Peled in 1979 [31] and is called the solid electrolyte interphase (SEI). It will prevent further electrolyte decomposition if the following conditions are met [32]: (i.) a good mechanical stability and adhesion to the electrode for it to not detach in case of swelling or cracking during cycling, (ii.) it should be electronically insulating to prevent further decomposition and continuous consumption of the electrolyte, (iii.) it should be an ionic conductor to allow Li^+ diffusion to the electrode and

(vi.) have a homogenous composition and distribution over the electrode to avoid preferred reaction sites.

The SEI is composed of various organic and inorganic compounds, and its nature depends on the electrolyte. Typical SEI products are LiF, Li_2O, Li_2CO_3, and polyolefins [33]. The SEI is formed during the initial cycles as the potential of the electrode decreases. Depending on the type of graphite, the current densities applied and the solvents and salt used, the SEI will be formed at different potential [33] and can be controlled by careful initial cycling at low current densities. This process is called the formation cycles and is essential for long-term cycling [34].

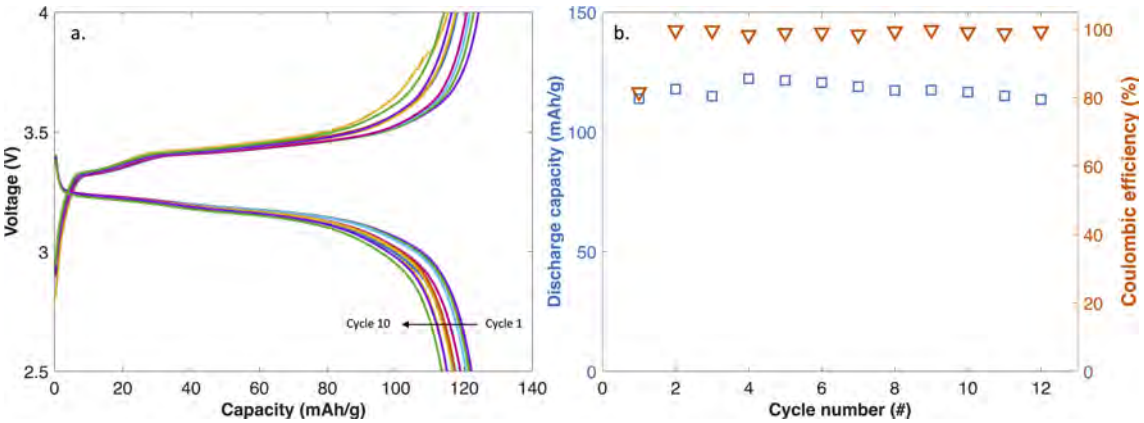

Figure 2.3: a. Voltage profile of $LiFePO_4$–Graphite full-cell over 10 cycles at a current of 1C corresponding to 2.0 mAh/cm^2. b. Corresponding discharge capacity and coulombic efficiency.

In this thesis, galvanostatic cycling was used to cycle batteries. It works by applying a constant current, and the potential response between the two electrodes is measured. Measuring the charge released by the cell makes it possible to extract useful cell parameters such as its capacity, coulombic efficiency (capacity$_{charge}$ / capacity$_{discharge}$) or rate capability. The current is usually expressed with respect to the capacity of the electrode and is called the C-rate. For example, a C-rate of C/n requires a current that corresponds to a full charge (or discharge) in n hours.

Figure 2.3a shows the voltage profile of the charge and discharge of a LFP-graphite cell. The x-axis is given as the specific capacity (mAh/g) to be able to compare different active materials or charge/discharge rates. The discharge capacity over multiple cycles can be observed in **Figure 2.3b** as well as the coulombic efficiency. The coulombic efficiency is an important parameter in batteries because it determines the cycle life. For example, a coulombic efficiency of 99 % means that the battery retains 99 % of its capacity at each cycle and the capacity retention follows a geometric decay. A battery in an electric vehicle is considered to have reached its end of life when it can only deliver 70 to 80 % of its original capacity [35]. If we

consider that the battery has reached 80 % of capacity retention in 1000 cycles, the coulombic efficiency should be $0.8^{(\frac{1}{1000})} * 100 = 99.98\%$.

When testing a battery, different configurations can be made to investigate the cell's performance. In a "half-cell" configuration, the negative electrode is a metallic Li foil and has the function of being a large reservoir of lithium. The main advantage of a half-cell configuration is that, despite having a two-electrode setup, it is assumed that the potential of the metallic counter electrode is close to 0 V vs. M^+/M (M=Li, Na, K, Mg, or Zn) since the reaction taking place is the plating or stripping of the metal. Therefore, the overall potential of the cell can be assumed to be that of the working electrode. A "full-cell" uses an actual active material at both positive and negative electrodes. The battery is being tested in conditions closer to a commercial cell to evaluate its performance.

2.3 Lithium intercalation in graphite

Graphite is a material made of carbon atoms, arranged in hexagonal layers called graphene. The layers are stacked in an ABAB sequence, meaning that carbon atoms do not have another atom directly above them and the layers are offset by half the crystallographic *c*-axis spacing [36] (**Figure 2.4**). The layers are weakly linked by van der Waals forces, making it possible to intercalate lithium ions by expanding the interlayer gap [37]. The high reversibility of lithium intercalation was part of the success of modern lithium-ion batteries [18].

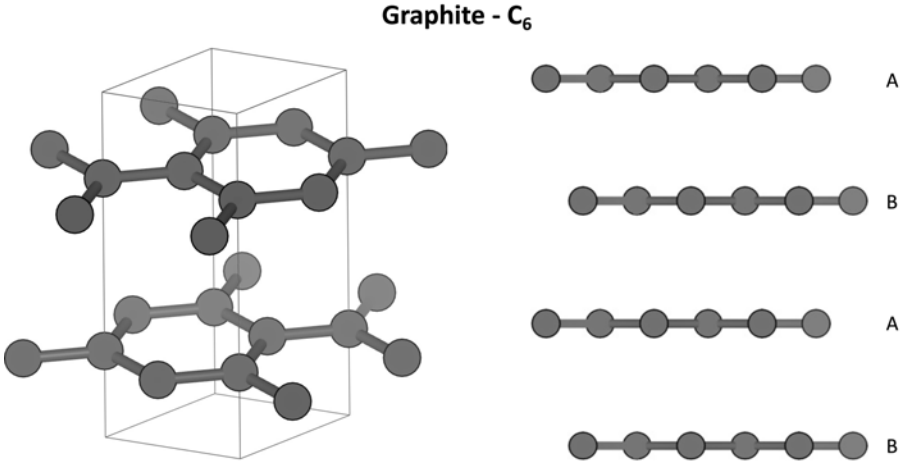

Figure 2.4: Schematic of the graphite crystal structure. This representation has been made with the VESTA software [38].

Lithium intercalation in graphite takes place at low potential, below 0.2 V vs. Li^+/Li. **Figure 2.5** shows the voltage profile of a graphite/lithium half cell during intercalation. The overall intercalation reaction of Li in graphite can be summarised

as:

$$xLi^+ + xe^- + C_6 \rightarrow Li_xC_6(0 < x < 1) \tag{2.10}$$

The different plateaus observed in the voltage profile correspond to the increased concentration of Li in Li_xC_6 $(0 < x < 1)$ or LiC_k $k = 6x$ [39, 40]. As lithium intercalates, the interlayer distance between graphene planes increases, resulting in an overall volume change of the bulk material and shift of the graphene layers, leading to a AAA stacking [37]. Different studies show that upon lithiation, graphite swells about 10-13 % in volume compared to its pristine state [37, 40–42].

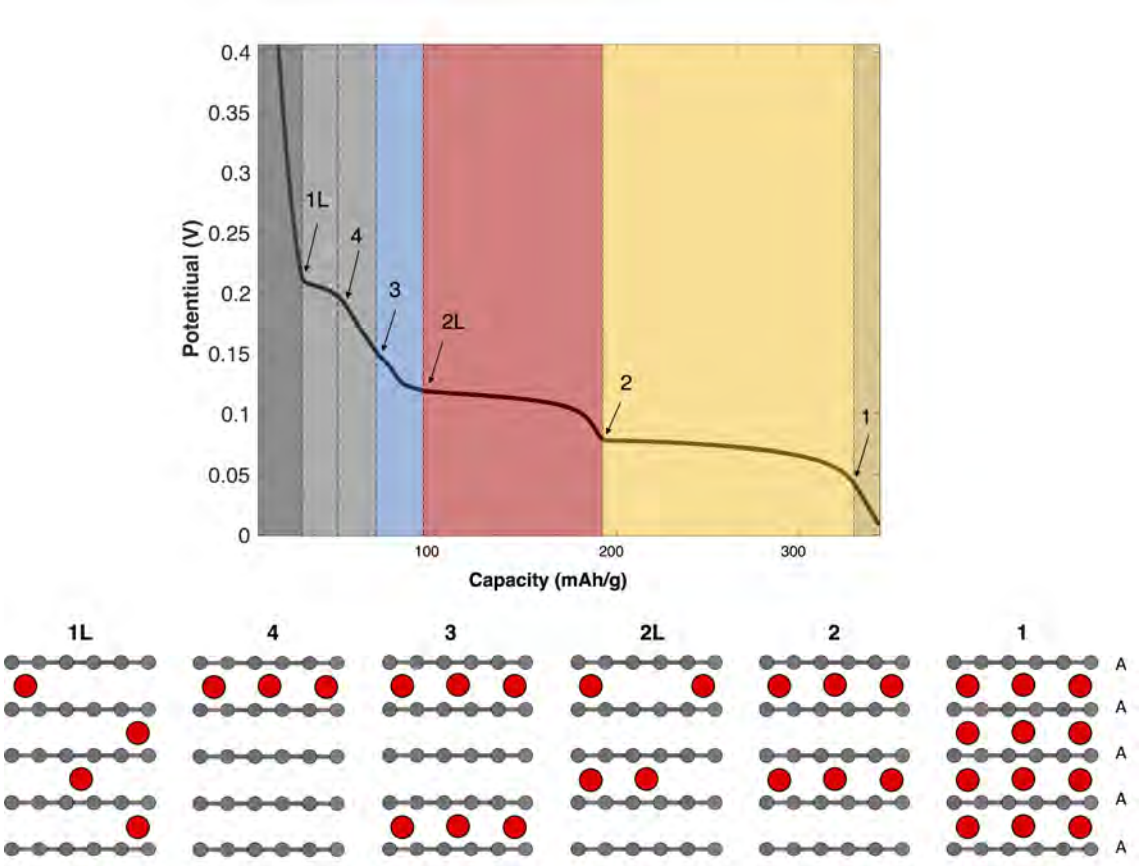

Figure 2.5: Voltage profile of lithium intercalation in graphite with illustrations of lithium intercalation stages. Lithium ions and carbon atoms are represented by red and grey spheres, respectively.

The intercalation process takes place in different stages commonly denoted in literature as: 1L, 4(LiC_{30+}), 3 (LiC_{30}), 2L (LiC_{18}), 2 (LiC_{12}) and finally stage 1 which corresponds to the final product LiC_6 [43]. **Figure 2.5** shows the stages in the voltage profile and their representative crystal structure. The plateaus mark the existence of two-phase regions, one transitioning to the next, and slopes between the plateaus indicate the end of a transition (i.e., one phase in present, see arrows in **Figure 2.5**). The number (1,2,3 or 4) in the name of the different stages reflects the number of graphene layers between layers occupied by lithium. The addition of "L"

stands for "liquid" and expresses the fact that lithium does not have a specific ordering, and is therefore organised in a liquid-like phase. As the intercalation process starts, the first stage 1L represents a dilute solid solution where traces of lithium can be found in every inter-layer [44]. The system transitions early on to stage 4, at a voltage below 0.2 V vs. Li^+/Li. The next transitions, 4 and 3, are still up for debate [45] on the exact crystal structure and ordering of the graphite layers. More defined plateaus can be observed for the transition between stages 2 and 2L with a progressive ordering of lithium between graphene layers. The final transition to stage 1 shows up as a sharp drop of potential to 0 V vs. Li^+/Li, indicating that the intercalation process is finished. The intercalation of ions into the crystal structure is associated with a change in the visible absorption of the lithiated graphite compounds [46, 47]. The black/grey looking graphite is turning dark blue at stage 3, then red in stage 2/2L to finally become gold at stage 1. At the electrode scale, the intercalation process is generally not homogeneous, depending on the cell pressure and temperature distribution and internal local resistances, which lead to different lithiation states [7, 48, 49].

2.4 Lithium plating on graphite

Lithium plating is a common degradation mechanism during the lithiation of graphite [50]. As lithium ions are intercalated in graphite, the potential of the electrode drops close to 0 V vs. Li^+/Li (**Figure 2.5**). Theoretically, the intercalation reaction should stop at this limit, but under high current densities, high state of charge (SOC) or low-temperature conditions [50], the potential can drop below 0 V and trigger lithium plating instead of insertion. In addition, if graphite is already fully lithiated (i.e., in case of a high state of charge or overcharging), there is no more space in the electrode to accommodate Li^+, which will result in an accumulation of ions at the graphite-electrolyte interface, and lithium can plate and form a metallic film at the surface of graphite. The SOC dependence of plating was studied by Petzl *et.al.* who proposed a linear relationship between the mass of plated lithium and SOC [51].

Charging at low temperatures increases the risk of lithium plating, typically, in the temperature range of -20 °C to + 60 °C [52]. It is considered that below -20°C, transport properties, like diffusion of lithium in graphite, ionic conductivity (in the electrolyte and SEI), and charge transfer rate are significantly decreased [53]. At low temperatures, lithium ions adsorb at the graphite interface faster than they can diffuse into the electrode, resulting in an accumulation of charges and thus a rise in the onset of lithium plating [54]. Additionally, low temperatures is leading to ion depletion at the graphite/electrolyte interface [55], which increases the competition between intercalation and plating. Once lithium plating is triggered, the reaction will continue.

There are two main effects on the battery when lithium plating occurs: a safety issue and a capacity fade. Plated lithium typically grows in a dendritic fashion [56], i.e., fractal, spiky structures that can lead to short circuits of the cell if they reach the positive electrode. The short circuit can cause a rapid and uncontrolled increase in temperature (also called thermal runaway) to the point where the battery fails catastrophically and releases all its energy in the form of heat [57]. The capacity fade over multiple cycles due to Li-plating is caused by different phenomena [53]. The first one is the loss of active material with the creation of dead Li. After lithium has been plated, a fraction of it will be stripped back during the discharge; it is thus called reversible lithium plating and does not lead to capacity fade. It is also possible for plated lithium to re-intercalate back into the graphite if the cell is left at the open circuit or while stripping lithium [47, 58, 59]. The proportion of plated lithium that is not stripped back is simply not available anymore, which causes a loss of lithium inventory and thus available capacity [60]. The plating and growth of lithium also lead to new surfaces available for the formation of fresh SEI [61], and the electronically insulating nature of SEI can lead to the disconnection of dendrites from the electrode, creating dead Li. As seen in section 2.2, SEI is made of various components from the electrolyte. This newly formed SEI on lithium causes a continuous consumption of electrolyte, leading to further capacity fade [53].

2.4.1 Mitigation strategies

This section aims to introduce some strategies that help reduce or suppress lithium plating on graphite during charging of a Li-ion battery. Here, three approaches are considered: through the design of the cell, the modification of the electrode and the use of electrolyte additives.

In commercial lithium-ion batteries, the cell is designed to have an excess capacity on the anode (negative) side compared to the cathode (positive), also known as the negative-to-positive ratio (N/P), which is then greater than one. The extra capacity at the negative side acts as a buffer in case the battery is overcharged, preventing lithium plating if the charge limit is exceeded. Typically, a N/P ratio of 1.2 was found effective at reducing lithium plating [62]. The ideal ratio, however, depends on the detailed design of the cell, as it can affect the distribution of current and temperature, two parameters that are also important to prevent plating. The N/P ratio can be seen as a security in the cell design, but cannot by itself prevent plating, which can occur anyway if the conditions listed in section 2.4 are fulfilled.

Another strategy relies on the design of the electrode, for instance, by modifying the electrode morphology. The tortuosity of the electrode is defined as the ratio between the actual path of the ions in a porous electrode and the direct straight line path between the top and bottom of the electrode [63]. The tortuosity has an influence on ion transport in the electrode, which determines the local ion concentration.

Ensuring that every active material particle is accessible to lithium ions is crucial to prevent lithium plating. Habedank *et al.* used a pulsed laser to create holes in the electrode to change the tortuosity [64]. The artificially created channels in the graphite electrode improved the capacity retention of the cell by reducing the formation of plated lithium, even at -15 °C.

The electrolyte plays a major role in preventing Li plating, and choosing the right combination of salt, solvent and additives is crucial. For instance, the introduction of low concentrations of additional species in the electrolyte is a strategy to mitigate Li plating by changing the nature of the SEI. For instance, Jones *et.al.* showed the beneficial effect of adding 0.1 M lithium bis(fluorosulfonyl)imide (LiFSI) to a solution of 1.0 M LiPF6 in EC, EMC, and methyl propionate (MP) in a 20:20:60 volume ratio on preventing lithium plating at low temperatures (down to -50 °C) [65]. This improvement was due to a reduced SEI resistance while also not altering kinetics at the positive electrode because LiFSI creates an SEI rich in inorganic lithium compounds, such as LiF [66, 67]. They also proposed that the addition of 2 % in concentration of vinylene carbonate (VC) increased the tendency for lithium plating at low temperatures. On the other hand, it was shown by Burns *et.al.* that VC can have a beneficial effect on plating [68] depending on its concentration. VC increases the inorganic and polymeric components of the SEI, protecting from further electrolyte decomposition [69].

2.4.2 Detection of lithium plating

The detection of lithium plating in LIBs is often considered a challenging task, especially in commercial cells. The theoretical definition of the start of Li plating is the electrode potential dropping below 0 V vs. Li^+/Li. However, this simple condition is most often hard to verify since the overall cell voltage is measured by the difference in potential between the two electrodes in the cell. Thus, knowing the actual potential of one of the electrodes is impossible in this setup. To address this issue, one can introduce a third reference electrode, enabling one to determine the potential of the individual electrodes. This simple and reliable method can detect Li plating, but its implementation in battery cells requires design modifications that can impact battery performance [70, 71].

Another method that can be implemented to detect Li plating is an analysis of differential capacity during delithiation. At delithiation, plated lithium will be stripped first, i.e., at a voltage lower than the one for the de-intercalation process, and can be observed in the voltage profile by an early plateau [72]. In differential capacity analysis, this plateau is transformed to a peak, allowing an easy identification of the lithium plating onset [65, 73]. This method can easily be applied while the battery is being cycled since it does not require additional equipment or characterisation methods.

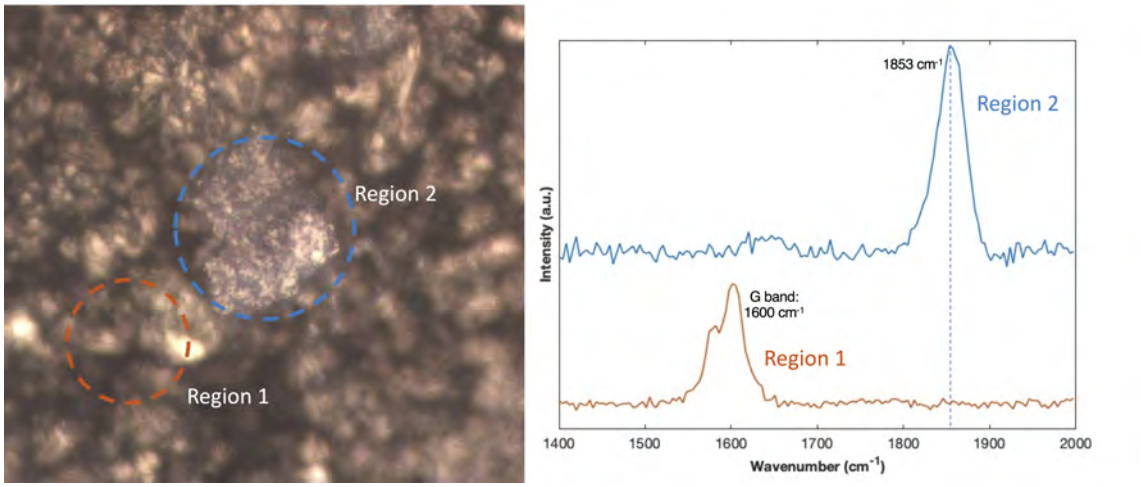

Figure 2.6: Optical microscopy image of a fully lithiated graphite electrode surface and associated Raman spectra. The electrode comes from a cycled coin cell and is put in an air-tight cell with a glass window, enabling Raman imaging of the electrode.

To identify plated Li after the battery has been cycled, it is possible to open the cell and visually inspect the electrode. This method has the advantage of being simple but is destructive, not quantitative and is limited to the plated lithium at the surface of graphite[74]. Observation of lithium deposition can also be done by various surface-sensitive techniques, e.g., atomic force microscopy (AFM) [75], transmission electron microscopy (TEM) [76] or optical microscopy [56, 77]. These methods can image the electrode and identify plated Li; however, they cannot provide a quantitative analysis of the deposition, which is crucial to be able to compare studies and carry out deeper analysis. Nuclear Magnetic Resonance (NMR) has a great sensitivity to ^{7}Li, and can quantify the mass of plated Li and also determine the type of plated morphology, whether it is mossy or dendritic, because of the different orientations of lithium deposition in the magnetic field[78, 79].

Raman spectroscopy has also been used to identify plated Li on graphite electrodes [80, 81]. Lithium plating has a signature in the Raman spectrum because a new species, lithium acetylide (Li_2C_2), forms when lithium reacts with the SEI of graphite. The triple $C \equiv C$ bond gives a Raman peak at around 1850 cm^{-1}, and can be used to locate specific spots where lithium plating occurs on the electrode with Raman imaging. In **Figure 2.6**, an optical microscopy image shows in which regions Raman spectra have been measured. The gold-looking 'Region 1' is a lithiated graphite grain and displays the typical Raman G-band at around 1600 cm^{-1} [82]. In 'Region 2', one can identify a grey-looking phase associated with lithium plating. The spectrum in this region shows a band at 1853 cm^{-1} which is not present in 'Region 1'.

X-ray imaging has been used to track lithium plating [41, 83–85]. X-ray tomographic

microscopy can provide a 3D image of lithium microstructure while the battery is being cycled. However, identifying lithium growing on a graphite surface is challenging in absorption-based tomography because of the poor contrast between graphite, electrolyte-filled pores and deposited Li [86]. Using X-ray imaging techniques to observe lithium plating will be further discussed in Chapter 3.

2.5 Sodium intercalation in hard carbons

Sodium-ion Batteries (NIBs) are an alternative to lithium-ion batteries with the promise to improve sustainability, sodium being the 4th most abundant element in Earth's crust [9]. However, unlike lithium, graphite is not suited for sodium because it cannot intercalate into graphite [87]. The inability of sodium to intercalate into graphite is primarily governed by the thermodynamics of the system and can be elucidated through density functional theory (DFT) calculations, which separate the contributions of structural deformation and binding energy in forming a hypothetical NaC_x compound [10]. The structural energy arises from the deformation of the AB-stacked graphite structure during intercalation and is higher for sodium compared to lithium. For a stable graphite intercalation compound to form, this structural energy must be compensated for by the binding energy. However, because the binding energy of Na is insufficient to overcome the deformation cost, sodium intercalation into graphite is thermodynamically unfavourable [10]. Hence, alternative anode materials are needed.

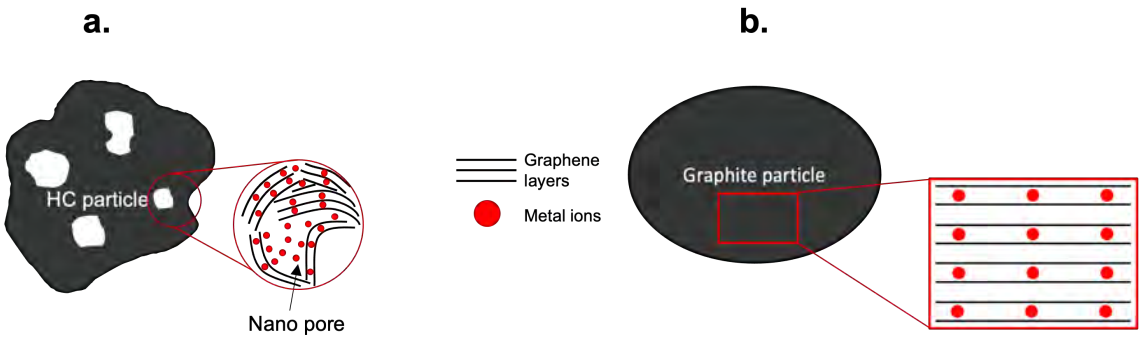

Figure 2.7: Comparison between **a.** hard carbon and **b.** graphite structures. The schematics and zoomed inset are not to scale.

Other types of carbonaceous materials have instead been investigated as anodes for sodium ion batteries [87]. Among them, hard carbons (HC) are a promising class of negative electrode materials with high specific capacity. For instance, Zhao *et.al.* combined a 400 mAh/g HC anode with a layered oxide positive electrode to make a cell with an energy density of 240 Wh/kg based on the materials used [88]. However, this performance was reported for only 50 cycles and in a coin cell setup, far from industry-standard pouch or prismatic cells. More recently, Contemporary Amperex

Technology Co., Ltd. (CATL) announced the first generation of commercial sodium-ion batteries featuring a hard carbon negative electrode and Prussian white positive electrode, reaching 175 Wh/kg at the cell level [89].

Hard carbons are disordered materials and lack the long-range order of graphite, granting them superior mechanical strength compared to graphite, hence the term hard carbon [87, 90] **Figure 2.7a.**). Hard carbons contain microporosities that are divided into two categories: the open pores are connected to the outside (in contact with the electrolyte), and the closed pores are inaccessible to the electrolyte, with a size ranging from 0.45 to 4 nm [90–92]. Moreover, the graphene layers in HC are randomly stacked and oriented compared to the regularly oriented and spaced layers in graphite (**Figure 2.7b**).

The extra space in the pores and between graphene layers enables new ways for ion insertion, leading to a more complex storage mechanism compared to graphite, with pore filling, defect adsorption, and intercalation between graphene layers, and the sodiation mechanism is still up for debate [93]. A typical voltage profile of HC sodiation is shown in **Figure 2.8**. Generally, the slope region has been attributed to intercalation between graphene layers and the plateau region to pore filling [90, 93]. However, the structure of HC can vary considerably depending on the pyrolysis temperature and precursor, which complicates the creation of a single model to fully describe the storage mechanism. HC is synthesised by pyrolysis of various organic precursors below the graphitisation temperature of 3000 °C [93], and the specific synthesis temperature will influence both the pore size distribution and graphene spacing [94]. Typical pyrolysis temperature range is between 1000 °C and 2000 °C, giving a pore size distribution of 0.51 nm to 0.92 nm in radius [90]. High pyrolysis temperature means that the structure is closer to the highly ordered long-range structure of graphite. It is expected that elevated synthesis temperature (typically at 2000 °C) reduces defect concentration and interlayer spacing, as well as increases the nanopore size distribution in the hard carbon structure [90, 94].

Studying the sodiation process is a challenging task due to the complex structure of hard carbons. However, scattering techniques are well-suited to understand how sodium is inserted into hard carbon. For instance, with Raman scattering, the effect of the pyrolysis temperature on the structure has been investigated. The HC Raman spectrum shows the characteristic D (1350 cm^{-1}) and G bands (1590 cm^{-1}), related to sp^2 carbon atoms bond stretching and breathing, respectively. The intensity ratio of these two bands can be used as an estimation of the defect concentration in HC (e.g., vacancy point defects) [90]. Small and wide-angle X-ray scattering (SWAXS) can also be used to describe the hard carbon structure. By modelling the SAXS pattern [90, 95], it is possible to extract information on particle roughness and micropore filling during the sodiation process. Raman spectroscopy and SWAXS will be discussed in this thesis in Chapter 3 and Chapter 4.

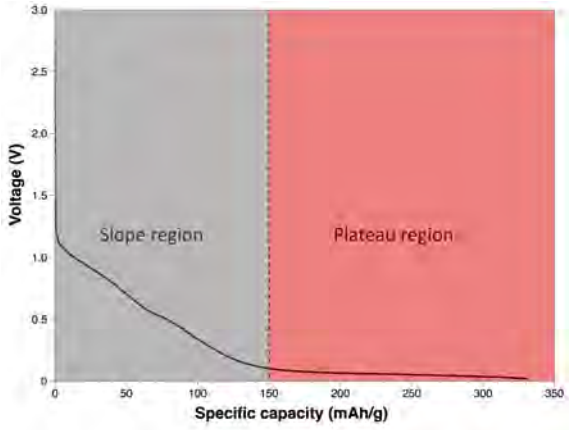

Figure 2.8: Voltage profile of the sodiation of commercial hard carbon at a constant current of an HC–Na coin cell. Current corresponds to C/10 or 20 mA/g.

2.6 Lithium-sulfur batteries

Lithium-sulfur (LiS) is a promising next-generation battery chemistry to replace the current state-of-the-art LIBs. The large specific capacity of elemental sulfur (1672 mAh/g) compared to common positive electrode materials (140 mAh/g for $LiCoO_2$), the non-toxicity, and the abundance of sulfur make it a suitable choice for sustainable, high-energy density batteries [12, 96]. A sulfur electrode is generally made up of elemental sulfur, S_8, embedded in a matrix of conductive carbon and a binder. The binder ensures that the composite electrode holds together, and the carbon additive creates an electron-conductive network to electrically connect sulfur particles as sulfur is an insulator (scheme in **Figure 2.9a**). The capacity of the cell comes from the conversion of elemental sulfur to Li_2S according to:

$$S + 2Li^+ + 2e^- \rightarrow Li_2S \tag{2.11}$$

The conversion pathway in common ether-based electrolytes (typically 1M lithium bis(trifluoromethanesulfonyl)imide (LiTFSI) salt dissolved in 1,2-dimethoxyethane (DME) and 1,3-dioxolane (DOL) in a 1:1 volume ratio) can be broken down into several intermediate steps [97, 98]:

$$S_8 + 2Li^+ + 2e^- \rightarrow Li_2S_8 \tag{2.12}$$

$$Li_2S_8 + 2Li^+ + 2e^- \rightarrow Li_2S_{8-n} + Li_2S_n \quad (n = 4 - 6) \tag{2.13}$$

$$Li_2S_{8-n} + Li_2S_n + 12Li^+ \rightarrow 8Li_2S \tag{2.14}$$

At the beginning of the discharge, solid sulfur, S_8, is converted to the polysulfide Li_2S_8 according to Equation 2.12. In common electrolytes, this polysulfide is soluble, and the initial reaction then also involves a solid-liquid transition which is

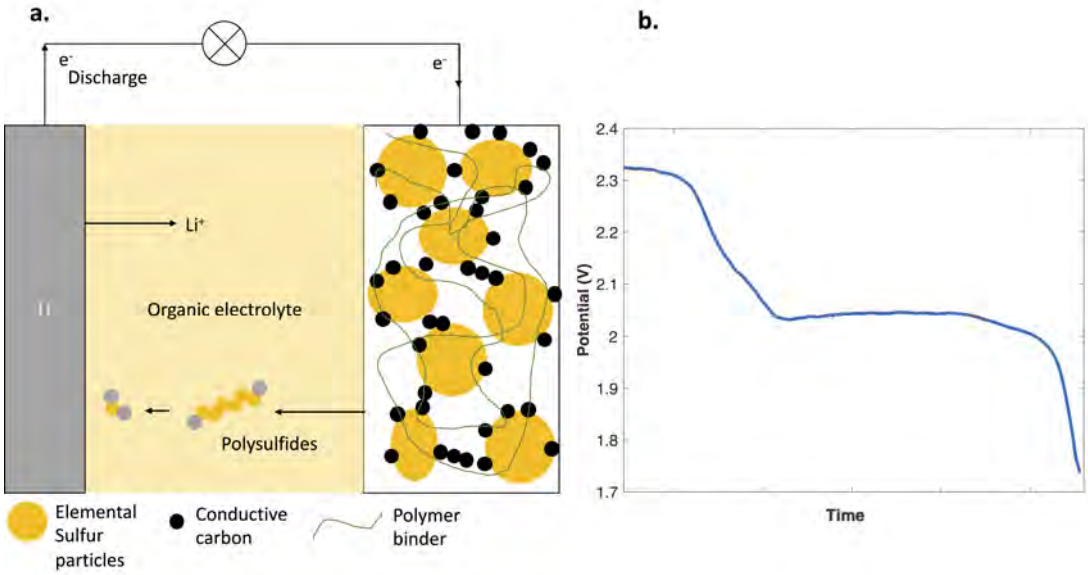

Figure 2.9: **a.** Scheme of a LiS cell with a sulfur-carbon composite electrode combined with a Li metal counter-electrode. **b.** Voltage profile of a LiS cell at discharge under a constant current of 1C corresponding to 3.4 mA/cm^2 and a mass loading of 2.0 mg/cm^2.

related to a plateau in the voltage profile (**Figure 2.9b**) between 2.3-2.4 V [98–100]. Subsequently, long-chain polysulfides are converted to shorter-chain polysulfides $Li_2S_n (n = 4 - 6)$ in a liquid-liquid reaction (Equation 2.13), since these polysulfides are all soluble in common electrolytes. This is reflected in the voltage profile by the slope between the first high-voltage plateau and a second plateau around 2.1 V. The lower plateau is a result of further conversion of Li_2S_n to the end product Li_2S [100]. The last step also involves a liquid-to-solid transition since Li_2S is insoluble in most common electrolytes. The cell polarisation at the very end of the discharge (a sharp drop of the potential) indicates that all the sulfur has been converted to Li_2S and the reaction is terminated.

Since intermediate conversion products, $Li_2S_n (n = 3 - 8)$, are soluble in the liquid electrolyte, they can diffuse out of the electrode and into the bulk electrolyte and reach the counter electrode due to concentration gradients. Once at the lithium surface, during the charge, they can gain an electron and reduce to shorter chains and then diffuse back to the working electrode, where they are oxidised once again. This reaction is known as the shuttle effect and is a parasitic reaction responsible for the poor coulombic efficiency of many LiS batteries [101–103]. Another issue connected to the solubility of polysulfides is that diffusion back to the cathode can be slow. This leads to capacity fade during cycling as a part of the active material is lost in the electrolyte [12].

Another important aspect of LiS batteries is the electrolyte/sulfur ratio (E/S), which

needs to be as low as possible (around 1 μL/mg) to reach high energy densities [104]. However, a low E/S ratio means an increase in viscosity due to a high polysulfide concentration in the electrolyte, which is causing an increase in the cell's polarisation and decreases the sulfur utilisation [105]. Furthermore, lean electrolyte conditions activate the polysulfide shuttle effect by increasing concentration gradients, corrode the lithium counter electrode and decrease the sulfur reaction kinetics [104]. At the research scale, the E/S ratio is often reported to be > 20 μL/mg [106]. This gives a false representation of cell performance since a flooded cell compensates for the above-mentioned challenges.

One way of preventing the shuttle effect is by having lithium nitrate as an additive in the electrolyte ($LiNO_3$). $LiNO_3$ is effective because its decomposition products form a protective passivation layer at the anode during the charge, and suppresses polysulfide reaction [107]. However, this passivation layer continuously breaks down and needs to be formed again over time. This leads to the consumption of lithium nitrate, which in fact is a sacrificial salt to prevent the shuttle effect [104]. The use of excess electrolyte or additives is typical in LiS batteries and can solve the shuttle effect for a while, but these strategies only delay the eventual failure of the cell. In addition, they lower the energy density, which is crucial for portable applications.

To circumvent polysulfides dissolution and loss of active material, another reaction pathway can be followed, where elemental sulfur is directly converted to short-chain polysulfides with a lower solubility compared to longer ones, called the quasi-solid reaction pathway [98]. This type of reaction is enabled using different types of electrolytes called sparingly solvating electrolytes (SSE). SSE rely on a low solubility of polysulfides, which shortens the reaction pathway from S_8 to short-chain polysulfides. The limitations of SSE are caused by the slow kinetics of Li_2S_2/Li_2S conversion, the use of salts with low ionic conductivity and high viscosity [105, 108]. One example of SEE was developed by Nazar's group, which is glyme-based [106], and another electrolyte from CIC energiGUNE is based on sulfolane and a highly fluorinated ether-based solvent [109]. In these studies, a low electrolyte to sulfur ratio was used and still resulted in high specific capacities, i.e., high active material utilisation.

An alternative strategy to liquid electrolytes for mitigating polysulfide diffusion is the implementation of a solid electrolyte. Because diffusion of polysulfides is inherently suppressed in solid phases, the shuttle effect and polysulfide dissolution can be effectively minimised, thereby reducing sulfur loss and enabling long-term cycling stability. Furthermore, solid electrolytes can inhibit lithium dendrite formation and offer enhanced safety compared to liquid electrolytes by lowering the risk of thermal runaway [110]. Despite these advantages, solid electrolytes are constrained by their relatively low ionic conductivity, which limits overall cell performance. Typically, liquid electrolytes exhibit ionic conductivities on the order of 10^{-2} S/cm [111],

whereas solid electrolytes generally range from 10^{-2} S/cm down to 10^{-6} S/cm or lower at room temperature [110]. Additionally, solid electrolytes are prone to form cracks due to their brittleness, which can increase internal resistances, build up plated lithium and lead to a short circuit of the cell [112].

A massive research effort is needed to understand the complex sulfur conversion reaction and improve LiS battery performance. Characterisation techniques such as the X-Ray Diffraction (XRD) [100] have shown that polysulfides adsorb on the fibres of the separator. Raman spectroscopy, [113], has been used to provide a better comprehension of the evolution of polysulfide species in the electrolyte with selective solubility of fluorinated ether-based electrolytes. X-ray tomographic microscopy (XTM) has been used to directly image sulfur particles and quantify their dissolution/precipitation throughout cycling [99, 114–116]. Tan *et.al.* used absorption-based computed tomography to resolve a sulfur cathode and reported that the reaction rate is diffusion-limited since the dissolution and precipitation of elemental sulfur evolves from the cathode-separator interface [115]. More recently, Sadd *et.al.* applied synchrotron-based XTM to demonstrate the complete dissolution of sulfur and observe the precipitation of end-of-discharge product Li_2S with a phase contrast reconstruction [99].

Chapter 3

Battery characterisation with *operando* X-ray techniques

The electrochemical reactions taking place in the battery's electrodes are associated with several processes that have effects over a large span of length scales, **Figure 3.1**. These processes are linked together, and processes at the atomic scale can result in changes on the particle or the electrode scale, which affects the performance of the battery overall. At the atomic scale, metal ions insert into the crystal structure and are associated with a change in oxidation state. For instance, in $LiCoO_2$, the lithium ions are intercalated in the octahedral sites of the crystal lattice and compensated by the redox couple Co^{4+}/Co^{3+}. However, during charge, it is only possible to remove half of the lithium ions from $Li_{1-x}CoO_2$ ($x < 0.5$) before the structure starts releasing its oxygen, limiting the capacity to 50 % of the theoretical one (140 mAh/g) [26]. In graphite, as discussed in section 2.3, lithium is being intercalated between the graphene layers, which are expanding with increased content of lithium and producing volume change of the entire electrode [6]. Such structural deformations experienced by the electrodes over the battery's lifetime can produce macroscopic degradation, such as cracks, particle disconnection or delamination from the current collectors, resulting in capacity loss [117]. Lithium-ion batteries rely on reversible electrochemical reactions to store and release energy, but there are several irreversible processes that can occur. The SEI formation in the early cycles is irreversible because it is consuming materials from the electrodes and electrolyte in order to create a protective layer [34]. Electrodes based on conversion reactions, such as lithium-sulfur, are also subject to irreversible reactions. For instance, the shuttle effect leads to loss of sulfur, but also soluble polysulfides can diffuse out of the electrode and cannot participate any more in the capacity-producing reaction [102].

All these processes are occurring while the battery is operating, and a powerful way to study these issues can be done by performing *operando* characterisation. There is a wide range of techniques that can be used *operando*, for instance, transmission

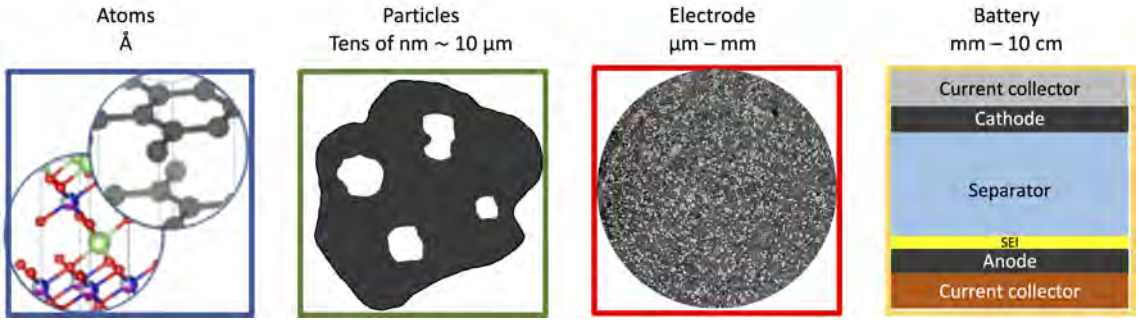

Figure 3.1: Characteristic length scales of a battery system.

electron microscopy (TEM) [118], nuclear magnetic resonance (NMR) [119], optical microscopy [77] or Raman spectroscopy [120]. *Operando* TEM offers imaging on the atomic scale of the materials, providing information on ion intercalation, structural changes and phase evolution in the electrode or SEI formation [118]. However, TEM setup requires special cells that have large overpotentials, which can make interpretation of the results challenging to link to more realistic cells. Additionally, the electron beam can damage the materials by decomposing the electrolyte, which can lead to gas formation.

NMR has been used to study lithium plating because the Li metal has a clear signal compared to lithium ions intercalated in graphite or Li in the SEI [7, 79, 121, 122]. As an example, *operando* NMR has been used to detect the formation of lithium and sodium dendrites on hard carbon electrodes [121], and the results revealed that the quasimetallic Li in the hard carbon pores acts as a buffer for further lithium deposition. NMR measurements produce a higher spectral resolution when the sample is spun, which is impracticable in *operando* NMR [119].

To characterise batteries on the μm to mm length scale, one can use optical imaging of the electrode. The strength of optical microscopy lies in its simplicity, without the need for an X-ray or neutron source, and the fact that visible light is non-destructive to the materials. Optical microscopy has been used to study the evolution of lithium dendrites [56, 77, 123] or the volume change of silicon particles during alloying with lithium [124]. Optical microscopy is particularly powerful for colourimetric measurements, for instance, with graphite particles that undergo a colour change as they are being lithiated, enabling quantification of the battery's state of charge [46]. The main drawbacks of optical microscopy are that it is limited in resolution to hundreds of nanometres due to the diffraction limit [125], and it often requires modification of the cell with a transparent window that can limit the performance. Another issue is that visible light cannot access the bulk of the materials, which inherently restrains optical microscopy to surface analysis.

3.1 X-ray based characterisation techniques

X-rays were discovered by Röntgen in 1895 when he found out that a high voltage discharge tube could cause the fluorescence of a plate covered with barium platinocyanide. He called this new unknown radiation "X-ray" [126]. X-rays are electromagnetic waves with a wavelength in the range 0.01-10 nm, which corresponds to photons with an energy of 100 eV to 100 keV [127]. X-rays interact with the electron cloud of the material, and two main interactions are possible: absorption and scattering. The absorption of an X-ray photon involves the transfer of its energy to an inner-shell electron, which can be ejected from the atom **Figure 3.2a**. This is called the photoelectric effect, and it is the principle behind X-ray photoelectron spectroscopy (XPS). Photons absorbed might promote excitation of electrons from the core to the valence band or unoccupied states, and probing a sample with changing incident photon energy is the principle behind X-ray absorption spectroscopy (XAS). The scattering effect is caused by the electromagnetic field of the incoming photon inducing an acceleration of the electron, causing it to re-radiate light at the same frequency (elastic scattering, **Figure 3.2b**).

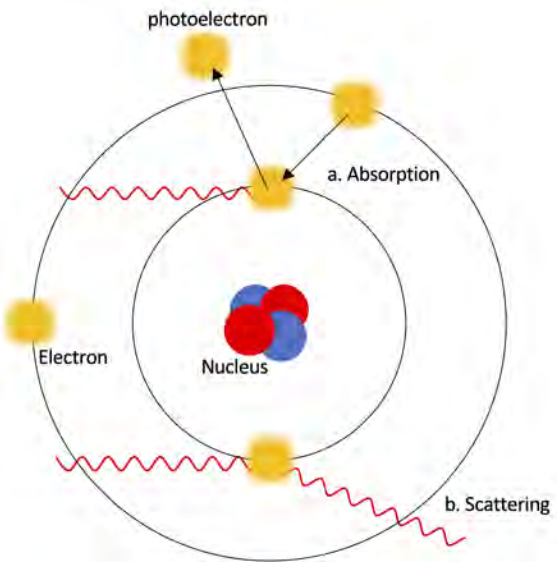

Figure 3.2: Illustration of X-ray interaction with matter. a. photoelectric effect that causes fluorescence and b. elastic scattering.

Nowadays, the best quality X-rays are produced at synchrotron sources where the beam has a high flux, tunable wavelength and high brightness. Synchrotron radiation facilities offer several advantages over conventional laboratory X-ray sources. Their brilliance, defined as the photon flux per unit source size and angular divergence, is up to eleven orders of magnitude higher compared to laboratory sources, enabling extremely fast measurements and allowing for high spatial and temporal resolution. In addition, synchrotron beamlines provide a high degree of experimental versatility, permitting a wide range of measurement configurations and making

them particularly well suited for *operando* characterisation. An illustration of a synchrotron is shown in **Figure 3.3** where the storage ring, insertion devices (blue and orange cubes representing the magnets of the undulators/wigglers) are represented. Each beamline is specific to an X-ray characterisation technique, for instance, at the Swedish synchrotron source MAX IV, Balder is specialised in X-ray absorption spectroscopy (XAS), HIPPIE in X-ray photoelectron spectroscopy (XPS), ForMAX for SWAXS imaging and DanMAX for X-ray tomographic microscopy. XAS and XPS will be discussed in this section, while SWAXS and XTM will be further discussed in sections 3.1.1 and 3.1.2, respectively.

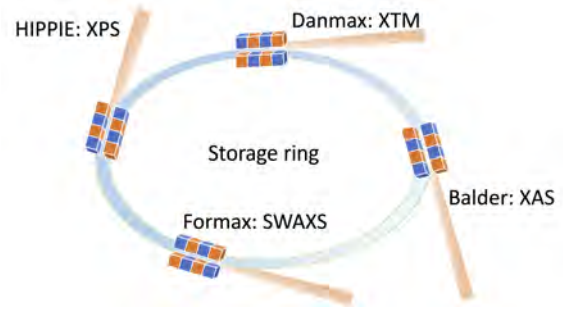

Figure 3.3: Illustration of the MAXIV synchrotron facility (Lund, Sweden) with its storage ring, insertion devices and some of the beamlines.

Absorption of X-rays by an atom experiences a sharp increase around the binding energy of the core electrons, known as the absorption edge. It is possible to scan the absorption edge with a high energy resolution in a technique called X-ray absorption near-edge structure (XANES) to obtain information on the oxidation state of the atoms, while the features beyond the absorption edge yield information on coordination numbers and bond lengths [128]. As an example, XANES has been used to investigate oxygen redox and transition metal charge compensation. Ogley *et al.* [129] used XANES on $LiNi_{0.8}Mn_{0.1}Co_{0.1}O_2$ cathode and observed no evidence of nickel oxidation at high voltage (above 4.2 V). XAS can also be used to address the polysulfide shuttling effect in LiS batteries. Jia *et al.* performed *operando* XAS and showed that a modified separator containing bismuth nanoclusters could stop polysulfides migration towards the counter electrode, significantly reducing the shuttle effect [130]. *Operando* XAS have a limited use in the soft X-rays regime, where X-rays with an energy below 1 keV have low penetration depth in the cell, which produces unreliable information [131].

In an XPS experiment, the kinetic energy of the ejected photoelectrons is measured and related to their binding energy, which can be used to identify chemical species, their oxidation state and binding environment. Because these photoelectrons are easily scattered by surrounding atoms, XPS is inherently surface-sensitive. The technique is widely used to investigate the SEI in batteries, for example, by identifying its organic and inorganic components [132]. However, performing XPS during

battery operation is challenging, as measurements are typically conducted under ultra-high vacuum, which restricts the use of liquid electrolytes. Moreover, both the liquid electrolyte and the insulating SEI layer attenuate the signal by limiting the number of photoelectrons that reach the detector. These factors make the development of *operando* XPS cells particularly challenging. As an example, Källquist *et al.* [133] used ambient pressure *operando* photoelectron spectroscopy to study lithium deposition on gold by indirect access of the interface, through the liquid meniscus in a beaker cell.

3.1.1 Small- and wide-angle scattering

SWAXS provide information on the structure and morphology of a material through elastic scattering of structures at a broad range of length scales, from atomic structure to the particle level and has been widely applied in battery research. The principal strength of WAXS lies in its ability to determine lattice parameters, identify crystalline phases, and quantify their relative fractions. SAXS, on the other hand, probes length scales characteristic of particle morphology (typically tens to hundreds of nanometres) or porosities and provides insight into internal structures and particle surfaces. The ability to track such structural evolution during battery cycling has been significantly advanced by synchrotron sources, where high brilliance and tunable energy enable high temporal resolution [13].

Building on these capabilities, WAXS has been particularly useful in elucidating the structural evolution of graphite during lithiation [40, 48, 49, 134, 135]. The lithiation of graphite is associated with an expansion of the inter-layer distance of the graphene sheets, which causes an overall volume change of the electrode. This effect was studied by Schweidler *et al.* [40], who used lab-scale *operando* WAXS to quantify volume expansion of graphite during lithium intercalation in a pouch cell at C/7. *Operando* WAXS provides continuous tracking of the transitions between the different stages of lithiation (1L, 4, 3, 2/2L and 1), and their lattice parameters. The authors followed the fraction of each lithiated stage to calculate the overall volume expansion of graphite throughout (de)lithiation, showing that even partial lithiation induces significant crystallographic strain and that total graphite expansion reaches 13 % at full lithiation (LiC_6).

The lithiation process is itself not occurring at the same rate throughout the electrode, creating heterogeneities that require the use of a focused X-ray beam to obtain spatial resolution at the electrode scale. Finegan *et al.* [48] used synchrotron XRD, with an energy of 72 keV on coin cells to map the lithiation front moving from separator to current collector under fast charging conditions. Severe depth heterogeneity was observed: near the separator, graphite rapidly reaches stage 1 (LiC_6), while deeper regions initially remain as graphite or stage 3. Simultaneously, the authors also addressed lithium plating, which was detected only within the first

20 μm from the separator, and explained by concentration gradients causing local overpotentials and creating favourable conditions for lithium plating [136]. Plated Li influences lithiation and can cause incomplete delithiation because LiC_6 and unlithiated graphite were found together, even after discharge. The depth-resolved measurements reveal how electrolyte transport limits both intercalation gradients and localised plating during cycling at high rates.

Similarly, Oney *et al.* used scanning WAXS to study the effect of graphite ageing and measured the depth profile of lithiation [49]. A cell with a PFA body was used, and a focused 3x3 μm^2 synchrotron beam (ID13, ESRF) with an energy of 23.5 keV scanned the electrode, producing a 35x28 pixels map in 2 minutes. The authors showed that ageing induces strong spatial variation in lithiated state, with inactive particles distributed non-uniformly through the electrode thickness. Regions near the separator show the highest inactivity, often remaining fully unlithiated or stuck in intermediate stages, while central regions contain lithiated yet electrochemically unresponsive particles. Two forms of inactivation were identified: "dead" graphite and "slow" kinetically hindered particles, demonstrating that lithiation heterogeneities fundamentally disturb reaction pathways in aged graphite. Overall, these two studies [48, 49] demonstrate how X-ray scattering can reveal the presence of lithiation heterogeneities, predominantly near the separator, with this effect becoming more pronounced at high current densities or in aged graphite.

SAXS and WAXS can also be used to study materials with less order than graphite, for instance, hard carbons. SWAXS can yield information on the surface of hard carbon particles, microporosities, and atomic arrangement, which are valuable parameters to study the sodiation of hard carbons [87, 90, 94]. As an example, a typical SWAXS pattern from a hard carbon powder is shown in **Figure 3.4**. The contribution at low q-values accounts for the surface of the hard carbon particles, which can provide information on the SEI formation on the particle's surface at the beginning of sodiation [120]. This would be reflected in a change of the slope at low q by increased roughness of the surface of hard carbon particles [137]. The characteristic shoulder at intermediate q comes from the difference in scattering length density between the micropores and the surrounding carbon matrix [95]. When sodium fills the micropores, this difference will decrease, which will lead to a decrease in intensity of the shoulder [90, 94].

Operando SAXS was used by Kistu Iglesias *et al.* [90] to quantify how synthesis temperature shapes the microstructure of hard carbon and influences the sodiation process. At low pyrolysis temperature (1100 °C), the slope region of the voltage profile (**Figure 2.8**) is more pronounced than the low voltage plateau, whereas at higher pyrolysis temperatures (1400–2000 °C), the opposite effect is observed. SAXS profiles show that higher pyrolysis temperatures lead to larger mean pore radii and higher micropore volume fractions, visible as increased scattering intensity of the

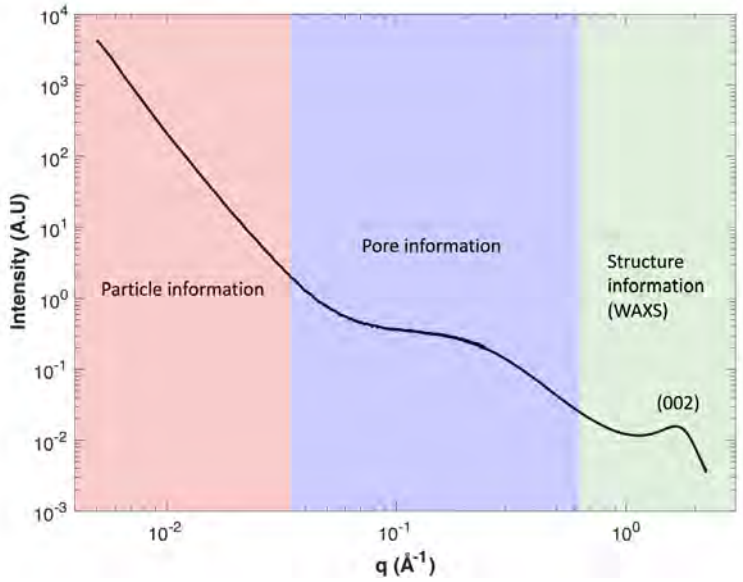

Figure 3.4: SAXS curve from a hard carbon powder. Low q values (red) are the contribution of the particles, the medium q range (blue) contains information on the micropores, and the high q region (green) is the wide-angle X-ray scattering (WAXS) range with crystal structure information.

micropore shoulder. By modelling the SAXS data, the pore size distribution could be extracted, and demonstrated that microstructural evolution with temperature directly affects sodium storage: hard carbon synthesised at higher temperatures stores more sodium in micropores in the plateau region because pores and pore volume are larger and more numerous, whereas lower pyrolysis temperature hard carbon shows small micropores and lower reversibility.

At higher q-values, the WAXS region in the scattering pattern of hard carbon shows a broad amorphous peak, often referred to as the (002) reflection peak, as it is analogous to the diffraction peak of the stacked graphene layers of graphite [87]. Morikawa *et al.* [94] showed that during sodiation, this peak shifts to smaller q-values, indicating an increased interlayer spacing associated with sodium intercalation. Additionally, the authors observed another broad peak at around q = 2.0-2.1 $Å^{-1}$, which was associated with pseudo-metallic sodium cluster (i.e., amorphous sodium clusters in the micropores [138]).

Operando WAXS can also be used to study lithium-sulfur batteries [100]. Conder *et al.* directly observed soluble lithium polysulfides in a working Li–S battery—species, typically invisible to diffraction due to the fact that polysulfides are in solution. Fumed silica was used as an electrolyte additive, enabling the detection of long-chain polysulfides when they adsorb on the separators, forming an organised nanometric surface layer that produces two broad diffraction peaks in WAXS. Tracking these peaks through cycling revealed the evolution of polysulfides across solid–liquid and

liquid–liquid reaction regimes and correlates their disappearance with the formation of crystalline Li_2S at the end of discharge.

3.1.2 X-ray tomographic microscopy

XTM takes advantage of X-rays to penetrate through and produce images with micrometric resolution. Synchrotron XTM has been used to study the degradation mechanism in lithium-ion batteries from the cell level down to active material particles. As an example of a degradation mechanism, lithium plating has been visualised by Ho *et al.* with XTM (8.3.2 beamline, Advanced Light Source, USA), and its interplay with lithiation heterogeneity inside graphite electrodes under fast-charging conditions [41]. A graphite/lithium half cell, in a PEEK body, was used, and a spring maintained mechanical pressure between the electrodes. The cells were lithiated at a desired state-of-charge, then measured with XTM while resting, and each scan took 10-15 minutes. Following a 1C lithiation, the formation of a mossy lithium layer at the graphite–separator interface was observed with XTM using a 22 keV beam, producing images at 2 μm spatial resolution. Digital volume correlation (DVC) was used to link volume change in the graphite electrode to the local state of charge. DVC revealed that this plated-Li layer creates a transport bottleneck, where graphite particles located tens of micrometres beneath the plated region remain under-lithiated, despite being far from the plating front. The state of charge mapping shows that areas directly below plated lithium can fall below 30 % lithiation even when the electrode as a whole receives a nominal 100 % state of charge. The results also showed that during a rest period that followed a plating at 6C, the difference in potential between plated lithium at the graphite/separator interface and under-lithiated graphite creates a current that strips plated lithium onto graphite particles, producing intense local ionic currents [59].

Lithium-sulfur batteries have been studied with XTM to visualise the morphological degradation of LiS composite electrodes built on carbon fibre current collectors [116]. Cells were cycled in coin cells and opened for XTM measurements after 1,2 and 10 cycles. XTM was performed at the BAMline beamline (Bessy, Germany) with an X-ray energy of 18.5 keV and a voxel size of 0.438 μm. After the first cycle, tomographic images show that sulfur particles shrink and diffuse into the porous current collector, and after 10 cycles, are re-deposited near the electrode top. The particle size systematically decreases with cycle number, which correlates with capacity fading.

Sadd *et al.* employ a glass capillary cell to achieve full-field *operando* X-ray tomographic microscopy, allowing the entire sulfur cathode to remain within the field of view during discharge [99]. XTM was performed at the Tomcat beamline (Swiss Light Source, Switzerland) at a X-ray beam energy of 21 keV and a field of view of 0.8x0.8 mm^2 and a voxel size of 0.325 μm. Each tomogram took 1 minute to

complete and was acquired every 30 minutes, which enabled continuous cycling at a C/10 current rate. XTM enabled direct, quantitative visualisation of sulfur, starting with the complete conversion of solid S_8 into soluble polysulfides early in the first plateau, which are not observable anymore once dissolved. Image sequences from *operando* tomography show that sulfur particles shrink and dissolve radially, with sulfur particles further away from the centre of the electrode dissolving first. After full dissolution of S_8, short-chain polysulfides convert to insoluble Li_2S during the second plateau. XTM slices reconstructed with Paganin phase-contrast [139] show a progressive greyscale increase across the cathode towards the end of the discharge, indicating the nucleation of Li_2S on the carbon/binder matrix. Because Li_2S particles are smaller than the 1 μm resolution, they do not appear as discrete particles but as a uniformly distributed high-intensity layer coating all available internal surfaces.

Tan *et al.* directly visualised where and how sulfur re-deposits during charging XTM [115]. XTM was conducted at the I13 beamline (Diamond light source, UK) with a 22 keV X-ray beam, producing tomograms with a 2.1 x 1.8 field of view and a voxel size of 0.81 μm, on a lithium/sulfur cell with a PFA body. Tomogram acquisition took 15 minutes, and the cell was held at open circuit during that time, then cycled for 15 minutes until the next tomogram. After complete sulfur dissolution at a C/5 current rate, elemental sulfur reappears only late in charge (85 % depth of discharge), but not as a uniform layer. Instead, preferential redeposition within the cathode microstructure was observed. Sulfur recrystallises first near the separator interface, indicating that polysulfide transport is rate-limiting, because regions closest to the separator are electrolyte-rich and experience the fastest access to incoming polysulfides. During charging, redeposited sulfur forms oriented clusters rather than returning to the initial uniformly dispersed morphology. These clusters are anchored along ridges and cracks of the carbon-binder matrix, especially near larger pores, showing that carbon-binder domain structure dictates nucleation sites.

3.2 Raman scattering

Raman scattering is a powerful technique to identify chemicals present in the battery electrode and electrolyte. Raman spectroscopy is particularly useful to study carbonaceous materials and provides useful information about their structural evolution when lithiated. **Figure 3.5** shows the different Raman bands of hard carbon with their associated vibrational movement. The D band represents sp^2 carbon atoms bond breathing (1350 cm^{-1}) while the G band represents bond in-plane stretching (1590 cm^{-1}). Deconvoluting the spectra provides more information about the nature of the defects (**Figure 3.5**): the D' band at 1620 cm^{-1} originates from vibrational movement of the surface graphene layers and is also associated with a stretching vibration [140]. The D4 and D3 bands at 1200 and 1500 cm^{-1} are associated with rings containing 7+ carbon and point defects, respectively [90].

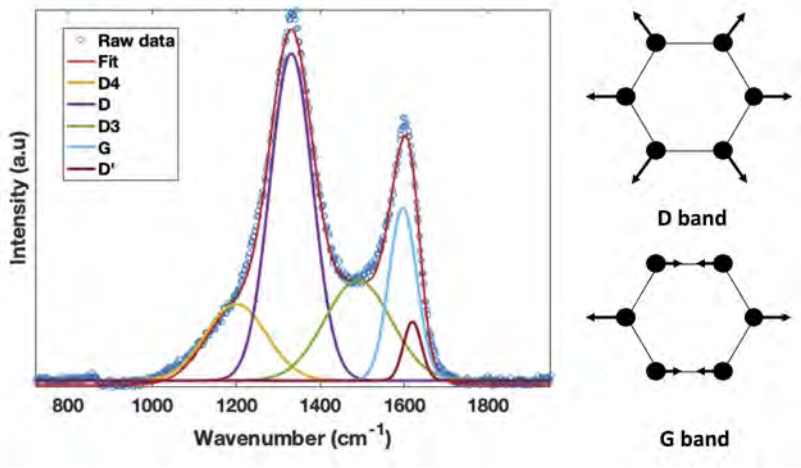

Figure 3.5: Raman spectra of a hard carbon sample with a deconvolution of the different bands and an illustration of the D and G bands vibrational movement.

The analysis of the bands allows us to understand the relation between defects in hard carbons and their pyrolysis temperature for its synthesis [90, 94] where it was found that lower temperatures (1000-1400 °C) form HC with higher defect concentration, while high temperatures (1500-2000 °C) produce more ordered HC with a structure closer to graphite. The sodiation process can be followed in HC with *operando* Raman spectroscopy, and the observation of the G band provides information on sodiation [120]. At higher voltage (from 1 V to 0.02 V), the frequency of the G band decreases due to the intercalation of sodium ions between the graphite-like layers of hard carbon and defect adsorption. At voltage below 0.02 V, the G band position remains constant, indicating that another sodiation mechanism has to take place, which is likely pore filling [90, 141].

Another way of investigating battery materials and components with Raman spectroscopy is to provide spatial information of the material through mapping an area of interest. Using a laser to scan the electrode is, for example, a way to locate the deposition of plated lithium [80, 142]. Lithium plating reacts with the SEI to form acetylide specie Li_2C_2, which serves as a marker of lithium deposition [81, 143].

Raman spectroscopy can be a complementary technique to X-ray tomographic microscopy since it is possible to measure the Raman shift of soluble species. As an example, polysulfides and radicals were identified with Raman spectroscopy by Sadd *et al.* [144], and the results pointed out that the use of polysulfides as catholyte (i.e., the cathode is in the electrolyte and there is no supporting salt) can increase the migration of polysulfides and improve the performance of a LiS cell.

Chapter 4

Experimental methods

This chapter aims to introduce the different methods that have been used in this thesis and the cell design required to perform *operando* measurements.

4.1 Cell design for *operando* X-ray experiment

Cell design for an *operando* X-ray experiment is crucial to consider and often requires special features depending on the technique used. The criteria that the cell should meet are diverse and often require making compromises on, for instance, the size of the electrode, stack pressure or volume of electrolyte. The field of view provided at synchrotron sources is usually a few millimetres, which forces the scaling down of the components of the cell compared to classical formats (coin cell or pouch cell) if the goal is to have the cell in the entire field of view. On the other hand, measuring only a portion of the electrode can be achieved to increase the spatial resolution and reduce the measurement time. Additionally, the cell design has to be somewhat close to a real cell to ensure similar electrochemical processes.

First, one needs to consider the materials that make up the body of the cell. Several materials have been used in *operando* cells, namely quartz, polyether ether ketone (PEEK) or perfluoroalkoxy alkanes (PFA) [41, 99, 115]. In **Paper III**, a quartz capillary tube was used because the background signal is low compared to PEEK and PFA in SWAXS imaging [145, 146]. The cell is shown in **Figure 4.1**. This cell design is not meant for performance, as it is lacking features that are otherwise essential in a standard cell. For instance, the capillary cell used did not have a separator or any mechanical pressure and used a large volume of electrolyte (approximately 10 μL of electrolyte for 0.1 mg of hard carbon).

The cell was assembled with a dip-coated pin in a hard carbon slurry and made of 85 wt.% HC, 10 wt.% PVDF binder and 5 wt.% carbon additives and then dried. This process was repeated until a few mg of electrode was coated on a stainless steel pin. Then the capillary was filled with electrolyte, and the other pin with sodium

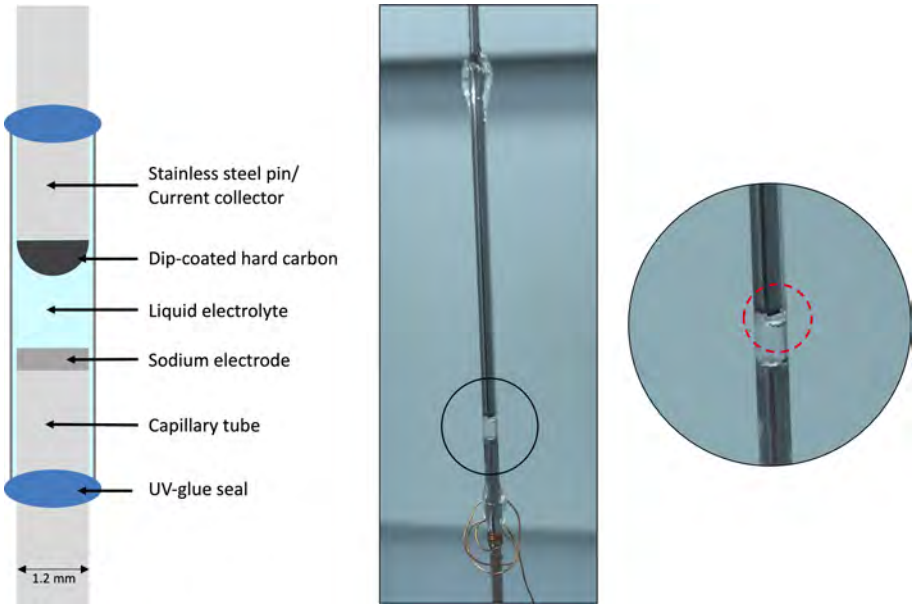

Figure 4.1: Schematic of the different components of the capillary cell with a photography image highlighting the formation of a gas bubble as one of the major drawbacks of the cell design [137]. Copper wires are soldered at the bottom and top.

metal was inserted. The cell's air-tightness was maintained by sealing the pin to the capillary with a UV-curable glue.

The small electrode diameter (in the range of 0.8 to 1.2 mm) means that it is possible to scan the entire electrode in a few minutes with a beam size of 15x25 μm^2. The small electrode size also means a good transmission signal through its thickness. Another advantage of the capillary cell is that the transparent glass, with no separator, allows direct observation of the electrode and electrolyte, meaning that quantitative analysis based on optical imaging could be carried out, as demonstrated in other work [99].

One of the issues of the capillary cell design is that it is extremely fragile because the capillary has a wall thickness of 150 μm to minimise the cell background. This means that the assembly procedure of the capillary cell is challenging and requires careful handling of the quartz tube. It is also difficult to precisely control the distance between the electrodes, which leads to a cell that cannot be reproduced exactly. Additionally, gas can be trapped between the pin and the capillary wall when assembling the cell. It can eventually move when handling the cell or simply by gravity move in the space between the electrodes (see the photograph in **Figure 4.1**). This can severely reduce the cell performance or even lead to cell failure if the bubble grows too big. Another issue comes from the dip-coated electrode on the pin, which makes it difficult to know the cell's actual capacity with great precision.

The capacity was determined based on the volume of segmented SWAXS images based on the density of hard carbon (1.5 mg/cm^2).

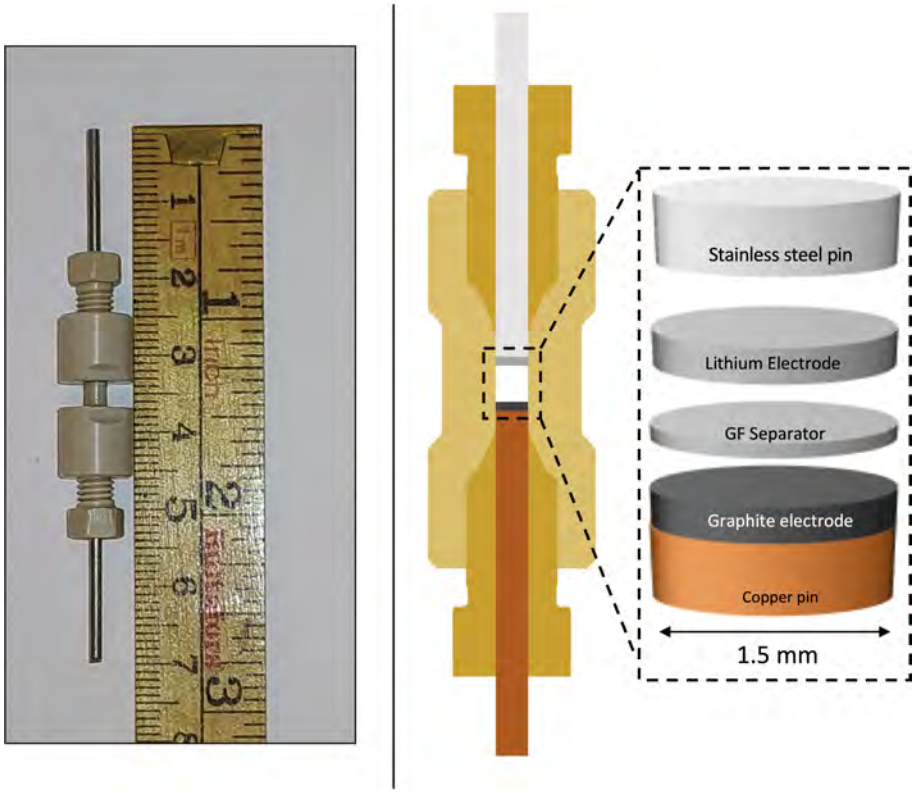

Figure 4.2: Photograph and scheme of the tomography cell used for XTM experiments, with a blow-up view of the battery stack showing the graphite-lithium half-cell configuration.

An alternative cell design used for the XTM experiment is presented in **Figure 4.2** with an illustration of the battery stack. In the experiment carried out at the ID19 and ID15a beamlines (based on **Paper I** & **IV**, respectively) at the European Synchrotron Radiation Facilities (ESRF) a cell made of (PEEK) with an internal diameter of 1.5 mm was used. PEEK has a high X-ray transmission and is suitable as a battery casing because of its good chemical stability. The middle section of the cell (where the electrode stack is located) was further cut to reduce X-ray attenuation. The pressure applied between the two electrodes is made by two metal plungers (used as current collectors) held in place by ferrules and screws that ensure the airtightness of the cell. The FOV achieved at ID19 (**Paper I**) was 1.48 x 1.48 mm^2, and with an electrode diameter of 1.5 mm, 97 % of the electrode can be captured in the FOV. At the ID15a beamline (**Paper IV**), the FOV was 0.82 x 0.83 mm^2, meaning that only 53 % of the electrode was in one tomogram. This difference is due to the fact that the half acquisition method was used at ID19, extending the FOV (see section 4.2.2).

The PEEK cell design was improved by Dr Rizell [147] by the addition of a spring

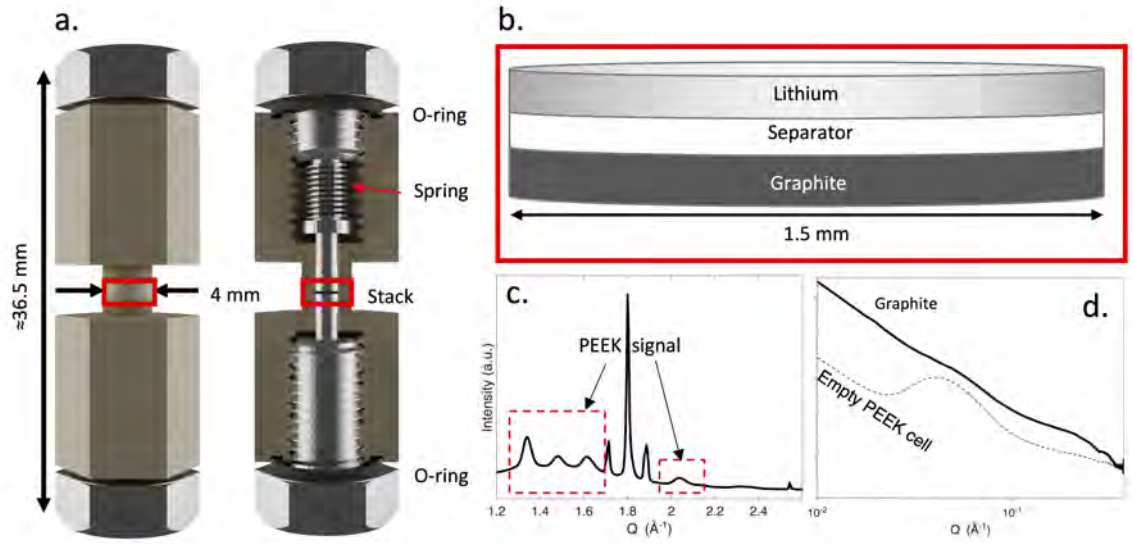

Figure 4.3: a) Schematic of the improved tomography cell (based on the work of [147]), with an additional spring that applies mechanical pressure to the battery stack illustrated in b). WAXS contribution from the PEEK cell is highlighted in c), and for SAXS in d).

and rubber o-rings to ensure the air tightness (**Figure 4.3a**). The spring provides mechanical pressure between the electrodes, which can improve the cell's coulombic efficiency. This design is closer to realistic cells and should yield electrochemical processes closer to industrial batteries. This design was used to perform scanning SWAXS as the ForMax beamline (MAXIV, Sweden) on a graphite/lithium cell (**Figure 4.3b**). As mentioned above, PEEK has a scattering signal (**Figure 4.3c,d**) with peaks in WAXS (1.3-1.7 $Å^{-1}$ and 2.04 $Å^{-1}$) and in SAXS at mid-q, measured on an empty PEEK cell. In SAXS, the cell's background signal was subtracted, whereas in WAXS, since the signal does not overlap with the graphite signal, only a linear background subtraction was used.

4.2 Characterisation methods

This section introduces the characterisation methods employed in this thesis. The X-ray-based techniques contain small- and wide-angle scattering as well as tomographic microscopy, while visible-light scattering is used in Raman spectroscopy.

4.2.1 Small and wide-angle X-ray scattering

Small- and wide-angle X-ray scattering (SWAXS) are characterisation methods that take advantage of the elastic scattering of X-rays by a material. SAXS provides information on particle size and shape, while WAXS addresses crystallinity and atomic arrangement. Small angles are generally defined between 0.1 and 10 °, thus,

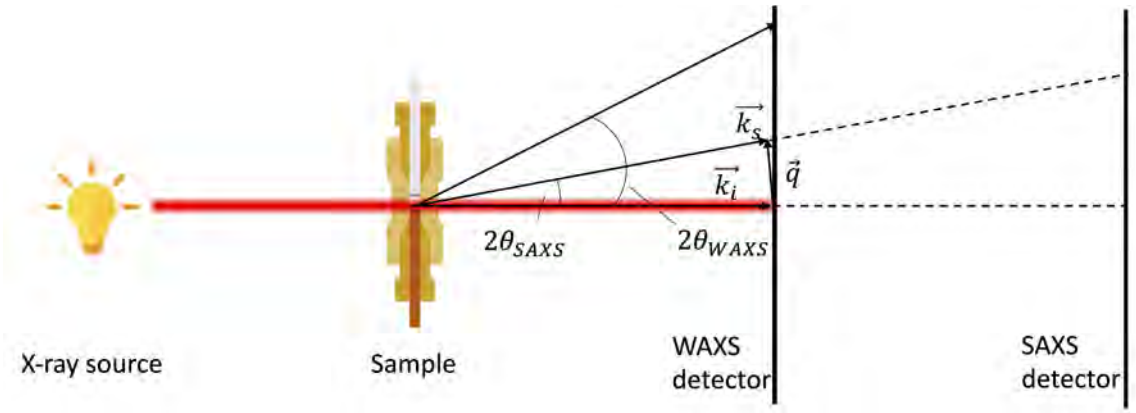

Figure 4.4: Schematic of a SWAXS setup in transmission mode. When the detector is placed close to the sample, it captures the scattering at wide angles, while placed further away, it captures smaller angles.

SAXS usually probes particles and structures from 1 to 100 nm [148] while at wide angles (typically above 5-10 °), WAXS probes inter-atomic distances, usually at the Ångstöm length scale.

A typical SWAXS setup in transmission mode is shown in **Figure 4.4**, where an incident X-ray beam, defined by the wave vector $\vec{k_i}$, impinges on the sample and is elastically scattered at the angle 2θ. The scattered light is represented by the wave vector $\vec{k_s}$. Since the scattering is elastic, the magnitude of $\vec{k_i}$ and $\vec{k_s}$ is equal, only their direction is different. The magnitude of the scattering vector $\vec{q}$ describes how much the wave vector has changed in the reciprocal space and is given by:

$$|\vec{q}| = |\vec{k_s} - \vec{k_i}| = \frac{4\pi}{\lambda} \sin\theta \tag{4.1}$$

where λ is the X-ray wavelength and θ is half of the scattering angle. The intensity of the scattering signal $I(q)$ depends on the ability of a material to scatter light, which is defined by the scattering length density ρ, which is proportional to the electron density. The intensity of the signal recorded by the detector is the squared Fourier transform of the scattering length density over the entire volume V of the illuminated material:

$$I(q) = \left| \int_V \rho(r) e^{-iqr} dr \right|^2 \tag{4.2}$$

In practice, resolving features in a scattering pattern depends on the difference in scattering length density of a material and its surroundings [149]. Using q instead of the scattering angle is a convenient way of comparing scattering patterns, independently of the wavelength of the incident light. Typically, the SAXS detector is placed a few meters away from the sample, while the WAXS detector is placed up to one meter away.

The principle behind WAXS (also called X-ray diffraction, XRD) is that when an

X-ray beam of wavelength λ hits an atom, it is scattered in every direction by the electron cloud. Constructive interferences will occur at the angle θ by atoms from two adjacent planes separated by the distance d when Bragg's condition is met and is illustrated in **Figure 4.5**.

$$n\lambda = 2d\sin\theta \quad (n \in \mathbb{N}^*) \tag{4.3}$$

The characteristic distances measured with SWAXS (atomic or particle distances in WAXS/SAXS, respectively) can be approximated by combining equation 4.3 and 4.1:

$$d = \frac{2\pi}{|\vec{q}|} \tag{4.4}$$

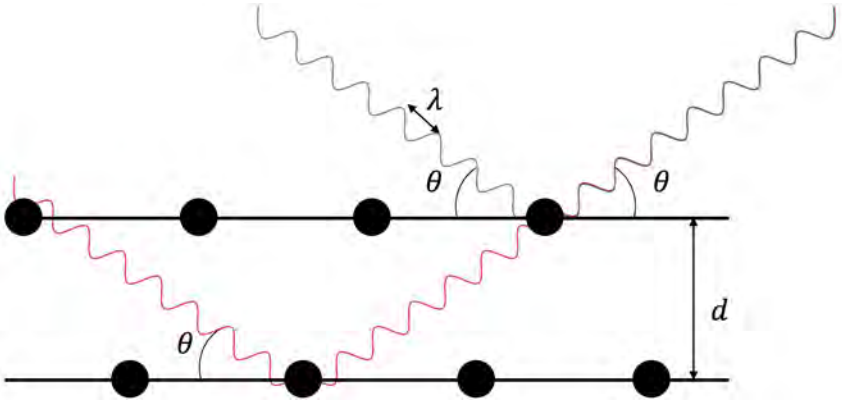

Figure 4.5: Schematic illustration of Bragg's condition.

In this thesis, imaging of graphite and hard carbon electrodes was done with scanning SWAXS, where a focused X-ray beam raster-scanned the material. Scanning SWAXS produces a two-dimensional grid of measurement points, where each point corresponds to a pixel in the resulting image. Each pixel of the image is a scattering pattern. **Figure 4.6** shows a graphite electrode that was scanned with a focused X-ray beam. The detector images for each pixel are azimuthally integrated to produce a 1-dimensional scattering curve. In this example, we can observe the scattering of PEEK that made the body of the cell in the 1.2-1.7 $Å^{-1}$ range, and the sharp crystalline peaks of graphite in the 1.7-1.9 $Å^{-1}$ range. These resulting 1D scattering curves represent the average scattering across the length of the electrode (1.5 mm). The strength of scanning SWAXS is that it provides local information about the microstructure and atomic arrangement, which makes it possible to detect heterogeneities within the electrode. The spatial resolution of the experiment is limited by the size of the X-ray beam, which was at the ForMAX beamline 48x14 μm^2, while at the cSAXS beamline, the beam size was 25x15 μm^2.

In order to extract useful information from WAXS data, a fit of the diffraction peaks has to be done. If the measurement was done with a perfect instrument on a perfect crystal, the peak shape would be extremely sharp; so describing a peak shape with

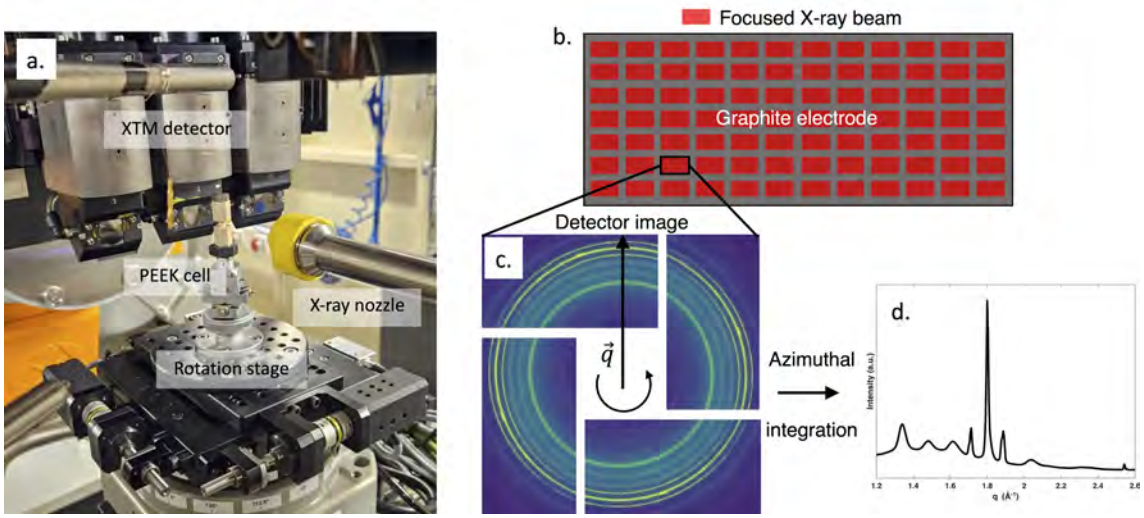

Figure 4.6: a) Picture of the ForMax beamline with the different elements of the experiment. b) Example of a scanning WAXS experiment with the corresponding detector image (c) of a scattering pattern obtained for one pixel and (d) its azimuthal integration.

a mathematical expression is to account for the peak broadening. WAXS peaks have a broadening caused by the instrument (e.g., size of the beam, wavelength distribution or detector response) which is best modelled by a Gaussian function $G(x)$. Another source of broadening comes from the sample being non-ideal, i.e., there is a distribution in crystallite size and strain effect, which can be modelled by a Lorentzian function $F(x)$ [150]. A good representation of peak broadening can be achieved by the convolution of a Gaussian and a Lorentzian function, called a Voigt function. However, the convolution is computationally demanding, so a good balance between physical realism and computational efficiency is achieved by using a pseudo-Voigt function defined by $PV(x) = \frac{1}{2}G(x) + \frac{1}{2}F(x)$, where:

$$G(x) = \frac{1}{\sigma\sqrt{2\pi}} e^{-\frac{(x-\mu)^2}{2\sigma^2}}; \quad F(x) = \frac{1}{\pi} \frac{\Gamma/2}{(x-\mu)^2 + (\Gamma/2)^2} \tag{4.5}$$

σ is related to the full width at half maximum (FWHM, Γ) by $\Gamma = 2\sqrt{2\ln 2}\sigma$ and μ is the position of the maximum. In this thesis, the WAXS peaks were fitted using a pseudo-Voigt profile and a MATLAB built-in function `lsqcurvefit` to find the parameters μ and σ.

An example of a fit is shown in **Figure 4.7**, where the different phases of lithiated graphite can be identified based on their main reflection peaks in the region 1.7-1.9 Å^{-1} according to section 2.3. The stage Gr' refers to the early lithiation phase of graphite, where lithium is diluted in graphite, which could be either stage 1L or stage 4 [45]. Fitting the WAXS curve yields the area of each peak, which enables

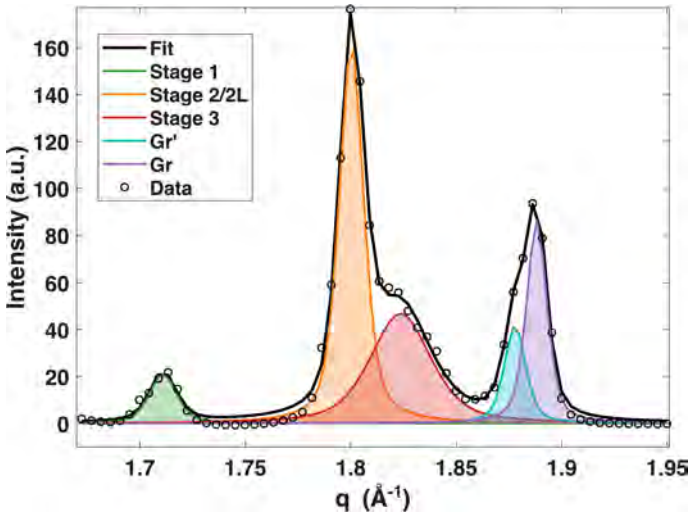

Figure 4.7: Fit of a WAXS pattern of the different phases of lithiated graphite

the determination of the phase fraction in the electrode under the assumption that the sum of all phases is equal to 1.

4.2.2 X-ray tomographic microscopy

X-ray Tomographic Microscopy (XTM) is a particularly powerful method to access the bulk of material and get detailed 3D information on micrometre length scales. It is common to perform XTM at synchrotron radiation facilities where the high flux enables the collection of fast tomograms at high resolution, even less than 1 μm. Additionally, in a synchrotron-based experiment, it is easy to tune the beam energy (in the range of 10 keV to 100 keV) and use a beam to reach high contrast and spatial resolution.

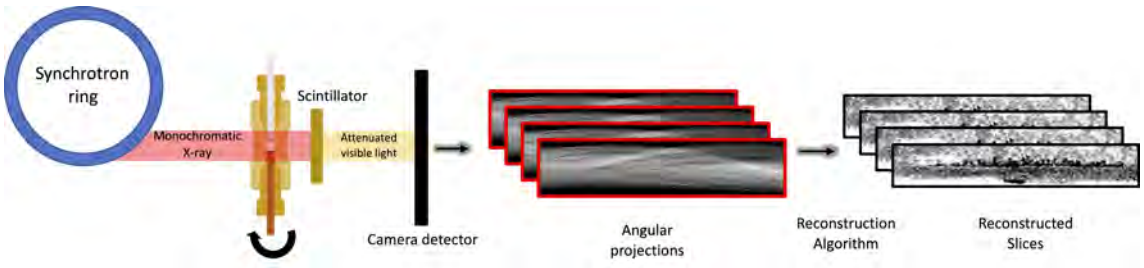

Figure 4.8: Schematic of an XTM experiment at a synchrotron with initial data reconstruction steps.

A typical layout for an XTM experiment is shown in **Figure 4.8**. The monochromatic X-ray beam illuminates the sample mounted on a rotation stage. The transmitted signal is converted to visible light and is captured by a camera to produce raw radiographs. Radiographs taken at different angles make a set of angular projections that are computationally reconstructed to form 3D images [86]. The transmitted

signal is attenuated by the sample according to the Beer-Lambert law:

$$I = I_0 e^{-\mu d} \tag{4.6}$$

where I is the transmitted beam intensity, I_0 is the intensity of the incoming beam, d is the thickness of the material and μ the linear attenuation coefficient. It is the differences of μ of each material that composes the sample that allows for the determination of the different phases, since it is linked to the density of a material:

$$\mu = \frac{\rho Z^4}{AE^3} \tag{4.7}$$

where ρ is the density, Z the atomic number, A the atomic mass and E the X-ray energy. From Equation 4.7, it becomes clear that the beam energy must be carefully selected when designing an XTM experiment to achieve sufficient contrast between the materials within the sample.

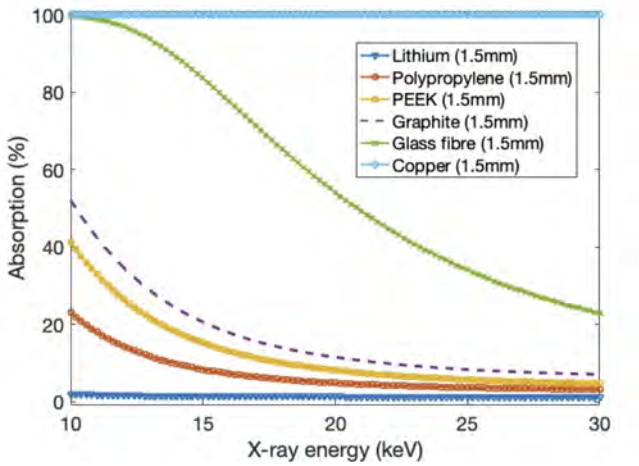

Figure 4.9: Calculated absorption as a function of X-ray energy of different cell components in a Li/graphite cell. The calculation has been made by using the website of the Centre for X-ray Optics at Lawrence Berkeley National Laboratory: `https://henke.lbl.gov/optical_constants/filter2.html`.

Figure 4.9 shows the simulated transmission of the components of a Li-metal/graphite cell as a function of X-ray energy. The thickness used in the simulation is typical for the diameter of a cell used for tomography in this thesis. Copper almost fully absorbs all the X-rays and can potentially shadow materials situated between it and the detector, in contrast to lithium, which is almost X-ray transparent. The separator made of glass fibre could potentially be an issue considering its high absorption, but it can also bring a good contrast to the materials of interest (graphite, lithium). If the energy is too low, the transmitted beam will be attenuated too much, and if the energy is too high, the contrast between the materials in the cell will be poor. Theoretically, attenuation contrast should be around 13 % [86] so a

suitable beam energy range can be 25-30 keV (**Figure 4.9**). An important aspect to consider is also the potential damage that the beam can cause to the sample. The exposure to high X-ray doses can induce material damage, particularly when using high-brilliance synchrotron sources. Beam-induced damages include the breakdown of the electrolyte or the deactivation of the electrode active material [151, 152].

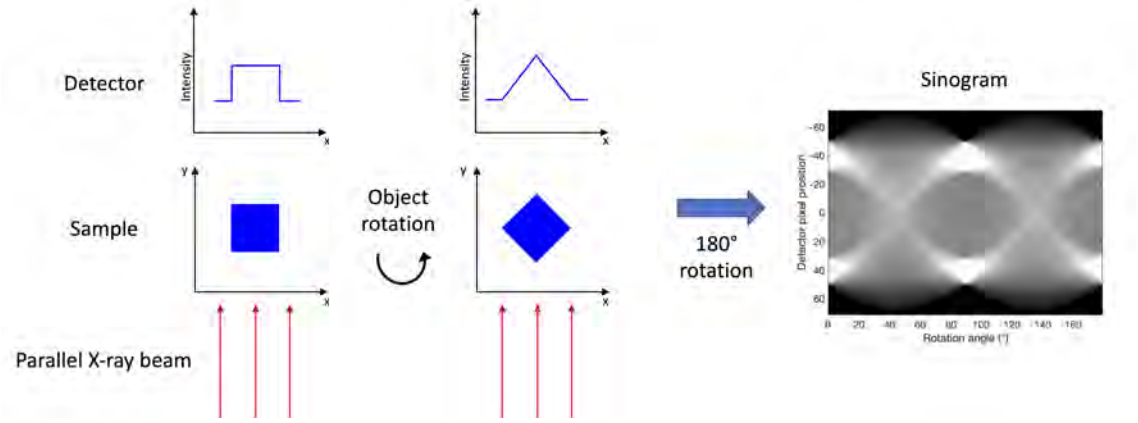

Figure 4.10: 2D illustration of an object absorbing X-rays and its projection on the detector at two different rotation angles. The sinogram is the combination of all rotations for one row of the detector.

A simplified example of a tomography experiment on a single-phase object and the projection on the detector is illustrated in **Figure 4.10**. The intensity profile is different depending on the angle of rotation, and each angular step will give a projection on the detector. The compilation of these projections on the detector is called the sinogram. It is possible to reconstruct the original object from the sinogram with a reconstruction algorithm. The reconstruction algorithm is based on the Fourier slice theorem, which states that the 1D Fourier transform of a projection of the object is equal to the 2D Fourier transform of the absorption coefficient μ, evaluated along one slice [86]. The reconstruction of the projections is performed in 3 steps: (i) take the Fourier transform of the sinogram (which is all the projections), (ii) apply a high-pass filter, and (iii) use the Fourier slice theorem by taking the inverse of the 2D Fourier transform of the filtered set to obtain μ. This algorithm, called Filtered Back-Projection (FBP), can reconstruct the original object based on the attenuation coefficient and is commonly used in XTM experiments. The filtering step is essential to alleviate artefacts due to the finite number of projections since the 2D Fourier space cannot be mapped completely and some data are missing at high frequencies, making simple back-projection often blurry compared to the original image, see **Figure 4.11**. Typically, a high-pass filter (such as the Ram-Lak filter) is used in the reconstruction algorithm.

In addition to attenuation, the X-rays can also be refracted, and the complex re-

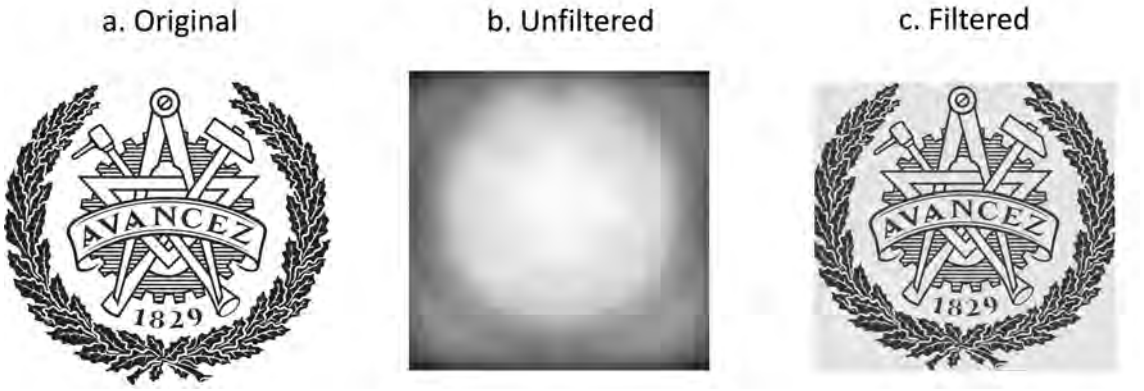

Figure 4.11: a. Original image of Chalmers logo, b. simple back projections reconstructed image and c. with the addition of the filtering step.

fractive index can be expressed as:

$$n = 1 - \delta + i\beta \tag{4.8}$$

where δ is the refractive index decrement and represents the change in phase of the wave, and β is the complex attenuation coefficient, which is related to the absorption coefficient ($\mu = 4\pi\beta/\lambda$). The phase change also yields information on the contrast of the object, but the detectors only measure the attenuation and are not sensitive to phase change (also known as the *phase problem* [127]). A common route to obtain the phase information with attenuation-based data was proposed by Paganin *et. al* [139]. The Paganin method works by filtering during the reconstruction of the high frequencies produced by edges in a material and improving the contrast of images.

There are also other important parameters to consider in an XTM experiment, such as the field of view (FOV) and the pixel size. The detector is composed of a pixel array that has a certain size (e.g., a PCO Edge HS camera has 2560*2160 pixels with a size of 6.5 μm) and, when combined with a magnification lens, will give the voxel size. With the example of a PCO Edge camera combined with a x10 objective, the voxel size is 0.65 μm and FOV is 1664 μm in height and 1404 μm in width, and, with a x20 objective, the voxel size is 0.325 μm, and the FOV is 832x702 μm^2. Lowering the voxel size to be able to resolve smaller objects with a larger magnification is done at the cost of a smaller FOV. However, if the sample doesn't fit in the entire FOV, it is possible to perform "half acquisition" (**Figure 4.12**) tomograms where the sample is displaced so that the rotation axis is close to the edge of the FOV and the sample is rotated over 360 ° instead of 180 °. This is extending the FOV by a factor of nearly two at the cost of doubling the acquisition time (the sample has to rotate an extra 180 °) and also quadrupling the raw data produced. Half acquisition tomograms were done in the experiment in **Paper I**, with a FOV of 1448x1448 μm^2 and allowed to capture 97 % of the graphite electrode.

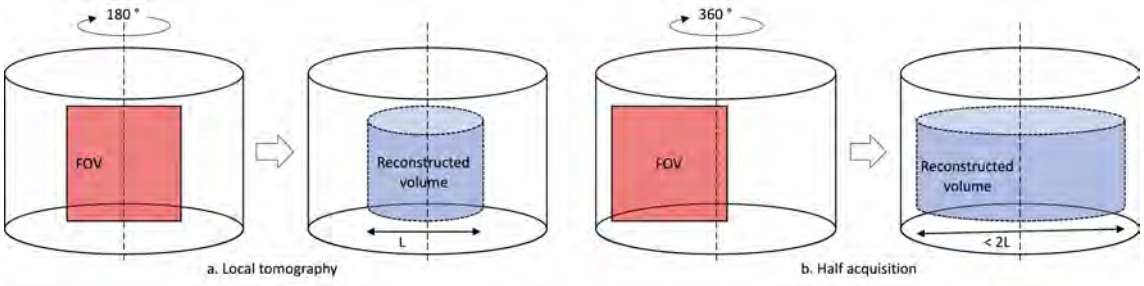

Figure 4.12: Comparison between local tomography (a), where the sample represented by the white cylinder is bigger than the FOV and half acquisition that doubles the FOV (b).

The resolution in the experiment is the size of the smallest feature that can be distinguished in an image. With a 3D volume from a tomographic reconstruction, the resolution is about 3 times the size of a voxel since at least 3 voxels are needed to form an interface. As an example, the voxel size given by a detector was 0.332 μm at the ID19 beamline, giving a resolution of approximately 1 μm. Practically, the determination of the actual spatial resolution can be done by plotting a line profile of the intensity along a sharp interface. **Figure 4.13** shows an interface between a pore and a graphite particle where a line was drawn over the interface. The intensity profile of this line is plotted, and from this plot, it is possible to extract the image resolution. From **Figure 4.13**, the resolution is about 1.5 to 2 μm, which is slightly higher than the estimation from the voxel size (1 μm).

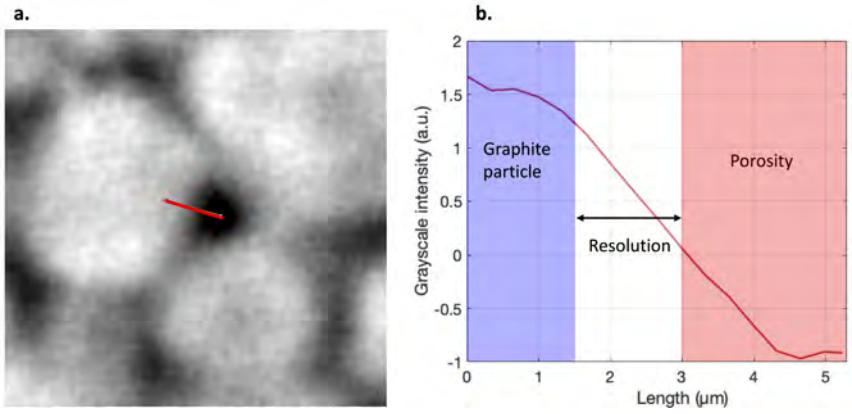

Figure 4.13: Determination of the resolution in a tomographic image. a. Zoomed tomographic 2D slice where a line is drawn at a sharp interface between a graphite particle (in bright colours) and a pore (dark). An approximation of the resolution is given by the line intensity profile in b. at 10-90 % of maximum and minimum intensities.

Getting quantitative data from XTM is often done by segmentation of the 3D data, where the greyscale images produced by XTM have different values that can help separate the materials present. A simple approach to realise that is to set a threshold

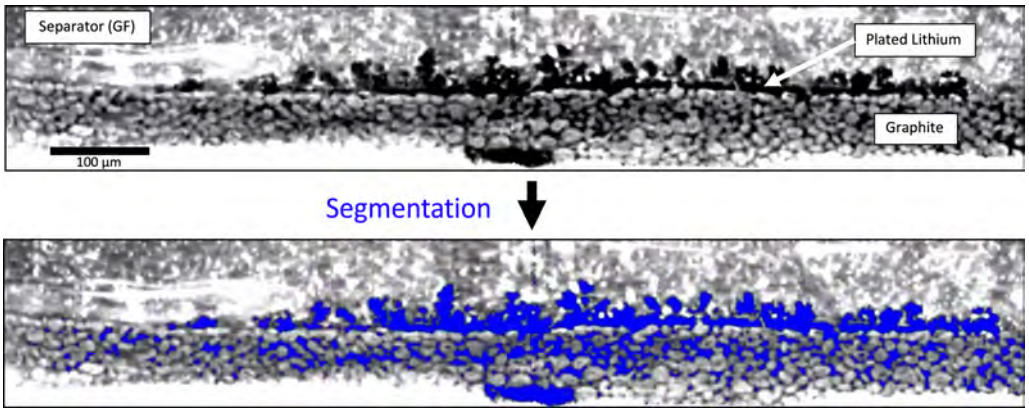

Figure 4.14: Example of segmentation of one tomographic slice with the different components of the cell (glass fibre separator and graphite anode). A blue overlay indicates the dark pixel that can be identified as plated Li.

and create a binary image with the value 1 for every pixel above the threshold and 0 for the rest. That way, it is possible to quantify the number of voxels (and thus the volume when multiplied by the voxel size) of one phase. **Figure 4.14** shows a tomographic slice of a Li/graphite cell with a glass fibre separator and copper current collector. All the dark pixels in **Figure 4.14** are identified as one phase (plated lithium), and the other materials (graphite, copper, separator) are left out. From here, it is possible to quantify the amount of plated lithium. One issue with this simple segmentation approach is illustrated by this example, since the pores filled with electrolyte would also be identified as lithium. Further analysis must then be carried out to only include relevant data from the tomographic slices, such as defining a region of interest (ROI), refining the threshold value, or changing the segmentation method (e.g., growing a mask from a seed, texture segmentation or watershed segmentation). On challenging datasets, a deep learning-based approach can be used. It consists of manually labelling a selection of images as a training sample for a neural network, capable of segmenting more difficult cases.

4.2.3 Raman scattering

Raman spectroscopy takes advantage of the inelastic scattering of visible light by a molecule. The electromagnetic field of a monochromatic laser induces a dipole moment in the molecule due to its polarisability, which is the ability of a molecule to deform its electron cloud. When an incident light with a frequency v_L and energy hv_L (h is Planck's constant) hits a molecule, a light-scattering event occurs. Since the energy of the photon is greater than the difference between the ground state and the first molecular vibrational state (state "0" and "1" in **Figure 4.15**), the molecule reaches a "virtual" energy state (represented by dashed lines in **Figure 4.15**). From the virtual state, the molecule will de-excite spontaneously, back to a lower energy state and emit a scattered photon. If this photon has the same energy as the incident

laser, the phenomenon is called Rayleigh scattering and is the most probable event. Raman scattering occurs when the scattered photon has a different energy compared to the incident photon, and this event is about 1000 times less likely to happen than Rayleigh scattering [153]. Two cases for Raman scattering can be distinguished: Stokes scattering is when the photon has a smaller energy than the incident photon, and anti-Stokes is when the molecule was already in an excited state "1", and the de-excitation brings it back to the ground state, generating a photon with a greater energy than the incident one. In a Raman spectrum, the Rayleigh scattering is filtered out, and typically the wavenumber of the Raman shift is used $\Delta\tilde{\nu} = (\frac{1}{\lambda_L} - \frac{1}{\lambda_m})$ (in cm^{-1}) instead of the photon wavelength or energy. This makes the Raman shift the same, regardless of the laser wavelength and allows the comparison of spectra between instruments.

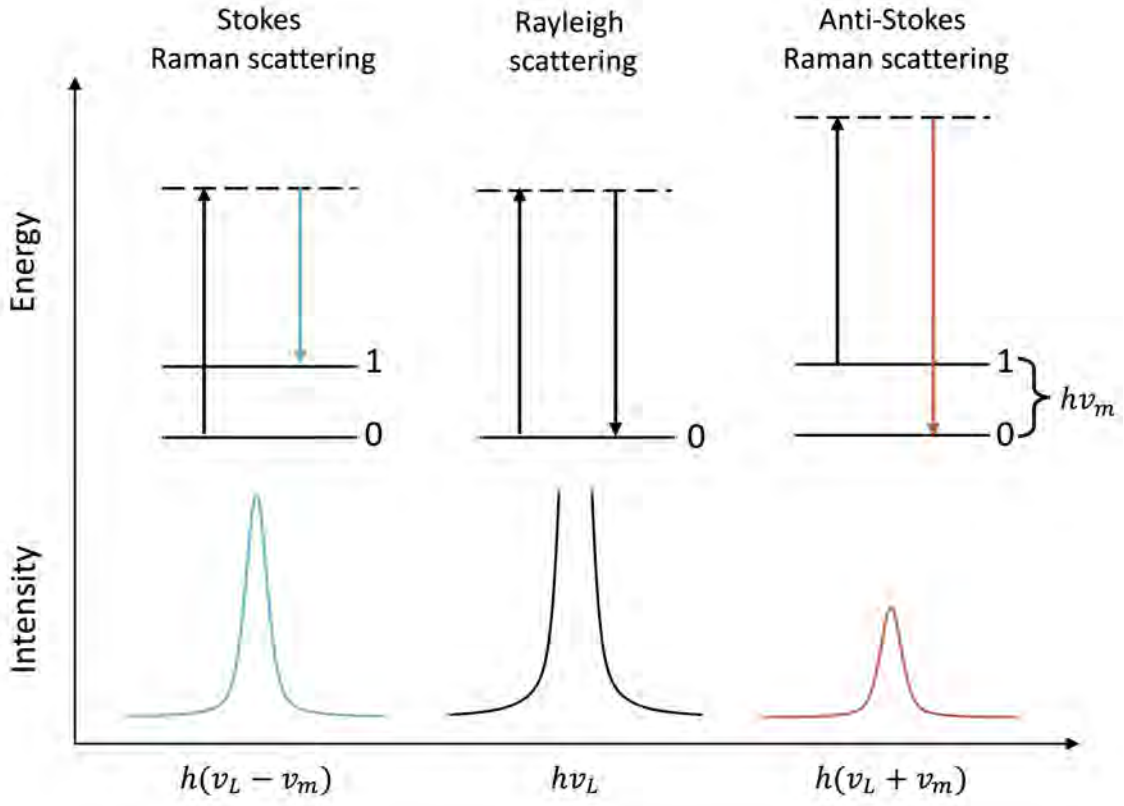

Figure 4.15: Energy diagram of the Stokes, anti-Stokes and Rayleigh scattering. The upward back arrows represent the energy of the incident photon, and the colourful downward arrows the energy of the scattered photon.

The frequency ν of the vibration associated with a Raman band is related to the masses of the atoms m_1 and m_2 and the bond force between them K (**Figure 4.16**):

$$\nu = \frac{1}{2\pi}\sqrt{K(\frac{1}{m_1} + \frac{1}{m_2})} \tag{4.9}$$

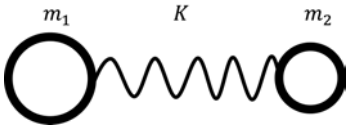

Figure 4.16: Schematic representation of a diatomic molecule m_1 and m_2 with a bond force K.

There are different types of vibrations, and the allowed movement depends on the symmetry of the molecule. The movement includes symmetrical and anti-symmetrical stretching (in-plane change of the bond length), scissoring (or bending, in-plane change of the bond angle), rocking (in-plane oscillation of the angle of a group of atoms), wagging (out-of-plane change of the bond angle) and twisting (oscillation out of plane of a group of atoms).

Raman scattering is often regarded as a surface-sensitive technique because the laser must directly interact with the sample to generate scattering events. The total scattered signal depends on the probed volume, which is determined by the laser cross-section and the skin penetration depth, δ:

$$\delta = \sqrt{\frac{1}{\pi f \mu \sigma}} \tag{4.10}$$

where f is the laser frequency, μ the magnetic permeability, and σ the electrical conductivity. A stronger Raman response can be achieved by increasing the laser wavelength, thereby enhancing the penetration depth. Conversely, highly conductive materials such as metals generally yield weak Raman signals due to their very limited penetration depth.

Chapter 5

Results

This chapter presents the results of the work carried out in the thesis, and also includes the papers attached. It highlights how X-ray imaging techniques were employed to investigate different battery materials and also presents complementary results from Raman spectroscopy not included in the attached papers. First, the detection of metal plating on carbon electrodes using XTM and WAXS is presented. This is followed by the use of scanning SWAXS as a tool for visualising heterogeneities within carbon-based electrodes. Finally, the chapter discusses how quantitative information can be extracted from imaging techniques to gain insight into degradation phenomena.

5.1 Metal plating in carbon electrode

5.1.1 X-ray methods

In **Paper I**, *operando* XTM was used to detect the presence of lithium plating on a graphite electrode and follow its evolution during lithiation and delithiation. The graphite/lithium cell presented in **Figure 4.2** was lithiated at 1C for one hour, followed by delithiation, also at 1C until the voltage reached 3 V. During this process, tomographic scans were acquired every 10 minutes, with 4000 projections distributed over 360 ° with an exposure time of 15 ms per projection, bringing the total measurement time for one tomogram to 60 s with the half acquisition method. **Figure 5.1** shows the voltage profile and reconstructed cross-section slices during the lithiation and delithiation cycles. Graphite appears as grey particles, the electrolyte fills the glass fibre separator as a grey phase with bright spots above the graphite electrode and the copper current collector, which attenuates all the X-rays, is the bright phase at the bottom. At around 35 minutes into the lithiation and onwards (**Figure 5.1e-g**), a new black phase, identified as lithium, appears at the interface between the graphite electrode and separator. Other interfacial phenomena, such as SEI, cannot be mistaken with plated lithium in those images because SEI is usually 10-50 nm

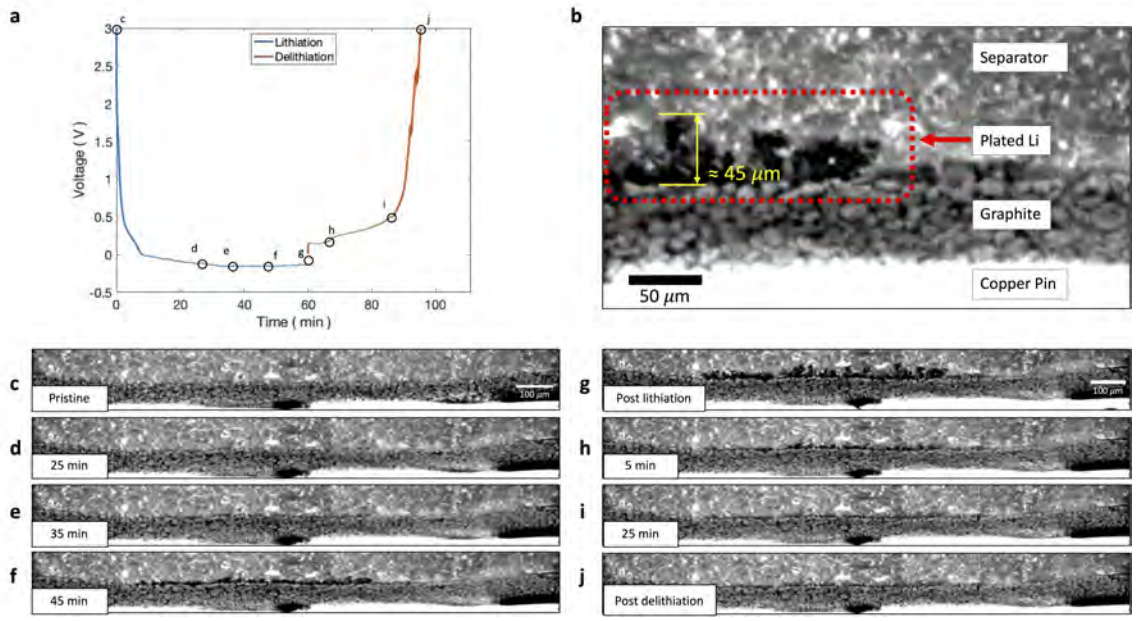

Figure 5.1: a) Voltage profile during lithiation/delithiation of graphite at 1C, with circles indicating when tomograms were taken. b) Zoomed in reconstructed vertical slice after lithiation for one hour. Cell components are indicated together with the identification of plated Li. Reconstructed vertical slices during lithiation (d–f) and delithiation (h–i). Tomograms of the pristine electrode, post-plating and post-stripping (c, g, j) were taken at open circuit voltage.

thick [154], and the plated lithium observed in all cells has a thickness of several orders of magnitude higher (10-100 μm). Moreover, the image resolution is around 1 μm, making the observation of SEI impossible.

Plated lithium grows into tall and fractal structures (dendrites) at the interface and even inside the separator (**Figure 5.1b**). The images from delithiation (**Figure 5.1h-j**) show that plated lithium is being stripped away, although not completely, since a thin layer of lithium remains at the end of delithiation, which is believed to be "dead lithium", i.e., Li which is electrochemically inactive.

The work in **Paper I** also involved the comparison between electrolyte additives. As it was stated in section 2.4.1, VC and LiFSI are two SEI-modifier additives commonly used in lithium-ion batteries. VC is known to create a mechanically strong polymeric SEI, while LiFSI forms a SEI rich in inorganic compounds such as LiF. These differences in SEI composition could explain some differences in the morphology of plated Li observed in **Figure 5.2**. With the baseline electrolyte, a rather uniform layer of plated Li is observed at the graphite separator interface, which could be associated with "mossy" lithium. With additives in the electrolyte, the morphology of the deposition is rather different, with more dendritic-like structures being observed.

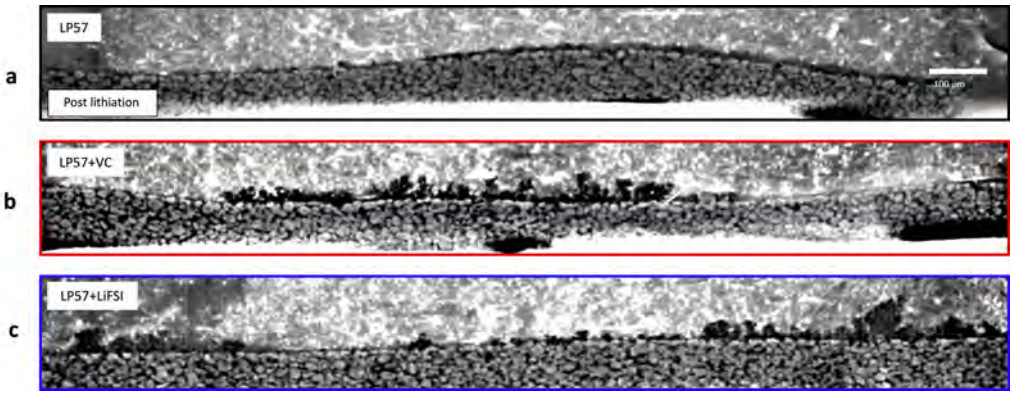

Figure 5.2: Cross-sectional images from the end of lithiation for the cells with a) LP57 b) LP57 + VC, and c) LP57 + LiFSI electrolytes.

From the tomographic images, lithium plating can be reliably identified only at the graphite–separator interface, where lithium provides strong contrast against the other cell components. However, as illustrated in the segmentation shown in **Figure 4.14**, additional pixels within the bulk of the electrode could be classified as lithium from greyscale thresholding. The space between graphite particles is expected to be filled with electrolyte, yet they exhibit a greyscale intensity close to that of lithium. This similarity makes it challenging to determine whether these features correspond to actual lithium plating or are just the normal bulk electrode. One could expect to see an expansion of this black phase and increasing inter-particle distance in the case of plated lithium in the bulk electrode, but this observation is not obvious from the tomographic images alone and would require further segmentation work.

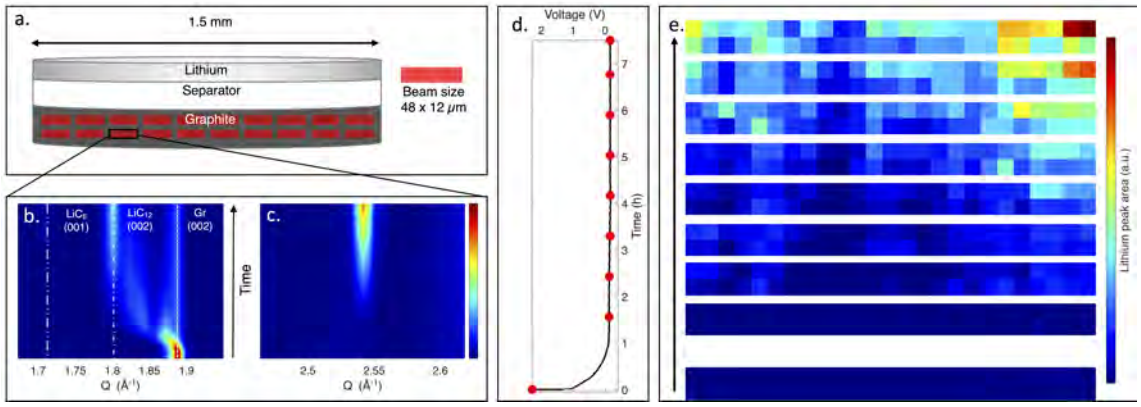

Figure 5.3: a) Illustration of the battery stack composed of lithium metal, separator and graphite with the approximate size of the focused beam and b) WAXS contour plots of the graphite (1.7-1.9 $Å^{-1}$) and c) plating (2.5-2.6 $Å^{-1}$) regions. d) Voltage of profile during lithiation at C/5, the cell was overcharged to 150 % (corresponding to 7.5 h) of its capacity to intentionally trigger plating. e) spatial map of lithium peak area over the region of interest from fitting WAXS patterns in each pixel during lithiation.

This challenge was one of the main questions to address in the experiment carried out in **Paper II**, to be able to detect plated lithium even in the bulk of graphite, and to do that, *operando* scanning SWAXS was employed. The experiment, carried out at the ForMAX beamline (MAXIV, Lund), used the same graphite electrode as in **Paper I**. A focused beam of 48x12 μm^2 was used to scan the electrode, and the scanning area was made of 3 lines with 31 points each, with a step size of 48 by 12 μm horizontally and vertically (**Figure 5.3a**). The total scanning area was cropped to a region of interest (ROI) to avoid the contribution of the separator and copper current collector, as well as limit the partially crystalline signal of PEEK in the WAXS pattern, which reduced the scanning area to 2 lines. Scanning SWAXS enabled to spatially and temporally resolve the evolution of the lithiation state of graphite (**Figure 5.3b**), which will be further discussed in section 5.2 on lithium plating.

Li plating can be identified by a diffraction peak (110 peak) around 2.5 $Å^{-1}$ appearing in the WAXS pattern (**Figure 5.3c**). The lithium peak was fitted using a pseudo-Voigt profile, and the area of the peak for each pixel was converted to a colour scale and plotted as an image that represents the spatial distribution of plated lithium (**Figure 5.3e**). The electrode thickness was approximately 50 μm, and the ROI covers the first 12 to 36 μm below the separator, so plating is indeed located in the bulk of graphite. Plated lithium seems to start from the edges of the electrode and propagate toward the centre. At the end of the lithiation, the signal of plated lithium can be detected in the whole electrode, but with more intensity towards the edges. XTM was also performed in **Paper II** (see supporting information), providing visual confirmation of plating in bulk graphite. The difference in term of plating location between **Paper I** and **Paper II** (surface or bulk, respectively) can be explained by the use of different cell design: the pressure applied in the cell's stack in **Paper II** was more important with the additional spring, providing shorter electrode distant and reduced internal resistances, which can prevent lithium growth at the interface of the separator. Another difference is that the cell in **Paper II** had an extra polypropylene separator placed between the glass fibre separator and graphite. Polypropylene-based separators are known to have sub-micrometre pore size [155], whereas the distance between glass fibres is around tens of micrometres. The small pore size of the polypropylene separator could help to contain plated lithium in the bulk electrode and limit its growth inside the separator.

Scanning SWAXS was also used to detect Na-metal plating in a hard carbon electrode in **Paper III** (**Figure 5.4a**). In this experiment, a capillary cell was used, and the electrode was scanned with a focused beam of size 25 by 15 μm horizontally and vertically. In this way, an image of the electrode can be made with contrast from the different features in SWAXS (e.g., particle surface, micropore filling, metallic cluster and intercalation). The spatial and temporal evolution of these features during the sodiation process will be further discussed in section 5.2. WAXS in particular could

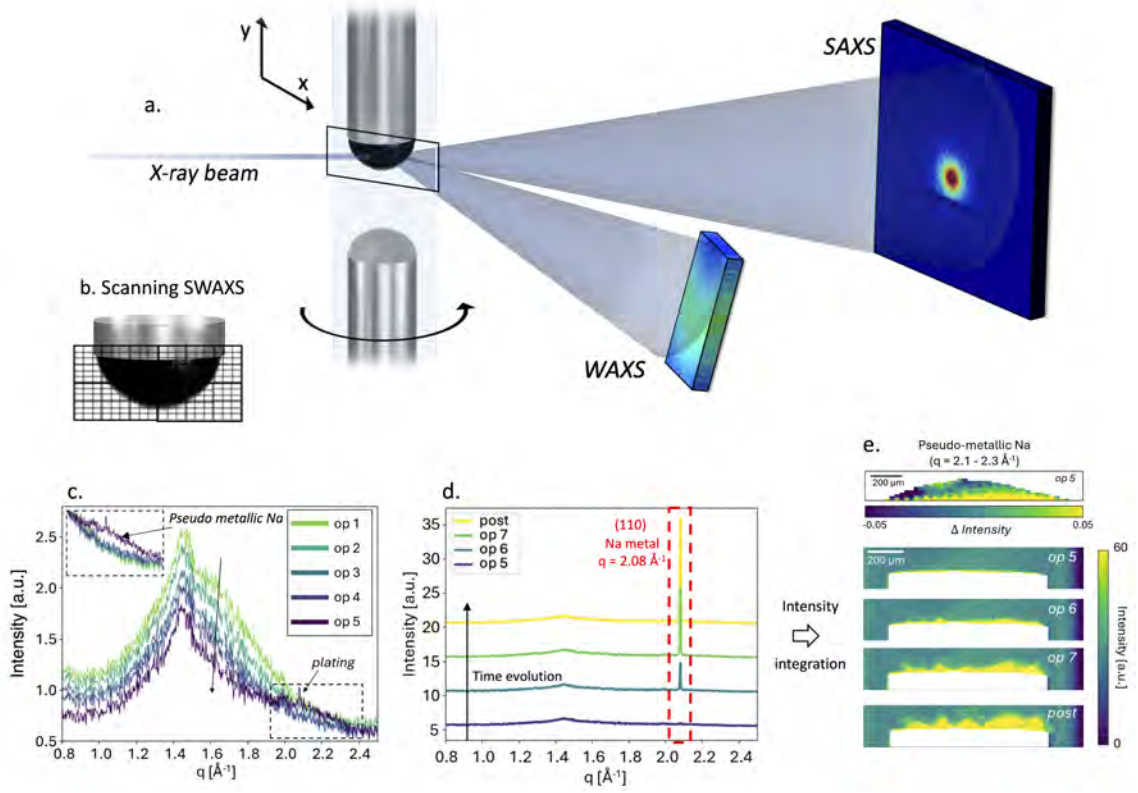

Figure 5.4: a) Schematic of scanning SWAXS set up at the cSAXS beamline (SLS, Paul Scherrer Institute). The hard carbon electrode placed in a capillary cell is illuminated by a focused X-ray beam that is scanning the sample (b), forming a map made of SWAXS patterns. c) Average WAXS curves of the electrode in the early stages of sodiation of the electrode (op 1-5) and d) during the later stage of sodiation (op 5-7, post) at the onset of plating. e) Scanning WAXS images of the intensity distribution of the peak for metallic sodium 2.08 $Å^{-1}$ and pseudo-metallic sodium intensity difference map compared to pristine electrode.

detect the (110) peak of metallic sodium and pseudo-metallic sodium clusters in the micropores of hard carbons, as shown in **Figure 5.4c,d**, which are the average patterns of all the pixels of the end of sodiation. In this study, the applied current of 14 μA corresponds to roughly 0.8C based on the segmentation and density of hard carbon and the cell was cycled for 90 minutes (190 % of the capacity), making overcharging trigger sodium plating. Spatially resolved images were created by the WAXS signal of the Na-metal peak for every pixel and are shown in **Figure 5.4e**. Here, plating of Na-metal seems to be starting from the bottom of the electrode, close to the current collector, and progresses into the hard carbon electrode.

There are notable differences in the location of metallic deposition between the lithium/graphite system and the sodium/hard-carbon system. In the lithium case, metallic lithium is detected both within the bulk of the graphite and as dendritic structures at the graphite–separator interface. In contrast, metallic sodium in the

hard-carbon system is found primarily near the current collector. Several factors could explain these differences. First, the cell configurations are fundamentally different. The capillary cell used for hard carbon applies no mechanical pressure between electrodes, which likely alters the current distribution compared with the PEEK cell used for graphite, where a spring maintained a pressure of approximately 910 kPa. Additionally, the capillary cell had no separator, which may further influence deposition behaviour. Second, preferential metallic deposition close to the current collector could indicate a low electronic conductivity in the electrode due to the dip coating method. Finally, the micro-pores of hard carbon become filled with sodium in a pseudo-metallic state, as indicated by the broad amorphous WAXS peak. This pseudo-metallic signal is particularly intense in the region close to the current collector (see **Figure 5.4d**), suggesting that pores with a high degree of pseudo-metallic sodium could serve as favourable precursors for sodium plating when the electrode is overcharged. This could reveal a fundamentally different metallic deposition mechanism between hard carbon and graphite, where the additional microporosities of hard carbon act as a buffer for metallic deposition, as suggested in another study [121].

5.1.2 Raman spectroscopy

This section highlights how Raman spectroscopy can be used to detect lithium plating through its reaction with the SEI and study the sodiation of hard carbon. This section is not part of any papers and is exclusive to the thesis. Raman spectroscopy was performed on a LabRAM HR Evolution (Horiba Jobin Yvon), which was calibrated before each measurement with a Si plate.

Raman mapping is particularly useful when performed with a confocal Raman spectrometer, which uses a microscope to precisely focus the laser to specific regions of interest with a resolution of a few micrometres. In this work, a graphite/lithium coin cell with LP57+VC electrolyte was overcharged to 150 % of its nominal capacity at 1C. The cell was then opened in an argon-filled glovebox and transferred to an air-tight Raman cell equipped with a glass window (see below). **Figure 5.5a** shows a microscope image of the selected area of the graphite electrode. The left-hand side of the image shows a golden "region" characteristic of lithiated graphite (LiC_6) [46], while metallic lithium can be seen covering the graphite grains on the right-hand side. Raman mapping was performed by scanning a 75x75 μm^2 area with a 632 nm laser, using 20 steps in both the X and Y directions (**Figure 5.5b**). Each spectrum was acquired with a 30-second exposure repeated three times to improve the signal-to-noise ratio, resulting in a total measurement time of approximately 10 hours. In “Region 1” (**Figure 5.5c**), the G band appears at 1600 cm^{-1}, confirming the presence of lithiated graphite, as pristine graphite typically shows this band closer to 1580 cm^{-1} [82]. In contrast, “Region 2” displays the characteristic Li_2C_2 band at 1853 cm^{-1}, formed through reactions between the SEI and plated

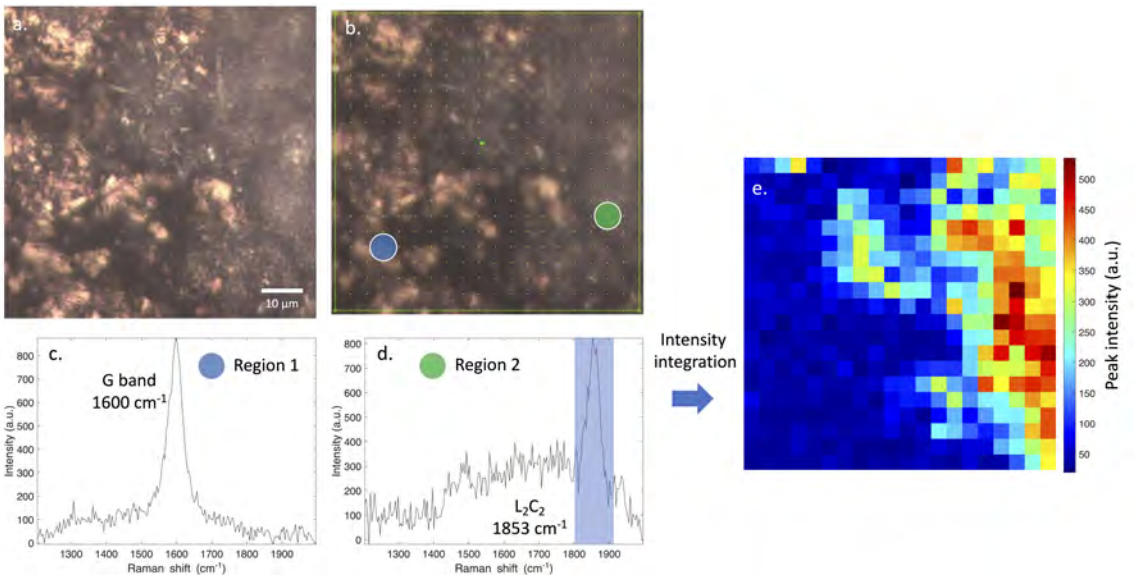

Figure 5.5: a) Microscope image of a lithiated graphite electrode that was over lithiated to 150 % of its capacity at 1C, and b) an overlap of the mapping area showing every spatial point where Raman spectra were taken. c) d) Raman spectra showing the G band and the Li_2C_2 peak in "Region 1" and "Region 2", respectively. The Li_2C_2 peak intensity was integrated and put into a colour map in e).

lithium [80, 81, 143]. Notably, the G band is absent in **Figure 5.5d**, likely because plated lithium blocks the laser from reaching the underlying graphite. The integrated Li_2C_2 band intensity for each scan is plotted in **Figure 5.5e**, producing a spatial map in which each pixel corresponds to the local band intensity. This distribution correlates well with the metallic deposits observed in the microscope image. With Raman mapping on graphite, plating is observed with the same electrolyte (LP57+VC) used in **Paper I** and correlates with XTM results (**Figure 5.1**, where heterogeneous lithium deposition is observed. The main limitation of Raman mapping is the trade-off between measurement time, scanning area, and spectra quality. Larger scanned regions provide more representative information on metallic deposition, but achieving comparable spectral quality requires substantially longer acquisition times. Another limitation comes from the fact that plated lithium is physically blocking the graphite underneath from the laser, which prevents the determination of the lithiation state.

Raman spectroscopy can also be used to follow the sodiation of hard carbon. In the *operando* cell used here, a glass window enabled optical access, and holes were made in both the sodium counter electrode and the glass-fibre separator to allow the laser to reach the hard carbon electrode (**Figure 5.6a**). During sodiation at C/20 (corresponding to a current of 70 μA), Raman spectra were acquired in a fixed position on the electrode every 10 minutes, with an effective measurement time of 3 minutes per spectrum. For each Raman spectrum, the position of the G band was determined, and its evolution is shown in **Figure 5.6c** together with the voltage

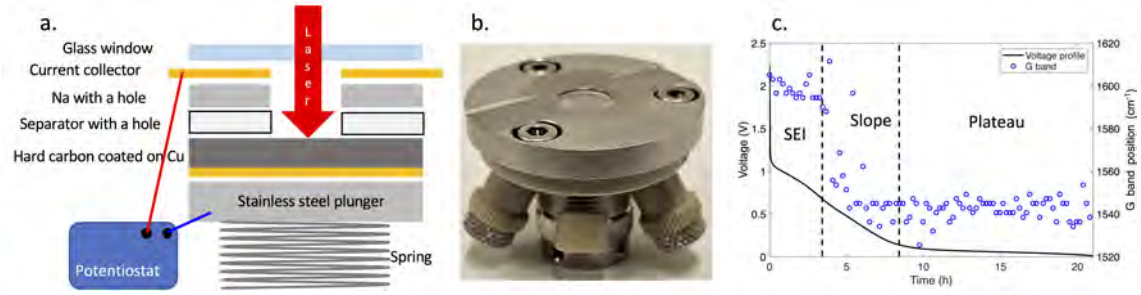

Figure 5.6: a) schematic of the *operando* cell for Raman spectroscopy with b) a picture of the actual cell. c) Voltage profile of a hard carbon/sodium cell cycled at C/20 with the evolution of the G band position.

profile of the hard carbon half-cell. Interaction of sodium ions with hard carbon can modify the C–C bonding environment and shift the G-band position, a change associated with sodium intercalation [120] or surface adsorption [92]. Since this was the first cycle, SEI formation is expected at the start of the charge, which is reflected by a small feature around 1 V early in the sodiation process. The G-band position remains constant during SEI formation, indicating that no intercalation occurs between 2 and 0.7 V—consistent with previous observations [120]. After SEI formation, the G band redshifts from 1600 cm^{-1} to approximately 1540 cm^{-1} throughout the sloping region of the voltage profile, signalling sodium intercalation between the graphene layers and surface adsorption on surfaces and defects of hard carbon. The relative contribution of these two mechanisms strongly depends on the defect concentration of the hard carbon, which is influenced by the synthesis temperature [90]. During the plateau region (below 0.1 V), the G-band position again remains constant, indicating that a different storage mechanism dominates, namely micropore filling. This mechanism is examined in more detail in the following section using scanning SWAXS.

5.2 Scanning SWAXS to detect heterogeneities in ion storage in carbon materials

In **Paper III**, the SWAXS signal of hard carbon that provides information about its microstructure was used to study the sodiaiton process. The low-q region (q = 0.0045–0.007 $Å^{-1}$) reflects the particle surface, and changes in this region, such as those caused by SEI formation, are expected to increase the scattering intensity. **Figure 5.7b** shows an average SAXS curve of all the scans with an increase in the surface-related signal, which was fitted using a power law. The evolution of this contribution is presented in **Figure 5.7d**. The increase is most pronounced at the beginning of sodiation, consistent with initial SEI formation, but it continues to grow throughout sodiation, indicating ongoing surface reactions, likely due to SEI evolution. The mid-q region (q = 0.12–0.4 $Å^{-1}$) corresponds to scattering from

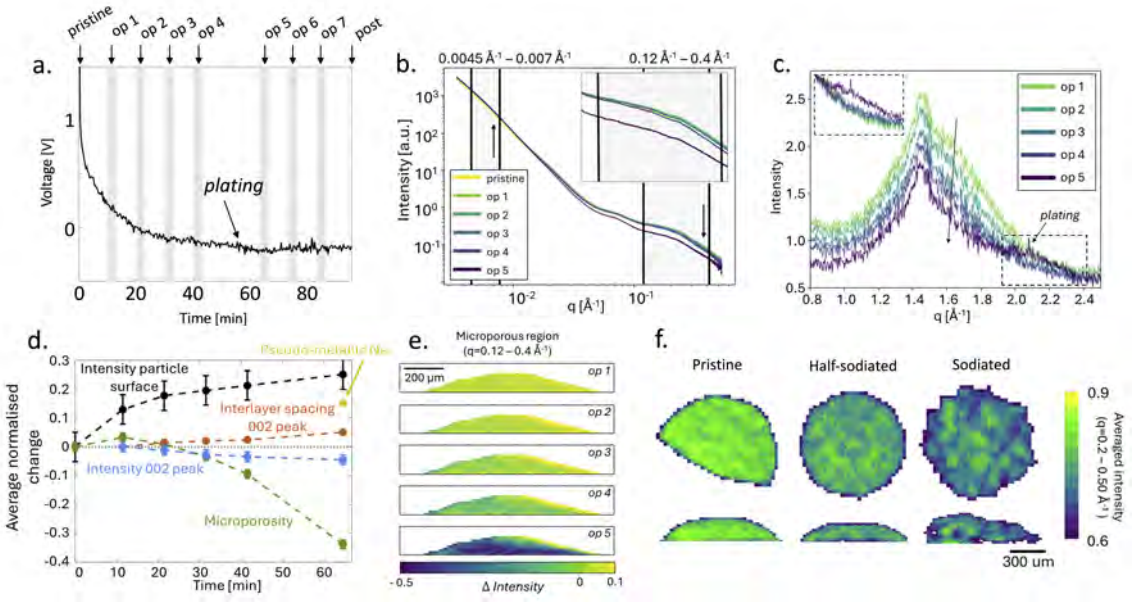

Figure 5.7: a) Voltage profile of the hard carbon/sodium cell with grey lines indicates when scanning SWAXS measurements were performed, and the inflexion point characteristic of plating is pointed out. b) SAXS curves of the averaged intensity over the full projected area of the electrode for the first five *operando* scans. The inset shows a magnified view of the q-range corresponding to scattering from micropores. c) WAXS curves of the averaged intensity over the full projected area of the electrode for the first five *operando* scans. d) Overlay of the line plots of the average intensity in selected q-regions corresponding to the different mechanisms of sodiation during the electrochemical process. e).Difference maps of the averaged intensity in the microporous region. f) 2D slices extracted horizontally and vertically from the tomograms of the averaged intensity in the microporous region

the micropores of hard carbon. The shoulder feature in this region arises from the electron density contrast between the empty micropores and their surrounding carbon matrix. As sodiation proceeds, the electron density of the micropores increases due to pore filling, reducing this contrast and causing a decrease in the scattering intensity. Initially, the scattering intensity of the micropore region increases (**Figure 5.7d**), which can be associated with sodium intercalation since it increases the electron density of the carbon matrix around the micropores [90]. Thereafter, the intensity decreases, with the strongest decrease observed during the low-voltage plateau (op 3-5), consistent with extensive micropore filling. Two-dimensional maps were generated by integrating the scattering intensity of the micropore region for each pixel in the scanning SAXS dataset and normalising to the pristine electrode (**Figure 5.7e**). One can note that during op 3–5, the relative intensity does not decrease uniformly across the electrode but shows larger decreases near the current collector, indicating a higher degree of pore filling in this region.

The 002 peak in WAXS (**Figure 5.7c**) is analogous to the graphite (002) diffraction

peak but significantly broader due to the more disordered nature of hard carbon. This peak (q = 1.2–1.9 $Å^{-1}$) was fitted with a Gaussian profile, and its position was used to determine the interlayer spacing of the turbostratic graphene layers ($d_{002} = 2\pi/q_{002}$). The interlayer spacing increases continuously during sodiation (**Figure 5.7d**), indicating that intercalation is not only limited to the sloping part of the voltage curve but can also occur during the plateau. At first, this appears to contradict the Raman results, which show no intercalation signature during the plateau (**Figure 5.6**). However, this discrepancy can be explained by the fact that shifts in the Raman G band are more strongly influenced by defect-related surface adsorption than by interlayer intercalation, as suggested in [92].

To obtain spatially resolved insight into heterogeneities in hard-carbon sodiation, SAXS tomography was performed on ex situ samples. Three electrodes were analysed: pristine, partially sodiated, and highly sodiated. In SAXS tomography, the sample is rotated from 0 to 180 °, and a SAXS pattern is collected at each angle. Reconstruction using the algorithm developed by Liebi *et al.* [156] produces a three-dimensional volume in which each voxel contains a full scattering pattern, allowing spatially resolved analysis beyond the line-averaged information obtained in scanning mode. The main limitation of SAXS tomography is the long acquisition time, on the order of several hours in this study, compared to the 10-minute acquisition of scanning SWAXS, making it unsuitable for *operando* measurements. **Figure 5.7f** displays cross-sections extracted from the reconstructed 3D volumes, where the colour scale represents the average scattering intensity of the micropore region (q = 0.12–0.4 $Å^{-1}$). For both the partially and fully sodiated samples, the scattering intensity decreases relative to the pristine electrode, confirming micropore filling. Importantly, the decrease is not spatially uniform: different regions show varying degrees of pore filling, indicating that sodiation induces increasing heterogeneity within the electrode as the degree of sodiation increases.

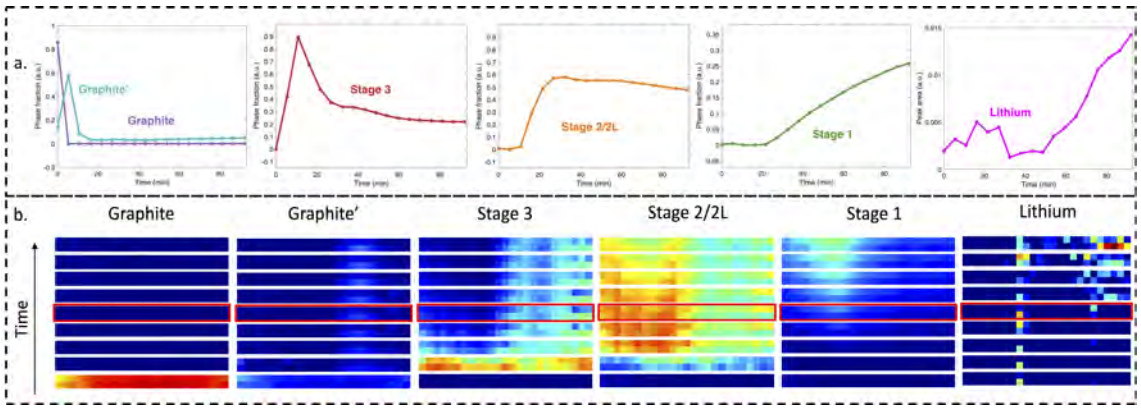

Figure 5.8: a) Average phase fraction of the electrode. b) Spatial and temporal images of the different graphite phases and lithium peak area evolution during lithiation at 1C. Red boxes indicates roughly the onset of lithium plating.

Scanning WAXS was also employed to monitor the lithiation of graphite in **Paper I**. The diffraction peaks of the different graphite stages were fitted using a pseudo-Voigt profile, and the phase fractions were calculated under the assumption that $\sum f_i = 1$, where f_i denotes the fraction of each graphite phase (stage 1, 2/2L, 3, graphite', and graphite). As shown in **Figure 5.8a**, the electrode initially contains a mixture of graphite and graphite' (stage 4 or stage 1L graphite), likely due to incomplete conversion of graphite during SEI formation cycles prior to the experiment. Graphite then goes through the different phases when lithiated, in order of transformation, stage 3 (LiC_30), stage 2/2L (LiC_{12-18}) and finally stage 1 (LiC_6). At the end of lithiation, the electrode consists of approximately 50 % stage 2/2L, 25 % stage 3, and 25 % stage 1, indicating incomplete lithiation despite the 150 % overcharge. This heterogeneity becomes more evident in the spatially resolved images of **Figure 5.8b**. In the images, the colour scale reflects the phase fraction of the various graphite phases and the integrated area of the lithium (110) peak. The graphite and graphite' regions convert relatively uniformly into stage 3 and stage 2/2L early in the process. However, the left-hand side of the electrode continues to lithiate and eventually forms stage 1, while the right-hand side remains at intermediate stages and never reaches stage 1. This asymmetric behaviour correlates with lithium plating on the right-hand side of the electrode, as evidenced by the increasing area of the metallic lithium peak. The presence of plated lithium slows down the lithiation kinetics, meaning that portions of the electrode affected by plating lithiate more slowly than those that lithiate normally. Scanning WAXS experiments can further reveal how current density influences lithium plating. At C/5, which represents a moderate current density, overcharging produces relatively homogeneous plating across the electrode (**Figure 5.3e**). By contrast, at 1C (considered as high current density, **Figure 5.8b**), plating becomes highly localised to one side of the electrode, significantly hindering the lithiation process in that region.

The results highlighted from **Paper II** & **III** with *operando* scanning SWAXS, provide powerful examples of resolving heterogeneities within battery electrodes. Such spatially and temporally resolved measurements reveal that lithiation and sodiation reactions progress unevenly, driven by gradients in ionic and electronic conductivity, or local changes in interfacial properties, such as lithium plating. As a result, different regions of the electrode may experience delayed intercalation, enhanced pore filling, or preferential metal deposition. These heterogeneities can lead to uneven utilisation of active material, amplify mechanical stresses within the electrode, build internal resistances and promote localised side reactions, which, all combined, reduce performance and accelerate ageing.

5.3 Getting quantitative information from tomographic images

X-ray tomography produces reconstructed greyscale images that reflect the electron density of the materials in the sample, which, often, by itself, is limited to a qualitative analysis of tomography data. This section aims to give more details about the methodology for extracting qualitative data from an XTM measurement.

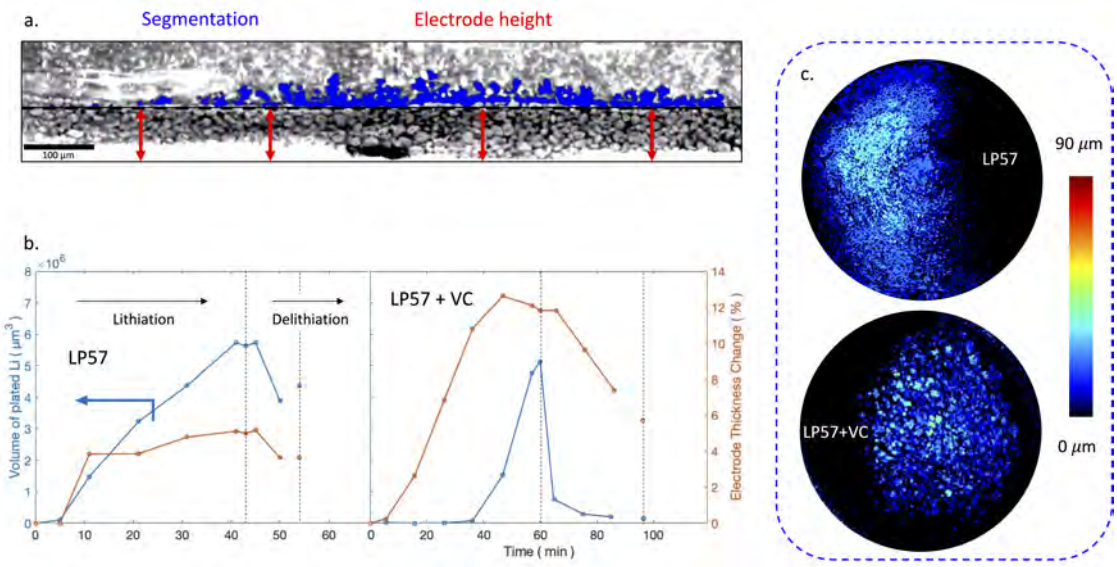

Figure 5.9: a) Tomographic cross-sectional slice showing different examples of quantitative data extraction. b) Volume of plated lithium and electrode thickness change over time during lithiation at 1C for the baseline electrolyte (LP57) and the addition of VC. c) Electrode height maps for LP57 and LP57+VD electrolytes.

In **Paper I**, lithium plating on a graphite electrode was analysed in different ways. Since there is a good contrast between the separator and lithium deposition, it was possible to do a simple threshold segmentation to quantify the amount of lithium (**Figure 5.9a**). The porosities between graphite particles that have the same greyscale intensity as lithium were removed by cropping the image. The graphite expansion due to lithiation was quantified by measuring the electrode's height at different points and for multiple slices to get an estimation of the average thickness change of the electrode during lithiation and delithiation. The amount of plated lithium and the evolution of the electrode thickness change are shown in **Figure 5.9b** for the baseline electrolyte LP57 and with the VC additive. With LP57, the onset of lithium plating occurs in the first 5 minutes of lithiation at 1C, whereas the addition of VC seems to delay the start of the deposition. It is also possible to observe the stripping of lithium during delithiation and notice that with the baseline electrolyte, there is some lithium still present at the end of delithiation, indicating the presence of dead lithium, i.e., lithium that is disconnected from the

electrode and does not participate in any electrochemical reactions. Conversely, with LP57+VC, the amount of dead lithium is significantly lower. The electrode thickness change is an indication of the state of charge of graphite, as it has been shown that graphite undergoes a change in volume of 13 % when fully lithiated [40]. In the case of the baseline electrolyte, the electrode thickness does not reach these values and plateaus at around 5 %, indicating incomplete lithiation. This goes accordingly with **Paper II**, which used the same graphite and electrolyte (LP57) and showed the incomplete lithiation state of graphite, though with more precision on the lithiation stages with scanning WAXS. With the addition of VC in the electrolyte, the electrode thickness increased up to 12-13 %, which can be related to the delayed plating with graphite being able to reach a higher degree of lithiation. However, this process does not seem to be reversible since for both electrolyte systems, the relative thickness change does not come back to zero. Measuring the electrode thickness in the manner used in this thesis can become unreliable when lithium plating occurs within the bulk of the electrode. In such cases, it is not possible to distinguish whether the overall thickness increase arises from graphite expansion due to intercalation or from the accumulation of plated lithium. The morphology of deposition was further analysed in the height maps (**Figure 5.9c**), which are a 2-dimensional projection of the height of the lithium deposition; the graphite electrode surface is represented in black in the colour scale. With LP57, plating deposition is thin and rather homogenous, whereas with LP57+VC, lithium deposition is island-like and growing taller.

In **Paper IV**, a sulfur/lithium cell was cycled, and X-ray tomographic measurements were acquired during the conversion process, and the voltage profile is shown in **Figure 5.10a**. Initially, the electrode is composed of elemental sulfur, identified as bright, granular particles, embedded in a carbon and binder matrix (**Figure 5.10b**). During the high voltage plateau (around 2.4 V), the elemental sulfur conversion to soluble polysulfides takes place (equation 2.12). Since polysulfides are in solution, it is not possible to visualise them with XTM and at the discharge, no elemental sulfur is visible (**Figure 5.10c**), only the carbon matrix remains. At the end of the charge (**Figure 5.10d**), it is possible to observe the redeposition of elemental sulfur particles, although they are not distributed evenly in the electrode, a phenomenon that has also been previously reported in literature [115]. Additionally, it seems from the tomographic image that not all the sulfur was converted back during the charge, which could explain the poor coulombic efficiency of the first cycle (78 %).

Analysing and segmenting sulfur particles in this dataset is particularly challenging compared to the identification of lithium plating in **Paper I** because the sulfur particles have a similar greyscale intensity to the fibres of the glass fibre separator. **Figure 5.10e** illustrates this by giving an example of a slice where sulfur particles and fibres coexist; even for the naked eye, it is difficult to distinguish the sulfur particles. **Figure 5.10f** shows that threshold segmentation fails to separate sulfur

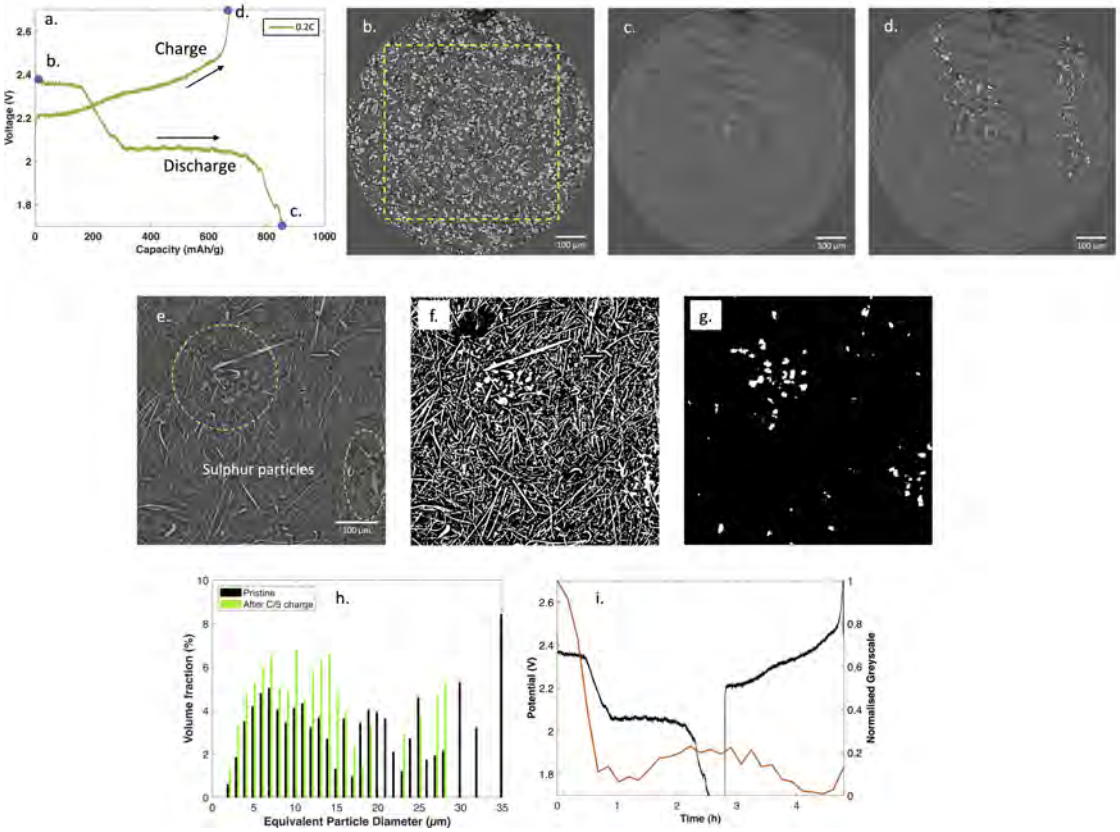

Figure 5.10: a) Voltage profile of a sulfur/lithium cell (discharge and charge) at 0.2C. b) pristine, c) end of discharge and d) end of charge tomographic slices extracted from reconstructed volumes. The yellow square indicated the size of the region of interest used for further analysis. e) tomographic slice showing sulfur particles (highlighted by yellow circles) and fibres from the separator, and f) binary image showing threshold segmentation. g) Neural network segmentation was able to isolate sulfur and remove fibres. h) Particle size distribution of the pristine and redeposited sulfur at the end of the charge. i) Voltage profile and normalised greyscale intensity as a function of time.

particles and fibres, causing an over-segmentation. Instead, a neural network was trained on challenging slices, and the sulfur particles were manually labelled. This produced a much more realistic segmentation (**Figure 5.10g**) where the fibres are successfully removed from the image, and the sulfur particles can be segmented. The careful viewer will notice that the fibres with the higher greyscale intensity are also picked up by the neural network segmentation. Since this error is consistent throughout all the slices, it is possible to evaluate the segmentation error from a slice known to contain no sulfur, such as one at the end of discharge.

From the binary image, a connected component algorithm (`bwconncomp`, MATLAB function) was applied to separate and label individual sulfur particles from the pristine and end-of-charge scans. Each particle was associated with a sphere of the same volume, and particles were binned with a step of 1 μm of the equivalent

diameter of the sphere to calculate the particle size distribution (**Figure 5.10h**). Particles with an equivalent diameter smaller than the image resolution of 1.5 μm or bigger than the sieve size of 45 μm (the sulfur particles were sieved before electrode coating) were removed from the distribution. Using the volume fraction to represent the size distribution reflects better the particle contribution to the capacity, where small particles might be over-represented in number but account for a small fraction of the total volume and hence capacity. The size distribution is rather broad in the pristine scan, from 2 to 30 μm. At the end of the charge at 0.2C, the average particle size is smaller, going down from 17 μm in the pristine electrode to 13 μm after charge.

The low voltage plateau at 2.1 V (**Figure 5.10a**) is characteristic of the conversion of polysulfides to solid compounds (Li_2S_2 and Li_2S). Li_2S should give rise to a brighter phase at the end of charge. This is, however, not observed (**Figure 5.10c**), and could be due to the fact that solid particles precipitate below the image resolution, making them not directly visible in the image. To resolve the solid end-product of sulfur conversion, the mean greyscale intensity of the average of 30 slices of the electrode was calculated and scaled by the average intensity of 125 lithium slices through the lithium counter electrode. The lithium greyscale intensity is not expected to change through the charge and can thus be used for normalisation. **Figure 5.10i** shows this normalised greyscale together with the voltage profile against time. The normalised greyscale undergoes a sharp decrease during the high voltage plateau, which corresponds to the dissolution of elemental sulfur particles. During the low voltage plateau, the intensity increases again and reaches a maximum at the end of discharge, which could indicate that Li_2S_2 and Li_2S are indeed being formed, and the nucleation of these species starts halfway through the discharge. Individual Li_2S particles are not resolved with XTM directly, which suggests that their size is below the image resolution of 1 μm. Additionally, this uniform deposition can lead to the formation of a layer of Li_2S known for being an insulator [157], which could limit the electron transfer of the polysulfide conversion reaction and explain the poor capacity at the end of the discharge. During the following charge, the normalised greyscale decreases, indicating the dissolution of Li_2S, which can also be suggested by a voltage plateau above 2.2 V.

Chapter 6

Conclusions and Outlooks

In this thesis, X-ray imaging techniques have been used to track morphological changes in battery electrodes through *operando* measurement, with high temporal and/or spatial resolution. The complex chemistry and large variety of battery systems require advanced characterisation methods to reach the deepest understanding possible of the processes and degradation mechanisms. The results show that fast data acquisition in synchrotron-based X-ray techniques enabled to track the different processes taking place in a graphite electrode, from the classic intercalation of lithium ions to the normally unwanted metallic deposition. *Operando* scanning SWAXS provided spatial and temporal resolution of the electrode, indicating that plated lithium influences the intercalation by slowing down the reaction kinetics. Scanning SWAXS also allowed to follow changes in micropores and interlayer spacing of a hard carbon electrode as an indicator of the sodiation state, with the correlation of electrochemical data. We show that the pore-filling mechanism responsible for the energy storage is not spatially homogeneous in the electrode, and the degree of inhomogeneities increases with the state of charge. XTM enabled the direct observation of a sulfur composite electrode, giving detailed insights into the dissolution and precipitation of elemental sulfur. Through the analysis of the size distribution of sulfur particles, we showed a decreased overall particle diameter compared to the uncycled electrode after the charge. The complete dissolution of elemental sulfur even at high current densities indicates that the conversion reaction into long-chain polysulfides is not rate-limited.

Placing the different projects of this thesis into a broader perspective highlights the critical importance of cell design in *operando* X-ray measurements. The selection of materials used for the cell assembly must be carefully considered, as they directly influence the background in SWAXS measurements and can limit the sensitivity to subtle structural changes. More importantly, the results presented here demonstrate that the mechanical pressure within the cell plays a decisive role in the degradation mechanisms that develop during cycling. The absence or uncontrolled pressure allows other electrode properties, such as electronic conductivity or parti-

cle morphology, to lead to non-uniform sodiation and lithiation, as well as the onset of metal ion plating. These findings show that cell design is not a practical constraint for *operando* measurements but an active factor shaping the electrochemical behaviour and degradation of the electrode.

With the knowledge gained throughout the different projects presented in this thesis, several promising directions emerge for future research. First, bridging WAXS and XTM on the intercalation state of graphite could be achieved through digital volume correlation, which tracks displacement fields within the electrode and may provide improved insight into local volume expansion, potentially at the scale of individual graphite particles. The constant improvements of synchrotron facilities, particularly in brilliance and acquisition speed, could further enable the capture of nucleation processes with higher temporal resolution, whether related to metal plating or the precipitation and dissolution of sulfur species. Improvements in spatial resolution, such as those provided by X-ray nano-tomography, will open the possibility to resolve processes below the micrometre length scale. For example, nano-tomography could be employed to investigate Li_2S nucleation in Li–S batteries or to elucidate how sodium plating develops within hard carbon particles in relation to microporosities. Illuminating a small area of the electrode with the high brilliance of the synchrotron sources would inherently increase the radiation dose received by the materials, so any beam-induced damage would need to be addressed to avoid lowering data quality. Additionally, neutron imaging techniques could be considered to detect metallic deposition since neutrons provide a better contrast between Li/Na with carbon materials and low attenuation with other cell components. However, neutron techniques usually have a lower flux than X-ray techniques, which limits temporal and spatial resolution. The new European Spallation Source in Sweden could help the development of neutron images.

Acknowledgments

I started my PhD studies back in November 2021, and what a ride it was! During this journey, I have met a lot of amazing people who contributed to this work in many different ways, and I would like to thank them.

First and foremost, I would like to thank my supervisor, Aleksandar Matic. I think you are both an amazing scientist and manager, and I am grateful for all the help and support you have provided. You allowed me to carry out my projects with a great degree of freedom and to explore the world through memorable research trips, which helped me grow both as a researcher and as a person. I want like to thank my former assistant supervisor, Shizhao Xiong, who enlightened me with his guidance and constant enthusiasm during the first half of my studies. To my examiner, Patrik Johansson, thank you for all the help throughout my PhD.

To all the current, former members and visitors of the Material Physics division, you all have my warmest thanks! You are the reason that we have such a great environment to do research and have a lot of fun in afterworks! I will truly miss working with all of you. Special thanks to my former colleagues Nataliia Mozhzhukhina and Matthew Sadd, who were my guardian angels in my earlier times as a PhD student, and introduced me to the fantastic world of research. To Jan Jamroz and Aleksi Zitting, thank you for all the help along the way with your immense knowledge of scattering techniques. I would like to say a special thank you to all my climbing buddies at Chalmers and elsewhere, Marita, Isak D, Isak B, Audunn, Romaric and Riccardo. Thank you to Ezio Zanghellini for making research in the lab possible and for all the help and advice.

I would like to thank the Swedish Energy Agency for funding my projects (grant 2019-90076). I am thankful to ESRF and MAXIV and their respective beamline staff (at ID19, ID15a, ForMax, DanMax) for providing the beamtime and great help.

I want to give my warmest thanks to my friends in Göteborg for all the amazing time I had in Sweden, all the trips in Scandinavia we made, and all the fun we had together! I hope this will continue! To all my friends back in France, thank you all for the continuous support and the good moments we had together, even though you are far away. I wish I could see you more often! Magdalena, thank you for your support, I feel so lucky to have you in my life! Mes derniers remerciements vont à ma famille, Laurence, Laurent, Yohan et Pauline. Merci du fond du cœur pour votre soutien inconditionnel.

Antoine Klein, Göteborg, 2026

Bibliography

[1] M. R. Palacín, "Recent advances in rechargeable battery materials: a chemist's perspective," Chemical Society Reviews, vol. 38, pp. 2565–2575, Aug. 2009.

[2] M. Armand and J. M. Tarascon, "Building better batteries," Nature, vol. 451, pp. 652–657, Feb. 2008.

[3] "https://www.consilium.europa.eu/en/policies/fit-for-55/, Accessed: 06/01/2026," Mar. 2025.

[4] A. Yoshino, "The Birth of the Lithium-Ion Battery," Angewandte Chemie International Edition, vol. 51, no. 24, pp. 5798–5800, 2012.

[5] M. S. Ziegler and J. E. Trancik, "Re-examining rates of lithium-ion battery technology improvement and cost decline," Energy & Environmental Science, vol. 14, no. 4, pp. 1635–1651, 2021.

[6] H. Zhang, Y. Yang, D. Ren, L. Wang, and X. He, "Graphite as anode materials: Fundamental mechanism, recent progress and advances," Energy Storage Materials, vol. 36, pp. 147–170, Apr. 2021.

[7] H. Lin, Y. Hu, Y. Zhou, W. Hu, J. Lin, H. Luo, Y. Jin, D. Zhao, J. Chen, M. Tao, P. Shan, J. Liang, Y. Wei, and Y. Yang, "Unveiling the Onset, Evolution, and Kinetic Factors Associated with Lithium Plating on Graphite Electrodes in Lithium-ion Batteries," Advanced Energy Materials, vol. 15, p. e02728, Oct. 2025.

[8] T. Foroozan, S. Sharifi-Asl, and R. Shahbazian-Yassar, "Mechanistic understanding of Li dendrites growth by in- situ/operando imaging techniques," Journal of Power Sources, vol. 461, p. 228135, June 2020.

[9] M. D. Slater, D. Kim, E. Lee, and C. S. Johnson, "Sodium-Ion Batteries," Advanced Functional Materials, vol. 23, no. 8, pp. 947–958, 2013.

[10] O. Lenchuk, P. Adelhelm, and D. Mollenhauer, "New insights into the origin of unstable sodium graphite intercalation compounds," Physical Chemistry Chemical Physics, vol. 21, no. 35, pp. 19378–19390, 2019.

[11] L. F. Nazar, M. Cuisinier, and Q. Pang, "Lithium-sulfur batteries," MRS Bulletin, vol. 39, pp. 436–442, May 2014.

[12] X. Ji and L. F. Nazar, "Advances in Li–S batteries," Journal of Materials Chemistry, vol. 20, pp. 9821–9826, Nov. 2010.

[13] D. Atkins, E. Capria, K. Edström, T. Famprikis, A. Grimaud, Q. Jacquet, M. Johnson, A. Matic, P. Norby, H. Reichert, J. Rueff, C. Villevieille, M. Wagemaker, and S. Lyonnard, "Accelerating Battery Characterization Using Neutron and Synchrotron Techniques: Toward a Multi-Modal and Multi-Scale Standardized Experimental Workflow," Advanced Energy Materials, vol. 12, p. 2102694, May 2022.

[14] D. Linden and T. B. Reddy, eds., Handbook of batteries. McGraw-Hill handbooks, McGraw-Hill, 3. ed ed., 2002.

[15] Q. Zhao, S. Stalin, C. Z. Zhao, and L. A. Archer, "Designing solid-state electrolytes for safe, energy-dense batteries," Nature Reviews Materials, vol. 5, no. 3, pp. 229–252, 2020.

[16] M. S. Whittingham, "Electrical Energy Storage and Intercalation Chemistry," Science, vol. 192, 1976.

[17] K. Mizushima, P. C. Jones, P. J. Wiseman, and J. B. Goodenough, "LixCoO2 (0<x<1): A new cathode material for batteries of high energy density," Materials Research Bulletin, vol. 15, pp. 783–789, June 1980.

[18] R. Yazami and P. Touzain, "A reversible graphite-lithium negative electrode for electrochemical generators," Journal of Power Sources, vol. 9, no. 3, pp. 365–371, 1983.

[19] J. Xu, X. Cai, S. Cai, Y. Shao, C. Hu, S. Lu, and S. Ding, "High-Energy Lithium-Ion Batteries: Recent Progress and a Promising Future in Applications," ENERGY & ENVIRONMENTAL MATERIALS, vol. 6, no. 5, p. e12450, 2023.

[20] R. Borah, F. Hughson, J. Johnston, and T. Nann, "On battery materials and methods," Materials Today Advances, vol. 6, p. 100046, June 2020.

[21] F. Ozanam and M. Rosso, "Silicon as anode material for Li-ion batteries," Materials Science and Engineering: B, vol. 213, pp. 2–11, Nov. 2016.

[22] S. Zhang, "Chemomechanical modeling of lithiation-induced failure in high-volume-change electrode materials for lithium ion batteries," npj Computational Materials, vol. 3, p. 7, Feb. 2017.

[23] Q. Xiao, M. Gu, H. Yang, B. Li, C. Zhang, Y. Liu, F. Liu, F. Dai, L. Yang, Z. Liu, X. Xiao, G. Liu, P. Zhao, S. Zhang, C. Wang, Y. Lu, and M. Cai, "Inward lithium-ion breathing of hierarchically porous silicon anodes," Nature Communications, vol. 6, p. 8844, Nov. 2015.

[24] M. Xia, B. Chen, F. Gu, L. Zu, M. Xu, Y. Feng, Z. Wang, H. Zhang, C. Zhang, and J. Yang, "Ti_3 C_2 T_x MXene Nanosheets as a Robust and Conductive Tight on Si Anodes Significantly Enhance Electrochemical Lithium Storage Performance," ACS Nano, vol. 14, pp. 5111–5120, Apr. 2020.

[25] M. K. Mahek, M. Ramadan, D. S. Choi, M. Ghazal, M. Alkhedher, and A. H. Alami, "Lithium titanate batteries for sustainable energy storage: A comprehensive review of safety, performance, and environmental impact," Journal of Energy Storage, vol. 132, p. 117573, Oct. 2025.

[26] A. Manthiram, "A reflection on lithium-ion battery cathode chemistry," Nature Communications, vol. 11, p. 1550, Mar. 2020.

[27] C. Banza Lubaba Nkulu, L. Casas, V. Haufroid, T. De Putter, N. D. Saenen, T. Kayembe-Kitenge, P. Musa Obadia, D. Kyanika Wa Mukoma, J. M. Lunda Ilunga, T. S. Nawrot, O. Luboya Numbi, E. Smolders, and B. Nemery, "Sustainability of artisanal mining of cobalt in DR Congo," Nature Sustainability, vol. 1, pp. 495–504, Sept. 2018.

[28] M. Kotal, S. Jakhar, S. Roy, and H. K. Sharma, "Cathode materials for rechargeable lithium batteries: Recent progress and future prospects," Journal of Energy Storage, vol. 47, p. 103534, Mar. 2022.

[29] M. R. Palacín and A. de Guibert, "Why do batteries fail?," Science, vol. 351, p. 1253292, Feb. 2016.

[30] K. Liu, Z. Wang, L. Shi, S. Jungsuttiwong, and S. Yuan, "Ionic liquids for high performance lithium metal batteries," Journal of Energy Chemistry, vol. 59, pp. 320–333, Aug. 2021.

[31] E. Peled, "The Electrochemical Behavior of Alkali and Alkaline Earth Metals in Nonaqueous Battery Systems—The Solid Electrolyte Interphase Model," Journal of The Electrochemical Society, vol. 126, pp. 2047–2051, Dec. 1979.

[32] H. Wu, H. Jia, C. Wang, J.-G. Zhang, and W. Xu, "Recent Progress in Understanding Solid Electrolyte Interphase on Lithium Metal Anodes," Advanced Energy Materials, vol. 11, no. 5, p. 2003092, 2021.

[33] E. Peled and S. Menkin, "Review—SEI: Past, Present and Future," Journal of The Electrochemical Society, vol. 164, pp. A1703–A1719, June 2017.

[34] S. K. Heiskanen, J. Kim, and B. L. Lucht, "Generation and Evolution of the Solid Electrolyte Interphase of Lithium-Ion Batteries," Joule, vol. 3, pp. 2322–2333, Oct. 2019.

[35] S. Saxena, C. Le Floch, J. MacDonald, and S. Moura, "Quantifying EV battery end-of-life through analysis of travel needs with vehicle powertrain models," Journal of Power Sources, vol. 282, pp. 265–276, May 2015.

[36] D. D. L. Chung, "Review Graphite," Journal of Materials Science, vol. 37, pp. 1475–1489, Apr. 2002.

[37] M. Winter, J. O. Besenhard, M. E. Spahr, and P. Novák, "Insertion Electrode Materials for Rechargeable Lithium Batteries," Advanced Materials, vol. 10, no. 10, pp. 725–763, 1998.

[38] K. Momma and F. Izumi, "*VESTA 3* for three-dimensional visualization of crystal, volumetric and morphology data," Journal of Applied Crystallography, vol. 44, pp. 1272–1276, Dec. 2011.

[39] J. Asenbauer, T. Eisenmann, M. Kuenzel, A. Kazzazi, Z. Chen, and D. Bresser, "The success story of graphite as a lithium-ion anode material – fundamentals, remaining challenges, and recent developments including silicon (oxide) composites," Sustainable Energy & Fuels, vol. 4, pp. 5387–5416, Oct. 2020.

[40] S. Schweidler, L. De Biasi, A. Schiele, P. Hartmann, T. Brezesinski, and J. Janek, "Volume Changes of Graphite Anodes Revisited: A Combined Operando X-ray Diffraction and in Situ Pressure Analysis Study," Journal of Physical Chemistry C, vol. 122, pp. 8829–8835, Apr. 2018.

[41] A. S. Ho, D. Y. Parkinson, D. P. Finegan, S. E. Trask, A. N. Jansen, W. Tong, and N. P. Balsara, "3D Detection of Lithiation and Lithium Plating in Graphite Anodes during Fast Charging," ACS Nano, vol. 15, pp. 10480–10487, June 2021.

[42] M. N. Obrovac and V. L. Chevrier, "Alloy negative electrodes for Li-ion batteries," Chemical Reviews, vol. 114, no. 23, pp. 11444–11502, 2014.

[43] C. Didier, E. P. Gilbert, J. Mata, and V. K. Peterson, "Direct In Situ Determination of the Surface Area and Structure of Deposited Metallic Lithium within Lithium Metal Batteries Using Ultra Small and Small Angle Neutron Scattering," Advanced Energy Materials, vol. 13, no. 44, p. 2301266, 2023.

[44] J. R. Dahn, "Phase diagram of Li x C 6," Physical Review B, vol. 44, pp. 9170–9177, Nov. 1991.

[45] C. Didier, W. K. Pang, Z. Guo, S. Schmid, and V. K. Peterson, "Phase Evolution and Intermittent Disorder in Electrochemically Lithiated Graphite Determined Using in Operando Neutron Diffraction," Chemistry of Materials, vol. 32, pp. 2518–2531, Mar. 2020.

[46] M. Bolsinger, C. Weisenberger, T. Waldmann, M. Kamlah, and V. Knoblauch, "Exploring the Inhomogeneous Nature of Li Intercalation and Li Plating on Graphite Anodes – an Experimental Study Combining Inert Gas High-Resolution Light Microscopy with Colorimetric and Machine Learning-Based Image Analysis," Advanced energy and sustainability research, vol. 0, p. e2500181, Sept. 2025.

[47] Y. Chen, K.-H. Chen, A. J. Sanchez, E. Kazyak, V. Goel, Y. Gorlin, J. Christensen, K. Thornton, and N. P. Dasgupta, "*Operando* video microscopy of Li plating and re-intercalation on graphite anodes during fast charging," Journal of Materials Chemistry A, vol. 9, no. 41, pp. 23522–23536, 2021.

[48] D. P. Finegan, A. Quinn, D. S. Wragg, A. M. Colclasure, X. Lu, C. Tan, T. M. Heenan, R. Jervis, D. J. Brett, S. Das, T. Gao, D. A. Cogswell, M. Z. Bazant, M. Di Michiel, S. Checchia, P. R. Shearing, and K. Smith, "Spatial dynamics of lithiation and lithium plating during high-rate operation of graphite electrodes," Energy & Environmental Science, vol. 13, pp. 2570–2584, Aug. 2020.

[49] G. Oney, F. Monaco, S. Mitra, A. Medjahed, M. Burghammer, D. Karpov, M. Mirolo, J. Drnec, I. C. Jolivet, Q. Arnoux, S. Tardif, Q. Jacquet, and S. Lyonnard, "Dead, Slow, and Overworked Graphite: Operando X-Ray Microdiffraction Mapping of Aged Electrodes," Advanced Energy Materials, p. e02032, Aug. 2025.

[50] D. Hu, L. Chen, J. Tian, Y. Su, N. Li, G. Chen, Y. Hu, Y. Dou, S. Chen, and F. Wu, "Research Progress of Lithium Plating on Graphite Anode in Lithium-Ion Batteries," Chinese Journal of Chemistry, vol. 39, no. 1, pp. 165–173, 2021.

[51] M. Petzl and M. A. Danzer, "Nondestructive detection, characterization, and quantification of lithium plating in commercial lithium-ion batteries," Journal of Power Sources, vol. 254, pp. 80–87, May 2014.

[52] Y. Ji, Y. Zhang, and C.-Y. Wang, "Li-Ion Cell Operation at Low Temperatures," Journal of The Electrochemical Society, vol. 160, p. A636, Feb. 2013.

[53] X. Lin, K. Khosravinia, X. Hu, J. Li, and W. Lu, "Lithium Plating Mechanism, Detection, and Mitigation in Lithium-Ion Batteries," Progress in Energy and Combustion Science, vol. 87, p. 100953, Nov. 2021.

[54] X. Zhao, Y. Yin, Y. Hu, and S.-Y. Choe, "Electrochemical-thermal modeling of lithium plating/stripping of Li(Ni0.6Mn0.2Co0.2)O2/Carbon lithium-ion batteries at subzero ambient temperatures," Journal of Power Sources, vol. 418, pp. 61–73, Apr. 2019.

[55] X. Xu, Y. Liu, J. Y. Hwang, O. O. Kapitanova, Z. Song, Y. K. Sun, A. Matic, and S. Xiong, "Role of Li-Ion Depletion on Electrode Surface: Underlying Mechanism for Electrodeposition Behavior of Lithium Metal Anode," Advanced Energy Materials, vol. 10, no. 44, pp. 1–10, 2020.

[56] K. N. Wood, E. Kazyak, A. F. Chadwick, K.-H. Chen, J.-G. Zhang, K. Thornton, and N. P. Dasgupta, "Dendrites and Pits: Untangling the Complex Behavior of Lithium Metal Anodes through Operando Video Microscopy," ACS Central Science, vol. 2, pp. 790–801, Nov. 2016.

[57] Y. Li, X. Feng, D. Ren, M. Ouyang, L. Lu, and X. Han, "Thermal Runaway Triggered by Plated Lithium on the Anode after Fast Charging," ACS Applied Materials & Interfaces, vol. 11, pp. 46839–46850, Dec. 2019.

[58] H. Ditler, T. Tegetmeyer-Kleine, G. Stahl, C. Rahe, and D. U. Sauer, "Lithium plating in commercial lithium-ion cells: An extensive study combining electrical methods with post-mortem analysis," Journal of Energy Storage, vol. 132, p. 117706, Oct. 2025.

[59] A. S. Ho, D. Y. Parkinson, S. E. Trask, A. N. Jansen, and N. P. Balsara, "Large Local Currents in a Lithium-Ion Battery during Rest after Fast Charging," ACS Nano, vol. 17, pp. 19180–19188, Oct. 2023.

[60] Q. Liu, C. Du, B. Shen, P. Zuo, X. Cheng, Y. Ma, G. Yin, and Y. Gao, "Understanding undesirable anode lithium plating issues in lithium-ion batteries," RSC Advances, vol. 6, pp. 88683–88700, Sept. 2016.

[61] C. R. Birkl, M. R. Roberts, E. McTurk, P. G. Bruce, and D. A. Howey, "Degradation diagnostics for lithium ion cells," Journal of Power Sources, vol. 341, pp. 373–386, Feb. 2017.

[62] C.-S. Kim, K. M. Jeong, K. Kim, and C.-W. Yi, "Effects of Capacity Ratios between Anode and Cathode on Electrochemical Properties for Lithium Polymer Batteries," Electrochimica Acta, vol. 155, pp. 431–436, Feb. 2015.

[63] J. Landesfeind, J. Hattendorff, A. Ehrl, W. A. Wall, and H. A. Gasteiger, "Tortuosity Determination of Battery Electrodes and Separators by Impedance Spectroscopy," Journal of The Electrochemical Society, vol. 163, no. 7, pp. A1373–A1387, 2016.

[64] J. B. Habedank, J. Kriegler, and M. F. Zaeh, "Enhanced Fast Charging and Reduced Lithium-Plating by Laser-Structured Anodes for Lithium-Ion Batteries," Journal of The Electrochemical Society, vol. 166, no. 16, pp. A3940–A3949, 2019.

[65] J.-P. Jones, M. C. Smart, F. C. Krause, and R. V. Bugga, "The Effect of Electrolyte Additives upon Lithium Plating during Low Temperature Charging of Graphite-LiNiCoAlO2 Lithium-Ion Three Electrode Cells," Journal of The Electrochemical Society, vol. 167, p. 020536, Jan. 2020.

[66] V. Sharova, A. Moretti, T. Diemant, A. Varzi, R. J. Behm, and S. Passerini, "Comparative study of imide-based Li salts as electrolyte additives for Li-ion batteries," Journal of Power Sources, vol. 375, pp. 43–52, Jan. 2018.

[67] X. Peng, Y. Lin, Y. Wang, Y. Li, and T. Zhao, "A lightweight localized high-concentration ether electrolyte for high-voltage Li-Ion and Li-metal batteries," Nano Energy, vol. 96, p. 107102, June 2022.

[68] J. C. Burns, R. Petibon, K. J. Nelson, N. N. Sinha, A. Kassam, B. M. Way, and J. R. Dahn, "Studies of the Effect of Varying Vinylene Carbonate (VC) Content in Lithium Ion Cells on Cycling Performance and Cell Impedance," Journal of The Electrochemical Society, vol. 160, no. 10, pp. A1668–A1674, 2013.

[69] M. C. Smart, B. L. Lucht, S. Dalavi, F. C. Krause, and B. V. Ratnakumar, "The Effect of Additives upon the Performance of MCMB/LiNixCo1-xO2 Li-Ion Cells Containing Methyl Butyrate-Based Wide Operating Temperature Range Electrolytes," Journal of The Electrochemical Society, vol. 159, p. A739, Apr. 2012.

[70] L. Somerville, S. Ferrari, M. J. Lain, A. McGordon, P. Jennings, and R. Bhagat, "An In-Situ Reference Electrode Insertion Method for Commercial 18650-Type Cells," Batteries, vol. 4, p. 18, June 2018.

[71] E. McTurk, C. R. Birkl, M. R. Roberts, D. A. Howey, and P. G. Bruce, "Minimally Invasive Insertion of Reference Electrodes into Commercial Lithium-Ion Pouch Cells," ECS Electrochemistry Letters, vol. 4, p. A145, Jan. 2015.

[72] M. Dubarry, V. Svoboda, R. Hwu, and B. Yann Liaw, "Incremental Capacity Analysis and Close-to-Equilibrium OCV Measurements to Quantify Capacity Fade in Commercial Rechargeable Lithium Batteries," Electrochemical and Solid-State Letters, vol. 9, no. 10, p. A454, 2006.

[73] I. D. Campbell, M. Marzook, M. Marinescu, and G. J. Offer, "How Observable Is Lithium Plating? Differential Voltage Analysis to Identify and Quantify Lithium Plating Following Fast Charging of Cold Lithium-Ion Batteries," Journal of The Electrochemical Society, vol. 166, no. 4, pp. A725–A739, 2019.

[74] C. Martin, M. Genovese, A. Louli, R. Weber, and J. Dahn, "Cycling Lithium Metal on Graphite to Form Hybrid Lithium-Ion/Lithium Metal Cells," Joule, vol. 4, pp. 1296–1310, June 2020.

[75] R. Mogi, M. Inaba, Y. Iriyama, T. Abe, and Z. Ogumi, "In Situ Atomic Force Microscopy Study on Lithium Deposition on Nickel Substrates at Elevated Temperatures," Journal of The Electrochemical Society, vol. 149, p. A385, Feb. 2002.

[76] R. L. Sacci, N. J. Dudney, K. L. More, L. R. Parent, I. Arslan, N. D. Browning, and R. R. Unocic, "Direct visualization of initial SEI morphology and growth kinetics during lithium deposition by in situ electrochemical transmission electron microscopy," Chemical Communications, vol. 50, pp. 2104–2107, Jan. 2014.

[77] T. Gao, Y. Han, D. Fraggedakis, S. Das, T. Zhou, C. N. Yeh, S. Xu, W. C. Chueh, J. Li, and M. Z. Bazant, "Interplay of Lithium Intercalation and Plating on a Single Graphite Particle," Joule, vol. 5, no. 2, pp. 393–414, 2021.

[78] R. Bhattacharyya, B. Key, H. Chen, A. S. Best, A. F. Hollenkamp, and C. P. Grey, "In situ NMR observation of the formation of metallic lithium microstructures in lithium batteries," Nature Materials, vol. 9, pp. 504–510, June 2010.

[79] H. J. Chang, N. M. Trease, A. J. Ilott, D. Zeng, L.-S. Du, A. Jerschow, and C. P. Grey, "Investigating Li Microstructure Formation on Li Anodes for Lithium Batteries by in Situ 6Li/7Li NMR and SEM," The Journal of Physical Chemistry C, vol. 119, pp. 16443–16451, July 2015.

[80] M. T. Fonseca Rodrigues, V. A. Maroni, D. J. Gosztola, K. P. Yao, K. Kalaga, I. A. Shkrob, and D. P. Abraham, "Lithium acetylide: A spectroscopic marker for lithium deposition during fast charging of Li-ion cells," ACS Applied Energy Materials, vol. 2, pp. 873–881, Jan. 2019.

[81] M. A. Cabañero, M. Hagen, and E. Quiroga-González, "In-operando Raman study of lithium plating on graphite electrodes of lithium ion batteries," Electrochimica Acta, vol. 374, p. 137487, Apr. 2021.

[82] C. Sole, N. E. Drewett, and L. J. Hardwick, "In situ Raman study of lithium-ion intercalation into microcrystalline graphite," Faraday Discussions, vol. 172, pp. 223–237, 2014.

[83] M. Sadd, S. Xiong, J. R. Bowen, F. Marone, and A. Matic, "Investigating microstructure evolution of lithium metal during plating and stripping via operando X-ray tomographic microscopy," Nature Communications, vol. 14, p. 854, Feb. 2023.

[84] K. Dong, M. Osenberg, F. Sun, H. Markötter, C. J. Jafta, A. Hilger, T. Arlt, J. Banhart, and I. Manke, "Non-destructive characterization of lithium deposition at the Li/separator and Li/carbon matrix interregion by synchrotron X-ray tomography," Nano Energy, vol. 62, no. May, pp. 11–19, 2019.

[85] M. Yusuf, J. M. LaManna, P. P. Paul, D. N. Agyeman-Budu, C. Cao, A. R. Dunlop, A. N. Jansen, B. J. Polzin, S. E. Trask, T. R. Tanim, E. J. Dufek, V. Thampy, H.-G. Steinrück, M. F. Toney, and J. Nelson Weker, "Simultaneous neutron and X-ray tomography for visualization of graphite electrode degradation in fast-charged lithium-ion batteries," Cell Reports Physical Science, p. 101145, 2022.

[86] P. Pietsch and V. Wood, "X-Ray Tomography for Lithium Ion Battery Research: A Practical Guide," Annual Review of Materials Research, vol. 47, pp. 451–479, 2017.

[87] D. Saurel, J. Segalini, M. Jauregui, A. Pendashteh, B. Daffos, P. Simon, and M. Casas-Cabanas, "A SAXS outlook on disordered carbonaceous materials for electrochemical energy storage," Energy Storage Materials, vol. 21, pp. 162–173, Sept. 2019.

[88] C. Zhao, Q. Wang, Y. Lu, B. Li, L. Chen, and Y.-S. Hu, "High-temperature treatment induced carbon anode with ultrahigh Na storage capacity at low-voltage plateau," Science Bulletin, vol. 63, pp. 1125–1129, Sept. 2018.

[89] "https://www.catl.com/en/news/6401.html, Accessed: 2026-01-27," Apr. 2025.

[90] L. Kitsu Iglesias, E. N. Antonio, T. D. Martinez, L. Zhang, Z. Zhuo, S. J. Weigand, J. Guo, and M. F. Toney, "Revealing the Sodium Storage Mechanisms in Hard Carbon Pores," Advanced Energy Materials, vol. 13, no. 44, p. 2302171, 2023.

[91] C. Qiu, A. Li, D. Qiu, Y. Wu, Z. Jiang, J. Zhang, J. Xiao, R. Yuan, Z. Jiang, X. Liu, X. Chen, and H. Song, "One-Step Construction of Closed Pores Enabling High Plateau Capacity Hard Carbon Anodes for Sodium-Ion Batteries: Closed-Pore Formation and Energy Storage Mechanisms," ACS Nano, vol. 18, pp. 11941–11954, May 2024.

[92] E. O. Eren, E. Senokos, E. Scoppola, Z. Song, M. Antonietti, and P. Giusto, "An enhanced three-stage model for sodium storage in hard carbons," Energy & Environmental Science, p. 10.1039.D4EE06029F, 2025.

[93] X. Chen, Y. Zheng, W. Liu, C. Zhang, S. Li, and J. Li, "High-performance sodium-ion batteries with a hard carbon anode: transition from the half-cell to full-cell perspective," Nanoscale, vol. 11, pp. 22196–22205, Nov. 2019.

[94] Y. Morikawa, S.-i. Nishimura, R.-i. Hashimoto, M. Ohnuma, and A. Yamada, "Mechanism of Sodium Storage in Hard Carbon: An X-Ray Scattering Analysis," Advanced Energy Materials, vol. 10, no. 3, p. 1903176, 2020.

[95] D. A. Stevens and J. R. Dahn, "An In Situ Small-Angle X-Ray Scattering Study of Sodium Insertion into a Nanoporous Carbon Anode Material within an Operating Electrochemical Cell," Journal of The Electrochemical Society, vol. 147, p. 4428, Dec. 2000.

[96] R. Fang, S. Zhao, Z. Sun, D.-W. Wang, H.-M. Cheng, and F. Li, "More Reliable Lithium-Sulfur Batteries: Status, Solutions and Prospects," Advanced Materials, vol. 29, no. 48, p. 1606823, 2017.

[97] A. Manthiram, Y. Fu, S.-H. Chung, C. Zu, and Y.-S. Su, "Rechargeable Lithium–Sulfur Batteries," Chemical Reviews, vol. 114, pp. 11751–11787, Dec. 2014.

[98] X. Li, L. Yuan, D. Liu, J. Xiang, Z. Li, and Y. Huang, "Solid/Quasi-Solid Phase Conversion of Sulfur in Lithium–Sulfur Battery," Small, vol. 18, no. 43, pp. 1–29, 2022.

[99] M. Sadd, S. De Angelis, S. Colding-Jørgensen, D. Blanchard, R. E. Johnsen, S. Sanna, E. Borisova, A. Matic, and J. R. Bowen, "Visualization of Dissolution-Precipitation Processes in Lithium–Sulfur Batteries," Advanced Energy Materials, vol. 12, no. 10, p. 2103126, 2022.

[100] J. Conder, R. Bouchet, S. Trabesinger, C. Marino, L. Gubler, and C. Villevieille, "Direct observation of lithium polysulfides in lithium-sulfur batteries using operando X-ray diffraction," Nature Energy, vol. 2, no. May, pp. 1–7, 2017.

[101] J. Conder, C. Villevieille, S. Trabesinger, P. Novák, L. Gubler, and R. Bouchet, "Electrochemical impedance spectroscopy of a Li–S battery: Part 1. Influence of the electrode and electrolyte compositions on the impedance of symmetric cells," Electrochimica Acta, vol. 244, pp. 61–68, Aug. 2017.

[102] Y. Diao, K. Xie, S. Xiong, and X. Hong, "Shuttle phenomenon - The irreversible oxidation mechanism of sulfur active material in Li-S battery," Journal of Power Sources, vol. 235, pp. 181–186, 2013.

[103] M. Agostini, S. Xiong, A. Matic, and J. Hassoun, "Polysulfide-containing Glyme-based Electrolytes for Lithium Sulfur Battery," Chemistry of Materials, vol. 27, pp. 4604–4611, July 2015.

[104] Y. Liu, Y. Elias, J. Meng, D. Aurbach, R. Zou, D. Xia, and Q. Pang, "Electrolyte solutions design for lithium-sulfur batteries," Joule, vol. 5, pp. 2323–2364, Sept. 2021.

[105] M. Zhao, B. Li, H. Peng, H. Yuan, J. Wei, and J. Huang, "Lithium–Sulfur Batteries under Lean Electrolyte Conditions: Challenges and Opportunities," Angewandte Chemie International Edition, vol. 59, pp. 12636–12652, July 2020.

[106] Q. Pang, A. Shyamsunder, B. Narayanan, C. Y. Kwok, L. A. Curtiss, and L. F. Nazar, "Tuning the electrolyte network structure to invoke quasi-solid state sulfur conversion and suppress lithium dendrite formation in Li–S batteries," Nature Energy, vol. 3, no. 9, pp. 783–791, 2018.

[107] A. Jozwiuk, B. B. Berkes, T. Weiß, H. Sommer, J. Janek, and T. Brezesinski, "The critical role of lithium nitrate in the gas evolution of lithium–sulfur batteries," Energy & Environmental Science, vol. 9, no. 8, pp. 2603–2608, 2016.

[108] L. Kong, L. Yin, F. Xu, J. Bian, H. Yuan, Z. Lu, and Y. Zhao, "Electrolyte solvation chemistry for lithium–sulfur batteries with electrolyte-lean conditions," Journal of Energy Chemistry, vol. 55, pp. 80–91, Apr. 2021.

[109] J. Castillo, A. Soria-Fernández, S. Rodriguez-Peña, J. Rikarte, A. Robles-Fernández, I. Aldalur, R. Cid, J. A. González-Marcos, J. Carrasco, M. Armand, A. Santiago, and D. Carriazo, "Graphene-Based Sulfur Cathodes and Dual Salt-Based Sparingly Solvating Electrolytes: A Perfect Marriage for High Performing, Safe, and Long Cycle Life Lithium-Sulfur Prototype Batteries," Advanced Energy Materials, vol. 14, p. 2302378, Nov. 2023.

[110] G. Wang, X. Luo, W. Sun, and J. Cai, "Assessing the practical feasibility of solid-state lithium–sulfur batteries," Communications Materials, vol. 6, p. 211, Sept. 2025.

[111] H. Yang and N. Wu, "Ionic conductivity and ion transport mechanisms of solid-state lithium-ion battery electrolytes: A review," Energy Science & Engineering, vol. 10, pp. 1643–1671, May 2022.

[112] M. Otoyama, M. Suyama, C. Hotehama, H. Kowada, Y. Takeda, K. Ito, A. Sakuda, M. Tatsumisago, and A. Hayashi, "Visualization and Control of Chemically Induced Crack Formation in All-Solid-State Lithium-Metal Batteries with Sulfide Electrolyte," ACS Applied Materials & Interfaces, vol. 13, pp. 5000–5007, Feb. 2021.

[113] R. Bouchal, A. Boulaoued, and P. Johansson, "Monitoring Polysulfide Solubility and Diffusion in Fluorinated Ether-Based Electrolytes by Operando Raman Spectroscopy," Batteries & Supercaps, vol. 3, no. 5, pp. 397–401, 2020.

[114] A. Yermukhambetova, C. Tan, S. R. Daemi, Z. Bakenov, J. A. Darr, D. J. L. Brett, and P. R. Shearing, "Exploring 3D microstructural evolution in Li-Sulfur battery electrodes using in-situ X-ray tomography," Scientific Reports, vol. 6, p. 35291, Oct. 2016.

[115] C. Tan, T. M. M. Heenan, R. F. Ziesche, S. R. Daemi, J. Hack, M. Maier, S. Marathe, C. Rau, D. J. L. Brett, and P. R. Shearing, "Four-Dimensional Studies of Morphology Evolution in Lithium–Sulfur Batteries," ACS Applied Energy Materials, vol. 1, pp. 5090–5100, Sept. 2018.

[116] L. Zielke, C. Barchasz, S. Waluś, F. Alloin, J.-C. Leprêtre, A. Spettl, V. Schmidt, A. Hilger, I. Manke, J. Banhart, R. Zengerle, and S. Thiele, "Degradation of Li/S Battery Electrodes On 3D Current Collectors Studied Using X-ray Phase Contrast Tomography," Scientific Reports, vol. 5, p. 10921, June 2015.

[117] J. S. Edge, S. O'Kane, R. Prosser, N. D. Kirkaldy, A. N. Patel, A. Hales, A. Ghosh, W. Ai, J. Chen, J. Yang, S. Li, M.-C. Pang, L. Bravo Diaz, A. Tomaszewska, M. W. Marzook, K. N. Radhakrishnan, H. Wang, Y. Patel, B. Wu, and G. J. Offer, "Lithium ion battery degradation: what you need to know," Physical Chemistry Chemical Physics, vol. 23, no. 14, pp. 8200–8221, 2021.

[118] X. Wu, S. Li, B. Yang, and C. Wang, "In Situ Transmission Electron Microscopy Studies of Electrochemical Reaction Mechanisms in Rechargeable Batteries," Electrochemical Energy Reviews, vol. 2, pp. 467–491, Sept. 2019.

[119] X. Liu, Z. Liang, Y. Xiang, M. Lin, Q. Li, Z. Liu, G. Zhong, R. Fu, and Y. Yang, "Solid-State NMR and MRI Spectroscopy for Li/Na Batteries: Materials, Interface, and In Situ Characterization," Advanced Materials, vol. 33, p. 2005878, Dec. 2021.

[120] J. S. Weaving, A. Lim, J. Millichamp, T. P. Neville, D. Ledwoch, E. Kendrick, P. F. McMillan, P. R. Shearing, C. A. Howard, and D. J. L. Brett, "Elucidating the Sodiation Mechanism in Hard Carbon by Operando Raman Spectroscopy," ACS Applied Energy Materials, vol. 3, pp. 7474–7484, Aug. 2020.

[121] K. Gotoh, T. Yamakami, I. Nishimura, H. Kometani, H. Ando, K. Hashi, T. Shimizu, and H. Ishida, "Mechanisms for overcharging of carbon electrodes in lithium-ion/sodium-ion batteries analysed by operando solid-state NMR," Journal of Materials Chemistry A, vol. 8, pp. 14472–14481, July 2020.

[122] J. Arai, Y. Okada, T. Sugiyama, M. Izuka, K. Gotoh, and K. Takeda, "In Situ Solid State 7 Li NMR Observations of Lithium Metal Deposition during Overcharge in Lithium Ion Batteries," Journal of The Electrochemical Society, vol. 162, no. 6, pp. A952–A958, 2015.

[123] B. Ma, S. Agrawal, R. Gopal, and P. Bai, "Operando Microscopy Diagnosis of the Onset of Lithium Plating in Transparent Lithium-Ion Full Cells," ACS Applied Materials & Interfaces, vol. 14, pp. 54708–54715, Dec. 2022.

[124] K. Nishikawa, J. Moon, and K. Kanamura, "In-situ observation of volume expansion behavior of a silicon particle in various electrolytes," Journal of Power Sources, vol. 302, pp. 46–52, Jan. 2016.

[125] D. Mayerich and R. Sun, "Superresolution Image Processing," in Microscope Image Processing, pp. 319–334, Elsevier, 2023.

[126] J. Maddox, "The sensational discovery of X-rays," Nature, vol. 375, pp. 183–183, May 1995.

[127] P. R. Willmott, An introduction to synchrotron radiation: techniques and applications. John Wiley & sons, 2nd ed ed., 2019.

[128] K. Miao, S. Chen, and J. Zhou, "The X-ray absorption spectroscopy for advanced battery systems," Sustainable Materials and Technologies, vol. 45, p. e01608, Oct. 2025.

[129] M. J. Ogley, A. S. Menon, G. C. Pandey, G. J. Páez Fajardo, B. J. Johnston, I. McClelland, V. Majherova, S. Huband, D. Tripathy, I. Temprano, S. Agrestini, V. Celorrio, G. E. Pérez, S. G. Booth, C. P. Grey, S. A. Cussen, and L. F. Piper, "Metal-ligand redox in layered oxide cathodes for Li-ion batteries," Joule, vol. 9, p. 101775, Jan. 2025.

[130] L. Jia, J. Wang, S. Ren, G. Ren, X. Jin, L. Kao, X. Feng, F. Yang, Q. Wang, L. Pan, Q. Li, Y. Liu, Y. Wu, G. Liu, J. Feng, S. Fan, Y. Ye, J. Guo, and Y. Zhang, "Unraveling Shuttle Effect and Suppression Strategy in Lithium/-Sulfur Cells by In Situ/Operando X-ray Absorption Spectroscopic Characterization," ENERGY & ENVIRONMENTAL MATERIALS, vol. 4, pp. 222–228, Apr. 2021.

[131] P. Ghigna and E. Quartarone, "Operando x-ray absorption spectroscopy on battery materials: a review of recent developments," Journal of Physics: Energy, vol. 3, p. 032006, July 2021.

[132] I. Källquist, R. Le Ruyet, H. Liu, R. Mogensen, M.-T. Lee, K. Edström, and A. J. Naylor, "Advances in studying interfacial reactions in rechargeable batteries by photoelectron spectroscopy," Journal of Materials Chemistry A, vol. 10, no. 37, pp. 19466–19505, 2022.

[133] I. Källquist, F. Lindgren, M.-T. Lee, A. Shavorskiy, K. Edström, H. Rensmo, L. Nyholm, J. Maibach, and M. Hahlin, "Probing Electrochemical Potential Differences over the Solid/Liquid Interface in Li-Ion Battery Model Systems," ACS Applied Materials & Interfaces, vol. 13, pp. 32989–32996, July 2021.

[134] A. Missyul, I. Bolshakov, and R. Shpanchenko, "XRD study of phase transformations in lithiated graphite anodes by Rietveld method," Powder Diffraction, vol. 32, pp. 1–7, May 2017.

[135] J. K. Mathiesen, R. E. Johnsen, A. S. Blennow, and P. Norby, "Understanding the structural changes in lithiated graphite through high-resolution operando powder X-ray diffraction," Carbon, vol. 153, pp. 347–354, Nov. 2019.

[136] K. P. C. Yao, J. S. Okasinski, K. Kalaga, I. A. Shkrob, and D. P. Abraham, "Quantifying lithium concentration gradients in the graphite electrode of Li-ion cells using *operando* energy dispersive X-ray diffraction," Energy & Environmental Science, vol. 12, no. 2, pp. 656–665, 2019.

[137] M. Olsson, A. Klein, N. Mozhzhukhina, S. Xiong, C. Appel, M. Carlsen, L. Nielsen, L. Rensmo, M. Liebi, and A. Matic, "Resolving the Sodiation Process in Hard Carbon Anodes with Nanostructure Specific X-Ray Imaging," Advanced Science, vol. n/a, no. n/a, p. e08635, 2025.

[138] H. Zhou, Y. Song, B. Zhang, H. Sun, I. A. Khurshid, Y. Kong, L. Chen, L. Cui, D. Zhang, W. Wang, L. Yang, and X. Du, "Overview of electrochemical competing process of sodium storage and metal plating in hard carbon anode of sodium ion battery," Energy Storage Materials, vol. 71, p. 103645, Aug. 2024.

[139] D. Paganin, S. C. Mayo, T. E. Gureyev, P. R. Miller, and S. W. Wilkins, "Simultaneous phase and amplitude extraction from a single defocused image of a homogeneous object," Journal of Microscopy, vol. 206, no. 1, pp. 33–40, 2002.

[140] A. Sadezky, H. Muckenhuber, H. Grothe, and R. Niessner, "Raman microspectroscopy of soot and related carbonaceous materials: Spectral analysis and structural information," Carbon, vol. 43, pp. 1731–1742, 2005.

[141] S. Alvin, H. S. Cahyadi, J. Hwang, W. Chang, S. K. Kwak, and J. Kim, "Revealing the Intercalation Mechanisms of Lithium, Sodium, and Potassium in Hard Carbon," Advanced Energy Materials, vol. 10, no. 20, p. 2000283, 2020.

[142] S. Jabri, L. P. Bauermann, and M. Vetter, "Raman spectrometry measurements for the 2D mapping of the degradation products on aged graphite anodes of cylindrical Li-ion battery cells," AIP Advances, vol. 13, p. 115114, 2023.

[143] V. Maccio-Figgemeier, G. G. Eshetu, D. Mroz, H. Joo, and E. Figgemeier, "Establishing Li-acetylide (Li2C2) as functional element in solid-electrolyte interphases in lithium-ion batteries," Journal of Power Sources Advances, vol. 28, p. 100152, Aug. 2024.

[144] M. Sadd, M. Agostini, S. Xiong, and A. Matic, "Polysulfide Speciation and Migration in Catholyte Lithium-Sulfur Cells," ChemPhysChem, vol. 23, no. 4, p. e202100853, 2022.

[145] S. J. Talley, S. L. Vivod, B. A. Nguyen, M. A. B. Meador, A. Radulescu, and R. B. Moore, "Hierarchical Morphology of Poly(ether ether ketone) Aerogels," ACS Applied Materials & Interfaces, vol. 11, pp. 31508–31519, Aug. 2019.

[146] H. Aso, K. Matsuoka, A. Sharma, and A. Tomita, "Structural analysis of PVC and PFA carbons prepared at 500–1000 °C based on elemental composition, XRD, and HRTEM," Carbon, vol. 42, no. 14, pp. 2963–2973, 2004.

[147] J. Rizell, Alkali Metal Plating and Stripping in Liquid Electrolytes. Ph.D. dissertation, Chalmers University of Technology, 2025.

[148] H. Schnablegger and Y. Singh, The SAXS Guide. Anton Paar GmbH, 3 ed., 2013.

[149] P. Lindnen and J. Oberdisse, Neutrons, X-rays, and Light. Elsevier, 2025.

[150] P. Thompson, D. E. Cox, and J. B. Hastings, "Rietveld Refinement of Debye-Scherrer Synchrotron X-ray Data from Al2O3," Journal of Applied Crystallography, vol. 20, pp. 79–83, 1987.

[151] E. T. North, C. Skautvedt, A. K. Thiagarajan, M. Di Michiel, S. Checchia, A. Y. Koposov, and D. S. Wragg, "X-ray Beam Damage Effects in a Lithium-Ion Battery Probed by Spatially Resolved X-ray Diffraction," ACS Energy Letters, vol. 10, pp. 4930–4932, Oct. 2025.

[152] T. Jousseaume, J.-F. Colin, M. Chandesris, S. Lyonnard, and S. Tardif, "How Beam Damage Can Skew Synchrotron *Operando* Studies of Batteries," ACS Energy Letters, vol. 8, pp. 3323–3329, Aug. 2023.

[153] P. Larkin, Infrared and Raman Spectroscopy: Principles and Spectral Interpretation. Elsevier, 2011.

[154] H. Adenusi, G. A. Chass, S. Passerini, K. V. Tian, and G. Chen, "Lithium Batteries and the Solid Electrolyte Interphase (SEI)—Progress and Outlook," Advanced Energy Materials, vol. 13, p. 2203307, Mar. 2023.

[155] Y. Lee, J. Park, H. Jeon, D. Yeon, B.-H. Kim, K. Y. Cho, M.-H. Ryou, and Y. M. Lee, "In-depth correlation of separator pore structure and electrochemical performance in lithium-ion batteries," Journal of Power Sources, vol. 325, pp. 732–738, Sept. 2016.

[156] M. Liebi, M. Georgiadis, J. Kohlbrecher, M. Holler, J. Raabe, I. Usov, A. Menzel, P. Schneider, O. Bunk, and M. Guizar-Sicairos, "Small-angle X-ray scattering tensor tomography: model of the three-dimensional reciprocal-space map, reconstruction algorithm and angular sampling requirements," Acta Crystallographica Section A Foundations and Advances, vol. 74, pp. 12–24, Jan. 2018.

[157] A. Vizintin, L. Chabanne, E. Tchernychova, I. Arčon, L. Stievano, G. Aquilanti, M. Antonietti, T.-P. Fellinger, and R. Dominko, "The mechanism of Li2S activation in lithium-sulfur batteries: Can we avoid the polysulfide formation?," Journal of Power Sources, vol. 344, pp. 208–217, Mar. 2017.